NASA-CR-174,847

NASA Contractor Report 174847

NASA-CR-174847
19850009818

The Effect of Tantalum on the Structure/Properties of Two Polycrystalline Nickel-Base Superalloys: B-1900 + Hf and MAR-M247

Gregg M. Janowski

Michigan Technological University
Houghton, Michigan

February 1985

Prepared for

NATIONAL AERONAUTICS AND SPACE ADMINISTRATION
Lewis Research Center
Under Grant NAG 3-216

ABSTRACT

THE EFFECT OF TANTALUM ON THE STRUCTURE/PROPERTIES OF TWO POLYCRYSTALLINE NICKEL-BASE SUPERALLOYS: B-1900 + Hf AND MAR-M247

The microstructure, phase compositions, and phase fractions were studied in conventionally cast B-1900 + Hf and both conventionally cast and directionally solidified MAR-M247 as a function of tantalum concentration. The hot tensile and creep rupture properties of the solutionized and aged MAR-M247-type alloys were also determined as a function of tantalum level.

The effects of tantalum on the microstructure and phase compositions of B-1900 + Hf and MAR-M247 (conventionally cast and directionally solidified) were found to be very similar. The addition of tantalum to the as-cast and heat treated alloys was shown to cause the partial replacement of the Hf in the MC carbides by Ta, although the degree of replacement was decreased by the solutionizing and aging heat treatment. The gamma prime and minor phase fractions (primarily MC-type carbides) both increased approximately linearly with tantalum concentration. The gamma prime phase compositions were relatively insensitive to tantalum variations with the exception of the tantalum and/or hafnium levels. Bulk tantalum additions increased the tantalum, chromium, and cobalt levels of the gamma phase in both alloy series. The increase in the concentrations of the latter two elements in the gamma phase was a result of the decrease in the gamma phase fraction with increasing bulk

tantalum concentration and constant gamma/gamma prime partitioning ratio.

Tantalum additions increased the yield stress and ultimate tensile strength of the directionally solidified MAR-M247-type alloys and had no significant effect on ductility. The secondary creep rate was decreased and the creep rupture life was increased in the directionally solidified MAR-M247-type alloys with the addition of tantalum. The mechanisms believed responsible for these improvements are the increase in gamma prime weight fraction and increased solid solution strengthening of the gamma and gamma prime phases with increasing tantalum content. Stress coarsening of the gamma prime precipitates was also observed in the creep samples tested at 982°C. The conventionally cast MAR-M247-type alloys exhibited extremely low ductilities and premature failures which were related to the large fraction of intergranular fracture surface observed in the failed specimens.

TABLE OF CONTENTS

INTRODUCTION

Nickel-base superalloys possess a unique combination of properties that have made them invaluable to the aircraft gas turbine industry. They are highly resistant to fatigue, oxidation, and hot corrosion at high temperatures while still possessing good strength. Since the introduction of precipitation strengthened Ni/Cr/Al/Ti alloys in the 1940's, much research effort has been focused on improving superalloy performance through optimization of composition and processing. For example, this development effort has led to the highly alloyed cast materials where subsequent improvements in mechanical properties were obtained by directional solidification.

Recently, the additional factor of the availability of various alloying elements has complicated the superalloy development strategy. The United States imports nearly all of its Cr, Co, Ta, and Nb [1]. Cr and Co typically comprise nearly twenty-five weight percent of a modern cast superalloy, and the smaller alloying additions of Ta and Nb are equally critical for alloy performance. The uncertainty of long term supplies of these four "strategic elements" has caused concern in the aerospace industry. Therefore, it is desirable to study the role of these alloying elements in nickel-base superalloys, with the goal of reducing or replacing them without degrading material performance. In this context, the primary goal of this study is to determine the role of tantalum in the microstructure and high temperature mechanical properties of polycrystalline (both equiaxed and directionally solidified) MAR-M247. A secondary objective is to determine the effects of tantalum on the microstructure of a similar superalloy, B-1900 + Hf. By studying both of these alloys (which are commercially important, cast

nickel-base superalloys), a broader understanding of the "tantalum effect" will be obtained.

Microstructure of Nickel-Base Superalloys

Since the mechanical properties of a material are a direct consequence of its microstructure, a logical starting point for this introduction to nickel-base superalloys is an overview of superalloy microstructure. A modern cast nickel-base superalloy is composed of between six and twelve intentionally added elements. Before considering a commercial-type alloy, it would be instructive to first examine a simplified system, the nickel-rich portion of the Ni/Cr/Al phase diagram. The austenite matrix, the gamma phase, is a nickel-chromium solid solution, with a small amount of Al also being present. An ordered, coherent precipitate, gamma prime, forms when the solubility of Al in the matrix is exceeded at the temperature of interest. The composition of gamma prime is based on Ni_3Al, with some solubility of chromium. The gamma prime crystal structure is one of the ordered face-centered cubic (FCC) variants, $L1_2$, with the Al atoms occupying the corner positions and the nickel atoms in the face-centered positions of the unit cell. These alloys can be heat treated by solutionizing the alloy in the single phase region (above the gamma prime solvus temperature), and subsequently aging at a lower temperature to precipitate a dispersion of fine gamma prime. For a given alloy, the particle size and volume fraction are a function of the aging time and temperature.

Commercial nickel-base superalloys have some combination of Ti, Nb, Ta, C, B, Zr, Hf, Co, Fe, W, V, and Mo additions to the Ni/Cr/Al ternary. The additions of these elements in the proper proportions have

been found to improve the mechanical properties of superalloys, although these developments have been largely empirical. The mechanisms responsible for these improvements in mechanical properties include grain boundary strengthening through carbide precipitation or elemental segregation, solid solution strengthening of gamma and gamma prime, and altering other phase properties such as the anti-phase boundary energy of gamma prime. Most elements contribute to alloy strengthening through more than one of these mechanisms. Typical alloying additions that partition to the gamma phase are W, Mo, Co, Cr, and Fe, although the gamma prime phase also contains lower levels of these elements [2]. Vanadium, Nb, and Ta have been shown to be nearly completely contained in the gamma prime phase, while Al and Ti partition less strongly than the former elements to gamma prime [2]. Titanium, Nb, V, Ta, and W occupy Al positions in Ni_3Al while Co substitutes for Ni [2, 3]. Molybdenum and Fe either replace Al and Ni in Ni_3Al, respectively [2], or show no site preference [3]. The equilibrium gamma prime morphology is determined by the difference between the gamma and gamma prime lattice parameters, which is in turn determined by the alloying elements and their distribution between the two phases. A small mismatch (less than 0.5%) leads to spheroidal precipitates while larger misfits cause gamma prime precipitates to become cuboidal and eventually plate-like [4]. Elements such as Ti, Hf, Ta, Nb, Cr, W, Mo, Zr, and V are used in the formation of borides and/or carbides. The presence of these precipitates on the grain boundaries improves the creep resistance of the material. A more detailed discussion of the minor phases is included later in this section.

The gamma prime phase forms in three manners in as-cast nickel-base superalloys, although there is some disagreement on nomenclature. Primary gamma prime, also known as gamma/gamma prime eutectic, the "white etching phase", gamma prime nodules, and in some cases, degenerate gamma/gamma prime, is the product of the final, solute-rich interdendritic liquid [5]. Primary gamma prime is rich in Al, Ti [5, 6], and Hf [7, 8], and depleted in Cr, W [5, 6], and Co [6], relative to the gamma/gamma prime matrix. Primary gamma prime typically takes the form of degenerate pools or lamellar rosettes. In the latter case, particles of gamma prime are separated by gamma ribbons in a fan-like arrangement. Degenerate eutectic pools consist of large areas of spherulitic gamma prime, often with strips of gamma separating gamma prime particles. All or most of the gamma phase in the gamma/gamma prime eutectic dissolves into the gamma prime phase after solidification, a result of the enlarged gamma prime phase field at lower temperatures [5, 9]. On further cooling, the second type, coarse gamma prime, forms by solid state precipitation from the supersaturated gamma phase. The morphology of coarse gamma prime is cuboidal, with the cube edges approximately 1 micron in length. The last type, fine gamma prime, precipitates at lower temperatures as spheroids typically less than 0.5 micron in diameter. Fine gamma prime is thought to nucleate homogeneously in alloys with small gamma/gamma prime mismatch [3]. Uniformly dispersed fine gamma prime provides maximum creep resistance, whereas primary gamma prime and coarse gamma prime are less effective [10]. However, primary gamma prime is thought to improve the ductility of transverse grain boundaries [11]. Current commercial heat treatment schedules for directionally solidified (DS) and single crystal materi-

als are designed to maximize creep resistance by solutionizing and homogenizing the as-cast gamma prime and then reprecipitating a uniform dispersion of fine gamma prime.

The primary role of carbon in nickel-base superalloys is to precipitate carbides along the grain boundaries. The presence of discrete carbide particles along the grain boundaries has been shown to inhibit grain boundary sliding, an important high temperature deformation mechanism. Four distinct classes of carbides have been observed in superalloys, namely MC, M_6C, M_7C_3, and $M_{23}C_6$. The "M" in the compounds represents a carbide forming metallic element, but typically is composed of a combination of metallic elements. The exact composition is a function of carbide type and heat treatment.

MC carbides are among the first solidification products. The principal metallic elements that compose MC carbides are, in preferred order of formation, Ta, Nb, Ti, and V [12], with Hf showing behavior that is not easily ranked (see below for a detailed discussion of Hf effects). Molybdenum and W also substitute in the FCC structure which MC carbides possess. It is possible for several chemically distinct MC carbides to co-exist in a given alloy. In addition, the morphology of MC carbides is a function of cooling rate and, in some cases, melt composition. A slow solidification rate leads to an interdendritic network of script carbides; a rapid solidification rate leads to cubic or "blocky" carbides [12, 13]. In fact, the effects of various relative solidification rates on MC carbide morphology have been observed with section size differences [14].

The addition of Hf to nickel-base superalloys alters the composition and, in some cases, the morphology of the MC carbides. Microstructural comparisons of the same alloy with and without Hf have shown that Hf additions increase the number of chemically distinct MC carbides; in B-1900, there was an increase from one MC to four MC carbides with Hf additions, as determined by x-ray diffraction [15]. The range in measured lattice parameters indicated a variation in Hf level among the four MC carbide types from nil to nearly pure HfC. The x-ray diffraction data were supported by microprobe analysis of individual carbides which has also shown that the Hf levels vary within individual carbides [8, 15, 16]. This variation has been observed as Hf-rich rings around MC carbides or Hf-rich carbide segments. It has been suggested that the Hf inhomogeneities are a result of significant changes in the chemical activity of Hf during carbide formation [15]. This hypothesis implies a time dependency of MC composition, i.e. Hf-rich rings form in the latter stages of carbide formation. Hafnium additions have also been found to refine the MC carbide structure from an interconnected script network to discrete, blocky particles [15, 17], although this effect was not observed in a similar study [18].

While MC carbides are a solidification product, the other three types of carbides, M_7C_3, $M_{23}C_6$, and M_6C, are formed by solid state precipitation. M_7C_3 carbides are only found in simple Ni/Cr/Al/Ti alloys and are not stable in complex superalloys [3]. $M_{23}C_6$ carbides form in the temperature range from 760°C to 980°C, while M_6C carbides precipitate in the temperature range of 815°C to 980°C [12]. Chromium is the primary metallic element in $M_{23}C_6$ carbides, with lesser amounts of Ni, Mo, W, and other refractory elements substituting for Cr. The

M_6C carbides are composed mainly of W and Mo. Both $M_{23}C_6$ and M_6C carbides have large lattice parameters (greater than 1.0 nm) and complex cubic crystal structures. The morphology of $M_{23}C_6$ carbides is either in the form of a nearly continuous layer of platelets or discrete, blocky particles; both types are often located at the grain boundaries. A cube-on-cube orientation relationship ($\{100\}_{\gamma/\gamma'}$ // $\{100\}_{carbide}$) has been observed between $M_{23}C_6$ carbides and the matrix phases [6]. Such a relationship is reasonable since the $M_{23}C_6$ carbide phase has a lattice parameter that is almost exactly three times that of the matrix phases. An identical orientation relationship has also been found in austenitic stainless steels [19]. M_6C carbides can also form as discrete grain boundary precipitates, but in some cases take on an intragranular Widmanstätten morphology.

The sources of carbon for the formation of M_6C and $M_{23}C_6$ carbides are degeneration of MC carbides or carbon that remained in solution. The former case is thought to be more significant in light of the observed breakdown of MC carbides and subsequent precipitation of secondary carbides during long term aging. The following mechanisms have been proposed for MC degeneration and precipitation of $M_{23}C_6$ and M_6C carbides [12]:

$$MC + \text{gamma} \rightarrow M_{23}C_6 + \text{gamma prime}$$

$$MC + \text{gamma} \rightarrow M_6C + \text{gamma prime}$$

Although these reactions are not chemically balanced, they do illustrate three factors influencing secondary carbide precipitation. First, the amounts of M_6C and/or $M_{23}C_6$ carbides that form will depend on the relative stabilities of the three carbide classes. For example, low Cr and high W and Mo levels favor the formation of M_6C carbides. On the

other hand, very stable MC carbides, such as TaC and NbC, will slow the formation of $M_{23}C_6$ and M_6C carbides [12]. Secondly, the precipitation of secondary carbides will alter the matrix phase compositions, possibly leading to phase instabilities. The formation of $M_{23}C_6$ and M_6C carbides removes elements that partition to the gamma phase, W, Cr, and Mo, and releases elements that form gamma prime, Ti, Ta, and Nb. These compositional changes lead to the development of gamma prime envelopes around MC carbides and gamma prime coatings along the grain boundaries after long term aging treatments [20, 21]. Lastly, secondary carbides will tend to precipitate in the vicinity of MC carbides. The formation of $M_{23}C_6$ and M_6C carbides along the grain boundaries is a result of the degeneration of intergranular MC carbides.

The precipitation of relatively small, discrete carbides along the grain boundaries improves the creep resistance of superalloys. Unfortunately, other forms of carbides can have a detrimental effect on mechanical properties. For example, an interdendritic network of hard, brittle MC carbides provides likely sites for crack initiation and paths for rapid crack propagation [17]. Similar losses in ductility result from continuous or nearly continuous carbide layers on grain boundaries as well as the presence of M_6C carbides with an acicular morphology.

Topologically close packed (TCP) phases are an undesirable microconstituent in nickel-base superalloys. These intermetallic phases, known as mu, sigma, and Laves, form after extended high temperature aging of some alloys. Their occurrence has been related to poor composition control. TCP phases form in a plate morphology from the gamma phase parallel to the $\{111\}_\gamma$ [22]. The plate morphology can cause

significant reductions in creep rupture life and tensile ductility by providing sites for crack initiation and propagation [23]. In addition, because of their large Mo and W content, TCP phases would be expected to weaken an alloy due to reduced solid solution strengthening of the matrix phases. The phase compositions could also be altered such that the gamma/gamma prime mismatch changes, and this could possibly affect the gamma prime morphology [21]. Several approaches have been adopted to predict the formation of TCP phases, particularly sigma. The first, PHACOMP (for PHAse COMPutation), determines if the gamma phase is supersaturated with solute elements by applying electron vacancy theory. A major limitation of this method is that accurate gamma/gamma prime partitioning ratios must be available to calculate the gamma phase composition [24]. The second approach, SIGMA-SAFE, determines a "supersaturation number" and calculates an equivalent Ni/Mo/Al phase diagram at constant chromium level [24]. The predicted pseudo phase diagram is particularly attractive from an alloy development standpoint where it is desirable to assess the effects of alterations in alloy composition theoretically. Both PHACOMP and SIGMA-SAFE have been effective in predicting the susceptibility of individual heats of material to sigma formation.

Small additions of boron (0.005 to 0.02 wt.%) and zirconium (0.005 to 0.1 wt.%) are frequently made to polycrystalline nickel-base superalloys. Despite their low bulk concentrations, B and Zr markedly enhance the creep rupture properties of superalloys. The beneficial effects of B and Zr are thought to result from the segregation of atomic B and Zr to the grain boundaries [12], although Zr has been shown to nucleate MC carbides [25] and M_3B_2 or MB_{12}-type borides may

form along the grain boundaries. The large atomic size differences of B and Zr relative to the transition metals would be expected to increase the atomic density of the grain boundaries. An increased atomic density along the grain boundaries would decrease the grain boundary diffusion coefficients. This proposed mechanism is supported by the increased microstructural stability of transverse grain boundary phases with Zr and B additions to a model alloy [26].

An additional factor to consider in superalloy microstructures is the potential for alloying element interactions. For example, the addition of a stronger MC carbide forming element, such as Hf, will release elements otherwise contained in the MC carbides to the gamma and gamma prime phases [28]. The redistribution of Ti, Ta, and Nb to the matrix phases would be expected to increase the gamma prime volume fraction, as well as alter other phase properties. Another manner in which interactions can occur is by one element affecting the partitioning of another element; e.g. Ta additions increase the Al content of the gamma phase [27]. These secondary effects should be considered when examining bulk alloy compositional variations.

Control of grain structure is vital in cast nickel-base superalloys. The optimal grain size for conventionally cast alloys is a compromise between desired creep rupture and tensile properties [12]. A fine grain size is necessary for tensile properties because of Hall-Petch-type strengthening. A coarse grain size is desirable to minimize grain boundary sliding and diffusion at high temperatures. The relative importance of these two factors is dependent on stress and temperature. Directional solidification is an extreme case of grain structure control which virtually eliminates transversely oriented grain bound-

aries. Directionally solidified alloys have been shown to possess substantially enhanced creep resistance and ductility, as well as increased fatigue life, relative to their conventionally cast counterparts [6, 9, 29]. These improvements are a result of the elimination of transverse grain boundaries and the orientation of the preferred [001] direction parallel to the stress axis [9].

Strengthening Mechanisms for Nickel-Base Superalloys

Because of the high temperatures and stresses at which gas turbine engines operate, nickel-base superalloys are typically strengthened by a variety of mechanisms. The mechanisms can be divided into three classes: gamma strengthening, gamma prime strengthening, and precipitation hardening. Each of these strengthening mechanisms will be examined in turn.

The mechanisms that may be responsible for strengthening the gamma matrix include changes in lattice parameter, elastic moduli, stacking fault energy (SFE), and possibly short range ordering [3, 30, 31] as alloying additions are made. Changes in lattice parameter, which lead to atomic size misfit effects, and attractive and repulsive interactions between solute atoms and dislocations from changes in elastic moduli can be described using conventional solid solution hardening theory. On the basis of nickel binary alloys, Ti, Al, Cr, Mo, and W are potent solid solution hardeners of Ni [32, 33]. A reduction in SFE would also strengthen the gamma matrix due to increased resistance to dislocation cross-slip. At high temperatures, the addition of slow diffusing elements, such as Mo and W, would also contribute to gamma strengthening [3].

The gamma prime phase is hardened by solid solution additions and changes in the anti-phase boundary (APB) energy. Complications due to site occupancy, non-stoichiometry, and temperature effects (to be discussed below) make solid solution hardening experiments difficult to interpret, but Mo, Cr, W, Nb, and Ta are considered effective gamma prime strengtheners [3, 34]. The larger contribution to gamma prime strengthening from alloying additions is believed to be due to changes in the APB energy. Because gamma prime is an ordered intermetallic phase, the Burger's vector, $a/2\langle 110\rangle$, of a perfect dislocation in disordered FCC metals (including the gamma matrix of superalloys) is only a partial dislocation in gamma prime. Thus, the passage of one such dislocation introduces a high energy region known as an anti-phase domain. The passage of a second, identical dislocation is necessary to restore the ordered structure. Typically, the dislocations in gamma prime are observed in pairs, separated by a strip of anti-phase domain; the spacing is determined by the repulsive force between the dislocations and the magnitude of the APB energy. Elements that are thought to affect the APB energy and strengthen gamma prime include Ti, Nb, Ta, and W. An increase in the yield stress of gamma prime with increasing temperature has also been well documented. It is postulated that only the lead dislocation cross-slips to a $\{100\}$ plane from a $\{111\}$ plane, which becomes easier with increasing temperature. The dislocation pair is immobile until the trailing dislocation is also able to cross-slip. The decrease in yield stress observed above 750°C is associated with the cross-slip of both dislocations to $\{100\}$ planes where cube slip occurs. This transition temperature is sensitive to alloying additions.

Two of the most important strengthening mechanisms for nickel-base superalloys, order and coherency strain hardening, are related to the presence of coherent gamma prime precipitates in the microstructure. Coherency strains are the result of lattice mismatch between gamma and gamma prime, with the subsequent strain field interacting with the stress fields of dislocations. Coherency strains are a function of alloy additions and temperature. Order hardening arises from the creation of anti-phase domains (discussed above) by dislocation shearing of the ordered precipitates. Order hardening is not a factor with very large precipitates because the particle is then looped by the dislocations rather than sheared by them. A high volume fraction of evenly dispersed, fine gamma prime precipitates has been shown to impart maximum creep resistance to a high performance, cast superalloy (MAR-M200) [10]. Order hardening has been shown theoretically to be the largest contributor to alloy strength at room temperature and that coherency hardening and solid solution hardening of gamma and gamma prime have an equal, though lesser role [35].

Creep Mechanisms in Superalloys

The limiting factor in many superalloy applications is creep rupture behavior, with creep being defined as time dependent deformation at constant stress and $T > 0.6\ T_m$ (absolute melting temperature). Creep occurs in polycrystalline materials by a combination of mechanisms: grain boundary sliding, dislocation motion, and diffusional creep. Grain boundary sliding is minimized in superalloys by the presence of intergranular carbides and will not be considered further. The remaining creep processes will be briefly discussed below.

The creep curves for superalloys, as well as most metals, can be divided into three stages based on changes in the creep rate: a) primary creep ($d\varepsilon^2/d^2t < 0$), b) secondary or steady state creep ($d\varepsilon^2/d^2t = 0$), and c) tertiary creep ($d\varepsilon^2/d^2t > 0$). The secondary creep rate is one of the crucial alloy design parameters because a component spends most of its life in this stage. The secondary creep rate is determined by the temperature, stress, and of greatest interest to this study, microstructure. The onset of tertiary creep is characterized by either the development of grain boundary cavities and/or cracks, or microstructural instabilities such as grain growth or changes in precipitate distribution [36]. In either case, the end result is creep rupture failure.

The creep mechanisms that apply to nickel-base superalloys are thermally assisted processes. Diffusional creep, both within the lattice (Nabarro-Herring creep) and along the boundaries (Coble creep), is dependent on diffusion coefficients, which in turn follow an Arrhenius-type temperature dependence. The dislocation creep rate is increased with increasing temperature as a result of greater ease of dislocation cross-slip and climb. Each of these processes has an associated activation energy, which is often the activation energy for self-diffusion. On this basis, secondary creep rate ($\dot{\varepsilon}_s$) has been related to stress and temperature using a power law expression:

$$\dot{\varepsilon}_s = A \left[\sigma_a/E(T) \right]^n \exp(-Q_c/RT) \qquad (1)$$

where σ_a is the applied stress, n is the stress exponent (3 to 5 for metallic solid solutions), E(T) is Young's modulus corrected for temperature, Q_c is the apparent activation energy for creep, and A is a structure/material constant. In precipitation hardened materials, such

as superalloys, n has been found to range from 6 to 75 and to be temperature dependent, and Q_c has been reported to be several times larger than the activation energy for self-diffusion. An alternate form for power law creep has been suggested for precipitation hardened alloys [37, 38, 39, 40]:

$$\dot{\varepsilon}_s = A' [(\sigma_a - \sigma_r)/E(T)]^n \exp(-Q/RT) \qquad (2)$$

where σ_r is the "resisting stress" from the precipitates, Q is the activation energy for creep, and A' is another structure/material constant. The quantity $(\sigma_a - \sigma_r)$ represents the "effective stress" acting on the glide dislocations. With this modification, the value of n is 3 to 4 and independent of stress, and Q is equal to the activation energy for self-diffusion. The magnitude of the resisting stress is a function of temperature and microstructure.

To summarize this overview, it should be emphasized that mechanical properties are related to microstructure. Tensile and creep rupture properties of superalloys can be enhanced by optimizing the fraction, distribution, and composition of the microconstituents. As has previously been stated, a high volume fraction of uniformly dispersed, fine gamma prime precipitates provides maximum creep rupture resistance. The diffusion coefficients, and, therefore, the contribution of thermally assisted deformation mechanisms, can be decreased by the additions of certain alloying elements, with refractory metals being effective for reducing lattice diffusion and B and Zr being effective for reducing grain boundary diffusion. Solid solution additions to gamma and gamma prime affect the gamma/gamma prime mismatch, strength of the individual phases, stacking fault energy, and the APB energy of gamma prime. While small, discrete intergranular carbides

inhibit grain boundary sliding, other carbide forms are very deleterious to mechanical properties, particularly ductility. In light of these many interrelationships, mechanical property data must be considered with an understanding of the changes in microstructural features when any modifications are made to alloy composition or processing.

Overview of the Present Study

Tantalum additions have been made to nickel-base superalloys in order to improve their mechanical properties by altering their microstructures. Tantalum is a strong MC carbide forming element and can be expected to alter the type or types of MC carbides present, their stability, and possibly the secondary carbide precipitation. Tantalum is thought to partition to the gamma prime phase, where its addition would be anticipated to increase the volume fraction of gamma prime and strengthen the gamma prime by solid solution hardening and possibly changes in the APB energy. The Ta present in the gamma phase may also add an increment of strengthening by solid solution hardening and decreasing the rate of thermally assisted deformation by slowing down diffusion. The secondary effects of Ta additions, such as alterations in the distribution of other alloying elements among the gamma, gamma prime, and carbide phases, may also have a role in the observed Ta effects.

The primary goal of this research was to examine the effects of Ta on the microstructure and high temperature mechanical properties of both equiaxed and directionally solidified MAR-M247. A secondary part of this study was to determine the effects of Ta on the microstructure of another cast nickel-base superalloy, B-1900 + Hf. B-1900 + Hf and MAR-M247 nominally contain 4.0 and 3.0 weight percent Ta, respectively,

and otherwise differ significantly only in their Mo and W contents (see Table 1). Several recent studies [27, 41] have examined the effects of Ta on single crystal MAR-M247, but the alloy series were stripped of the grain boundary strengtheners B, Hf, Zr, and in some cases, C. By combining the results of these two previous studies with the results of this study on B-1900 + Hf and MAR-M247 in polycrystalline form and with grain boundary strengtheners, a broader understanding of the "Ta effect" in nickel-base superalloys can be attained. This information is not only desirable from the standpoint of achieving a fundamental understanding of the beneficial effects of Ta, but it will also allow guidelines to be formulated in the search for potential substitutes for this strategic element.

Table 1: Nominal Alloy Compositions

B-1900 + Hf

	C	Cr	W	Co	Mo	Al	Ti	Ta	Zr	B	Hf	Ni
w/o	0.10	8.00	--	10.00	6.00	6.00	1.00	4.00	0.100	0.015	1.25	Bal.
a/o	0.48	8.78	--	9.69	3.57	12.70	1.19	1.26	0.063	0.079	0.40	61.79

MAR-M247

	C	Cr	W	Co	Mo	Al	Ti	Ta	Zr	B	Hf	Ni
w/o	0.15	8.50	10.00	10.00	1.00	5.50	1.00	3.00	0.100	0.015	1.50	Bal.
a/o	0.75	9.78	3.25	10.15	0.62	12.19	1.25	0.99	0.066	0.083	0.50	60.36

EXPERIMENTAL PROCEDURE

A. Materials

The MAR-M247-type alloys used in this study were prepared from a master metal heat based on MAR-M247 supplied by Cannon-Muskegon Corporation. The master metal was cast without C, Hf, Ta, B, and Zr. These five elements were added to the vacuum furnace charge in order to vary their levels in the final compositions of the seven polycrystalline alloys in the present study and the six single crystal alloys that were utilized in another study. The melt additions and casting of all the MAR-M247-type alloys were performed by Howmet Turbine Components Corporation. Two directionally solidified (DS) alloys were cast using the withdrawal process with the growth axis approximately parallel to [001]. Alloy C contained zero tantalum and alloy D contained the normal Ta level of about 1 atomic percent or 3 weight percent (see Table 2). The equiaxed alloys were cast in inoculated shell molds with two different inoculants. It has been observed in superalloys that while inoculants affect the surface grain size, they have no effect on the internal grain size. Two low Ta alloys and one normal Ta alloy were cast using the inoculant for fine surface grain size, and two normal Ta alloys were cast utilizing the inoculant for coarser surface grain size. Regardless of inoculant, the cast-to-shape equiaxed tensile bars had a columnar grain structure that was oriented radially to the specimen axis. It should be noted from the compositions contained in Table 2 that Al, Ti, Cr and Co also systematically increased as Ta was added to the alloys.

Table 2: Alloy Compositions
(Atomic Percent)

		C	Cr	W	Co	Mo	Al	Ti	Ta	Zr	B	Hf	Ni
B-1900 + Hf	A	0.52	8.45	--	9.58	3.57	13.40	1.74	1.34	0.019	nil	0.49	60.88
	B	0.47	8.46	--	9.48	3.59	12.92	1.78	0.67	0.019	nil	0.50	62.13
	C	0.51	8.77	--	9.63	3.63	12.68	1.79	0.00	0.018	nil	0.48	62.50
MAR-M247	A1	0.54	9.58	3.01	9.59	0.31	10.80	1.08	0.07	0.045	0.071	0.51	64.41
(Equiaxed)	A2	0.54	9.61	2.98	9.63	0.31	10.99	1.08	0.23	0.052	0.033	0.50	64.05
	B1	0.50	9.98	3.16	10.33	0.36	12.05	1.17	0.88	0.046	0.105	0.56	60.86
	B2	0.50	9.90	3.11	9.95	0.35	11.58	1.12	0.71	0.052	0.105	0.52	62.11
	B3	0.45	9.76	3.14	9.97	0.36	12.22	1.14	0.87	0.046	0.066	0.43	61.56
MAR-M247	C	0.49	9.37	3.00	9.41	0.30	10.61	0.94	0.00	0.036	0.060	0.40	65.38
(D.S.)	D	0.51	9.57	3.11	9.75	0.35	11.86	1.02	0.97	0.036	0.072	0.41	62.35

The equiaxed B-1900 + Hf-type alloys were supplied by TRW, Incorporated. The compositions of these three alloys are also contained in Table 2. Alloy C contains zero Ta while alloys B and A contain one-half and the normal Ta level (about 1.34 atomic percent), respectively.

B. Heat Treatment

The gamma prime solvus temperatures were determined by heat treating thin ($\sim$ 1mm) disks of each alloy for four hours in 25°C increments near the solvus temperature, followed by a water quench. The lowest temperature that resulted in the complete dissolution of the coarse as-cast gamma prime was used as the solutionizing temperature (see Table 3). Differential thermal analysis was not utilized because of the difficulties in interpreting the many transition temperatures present in these alloys, most of which are heating rate dependent. All alloys were solutionized without the occurrence of any incipient melting. As is shown in Table 3, the addition of Ta increased the gamma prime solvus temperature in both MAR-M247 and B-1900 + Hf.

The bars for microstructural studies and mechanical testing were solutionized for four hours at temperature in still air. It took approximately one-half hour to move the samples into the furnace hot zone. The bars were then quenched with an argon spray. All alloys were given the standard MAR-M247 aging treatment of 20 hours at 871°C followed by an air cooling. The temperatures were kept within 5°C of the intended values during both the solutionizing and aging heat treatments.

C. Metallography and Microscopy

Specimens for optical and scanning electron microscopy (SEM) were mechanically ground through 600 grit silicon carbide paper. The final

Table 3: Heat Treatment Schedule

Alloy		Solution Treatment
B-1900 + Hf	A	1250°C/ 4 hours, argon quench
	B	1250°C/ 4 hours, argon quench
	C	1225°C/ 4 hours, argon quench
MAR-M247 (Con. Cast)	A	1225°C/ 4 hours, argon quench
	B	1250°C/ 4 hours, argon quench
MAR-M247 (D.S.)	C	1225°C/ 4 hours, argon quench
	D	1250°C/ 4 hours, argon quench

All alloys were aged at 871°C for 20 hours and air cooled

polishing consisted of 6 micron diamond paste and 0.05 micron alumina slurry. The etchants employed were Marble's reagent and a solution of 33% nitric acid, 33% acetic acid, 33% distilled water and 1% hydrofluoric acid. Marble's reagent consists of 50ml hydrochloric acid, 50ml distilled water and 10g hydrated copper sulfate. In some cases, this solution was diluted with water.

Thin foils for transmission electron microscopy (TEM) and scanning transmission electron microscopy (STEM) were initially mechanically ground to approximately 0.15 mm in thickness. The 3mm diameter punched disks were then thinned with a Fischione twin-jet electropolisher. The electrolyte was a fresh solution of 10% perchloric acid in absolute ethanol with a current of approximately 40 mA. It was found that the best polishing temperature varied between -35°C and -15°C, with the lower temperatures being preferred for the low Ta alloys. The operating voltage was a strong function of solution temperature.

The SEM was performed with a JEOL 35C instrument equipped with a KEVEX 8000 energy dispersive x-ray system. A software computer program, MAGIC V, was used to correct and quantify the x-ray data. The thin foil specimens were examined with a JEOL JEM-100CX TEM/STEM at accelerating voltages of 80, 100, or 120 kV. A KEVEX 7000 energy dispersive x-ray system with suitable software was used for STEM microanalysis.

D. Phase Extraction

The phase extractions were performed using a modification of the standard techniques [27, 44]. Disks weighing approximately 1 gram were ground through 600 grit silicon carbide paper and electropolished with a solution of 20% sulfuric acid in methanol at room temperature. This treatment was used to remove surface oxides and any possible strain

effected layers. The disks were then cleaned and weighed. Each specimen was suspended in a weighed beaker containing an aqueous solution of 1% ammonium sulfate and 1% citric acid. The entire sample, except for the small portion in an alligator clip above the solution, was dissolved. A stainless steel cathode and a current density of $1mA/mm^2$ were used. The residue, containing the gamma prime and minor phases, was allowed to settle for several days before decanting the solution. After rinsing with distilled water, the residue was dried and weighed in the beaker. The gamma prime was then dissolved with a solution of 50% hydrochloric acid in methanol. The beaker contents were again rinsed, dried, and subsequently weighed. The weight fraction of gamma prime and minor phases, predominately MC carbides, was obtained by dividing the respective residue weights by the weight of the dissolved portion of the sample. Three measurements were made for each alloy.

E. Phase Composition and Identification

The compositions of the microconstituents were determined by a combination of direct measurement and mass balance. The composition of the gamma prime and minor phase residue was determined with the inductively coupled plasma, atomic-emission-spectroscopy technique by NASA-Lewis Research Center in Cleveland, Ohio. Chemical analysis of the minor phase residue was performed with the EDS system on the SEM. Knowing the phase fractions, bulk alloy composition, and the gamma prime and carbide residue compositions, the gamma and gamma prime phase chemistries were calculated based on mass balance.

X-ray diffraction was used to determine the gamma prime lattice parameters and to identify the phases present in the minor phase residue. The Debye-Scherrer method was utilized for the gamma prime

lattice parameter and a diffractometer was employed with a scan rate of 1°/minute for the minor phases. In both cases, filtered Cu K_α radiation was used. The lattice parameters were calculated using Cohen's method. The minor phases were identified by comparing the peak positions and intensities with data in the literature.

The compositions of individual MC carbides were analyzed in-situ with EDS in the SEM. However, to minimize the matrix contribution to the x-ray signal, the in-situ EDS was limited to particles larger than about 1 micron in size.

F. Mechanical Testing

Hot tensile tests were carried out at 540°C (1000°F), 760°C (1400°F), and 982°C (1800°F) on the heat treated MAR-M247 type alloys. Alloys A1 and B1 were selected from the five conventionally cast alloys for all mechanical testing. The testing was done in air in accordance with ASTM specification E21-79. The 0.2% offset yield stress, ultimate tensile stress, percent elongation, and reduction in area were measured.

The creep rupture testing was carried out under constant stress at 760°C (1400°F), 871°C (1600°F), and 982°C (1800°F) in air on the MAR-M247-type alloys. The stress levels were selected to maximize the range of rupture times and steady-state creep rates. Testing was terminated either at rupture or after a specified number of hours. The creep rupture testing was performed according to ASTM E139-79. All high temperature mechanical testing was performed by Joliet Metallurgical Laboratory, Joliet, Illinois.

RESULTS

A. Microstructure and Phase Compositions

1. As-Cast Microstructure

The microstructures of as-cast MAR-M247 and B-1900 + Hf are composed of gamma, gamma prime, MC carbides, and gamma/gamma prime eutectic regions. These microconstituents are shown in the SEM micrograph of Figure 1. The eutectic regions either take the form of coarse degenerate pools or fine gamma/gamma prime rosettes. The coarse gamma prime in all cases is cuboidal and approximately 1 micron in size. It appears dark and etched back from the gamma matrix. The MC carbides appear as white particles in relief.

The gamma/gamma prime eutectic regions are non-equilibrium solidification products which are located primarily along the grain boundaries. The morphology of the eutectic pools is a function of Ta content in the B-1900 + Hf-type alloys; a dependency of eutectic morphology on Ta concentration was not observed in either the conventionally cast or DS MAR-M247. A typical structure for the MAR-M247-type alloys, regions of both degenerate gamma/gamma prime and fine gamma/gamma prime rosettes, is shown in Figure 2. When Ta is present in the B-1900 + Hf-type alloys, a portion of the eutectic regions are degenerate, with the remaining eutectic being of the rosette type. A reduction in the Ta concentration to one-half of the original level decreases the volume fraction of degenerate eutectic in the alloy from 7.8% to 2.5%. The absence of Ta eliminates the degenerate structure altogether. Figure 3 illustrates this progression in eutectic pool morphology with Ta variation. EDS analysis of the eutectic pools in both alloy series shows that they are rich in Ta, Ti, Hf, and Al and depleted of W, Mo

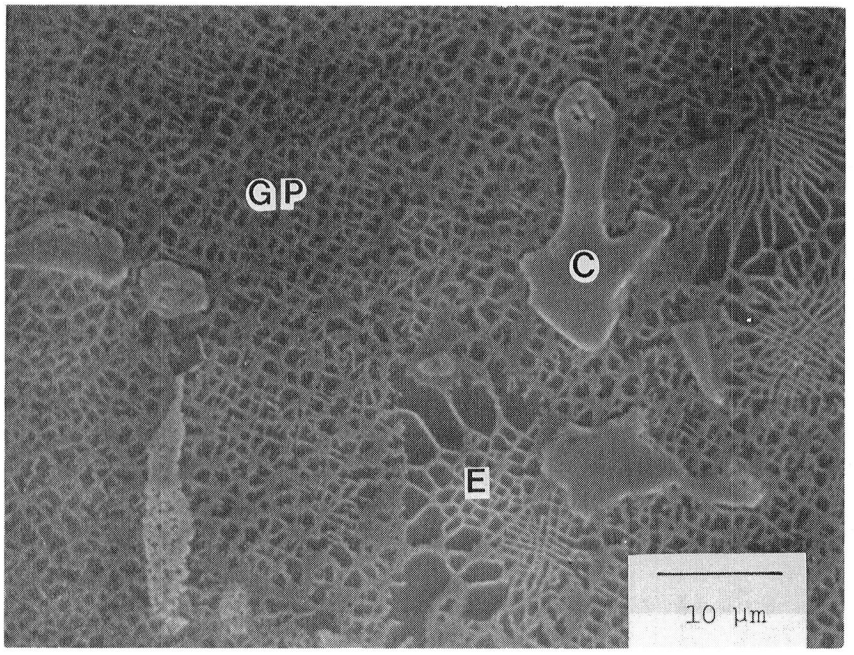

Figure 1: SEM micrograph of the normal Ta B-1900 + Hf alloy in the as-cast condition. Note the gamma/gamma prime eutectic (E), the coarse gamma prime (GP) and the MC carbides (C).

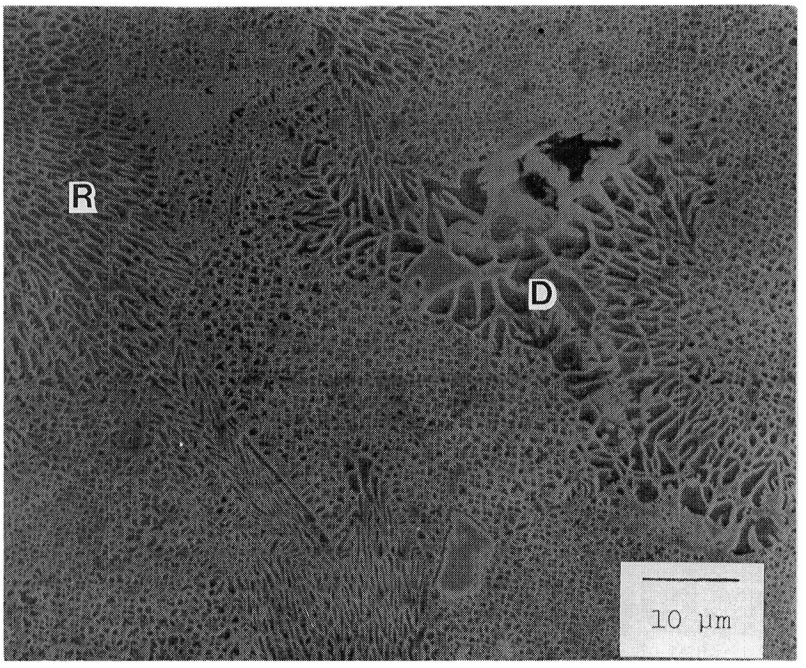

Figure 2: SEM micrograph of the normal Ta DS MAR-M247 alloy in the as-cast condition. Note the degenerate (D) and rosette-type (R) gamma/gamma prime eutectic regions.

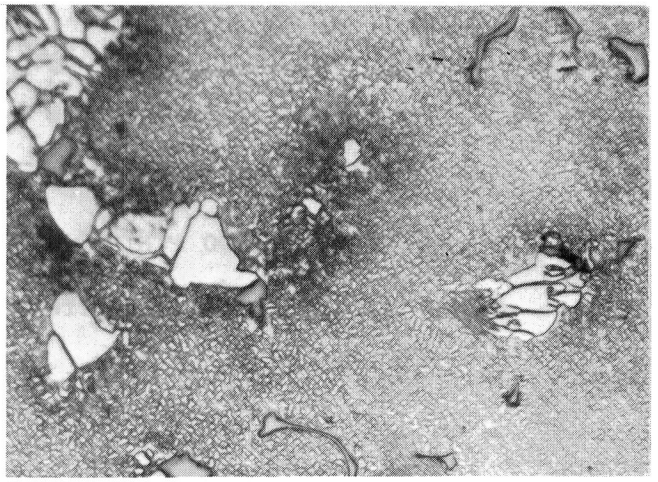

1.34 a/o Ta

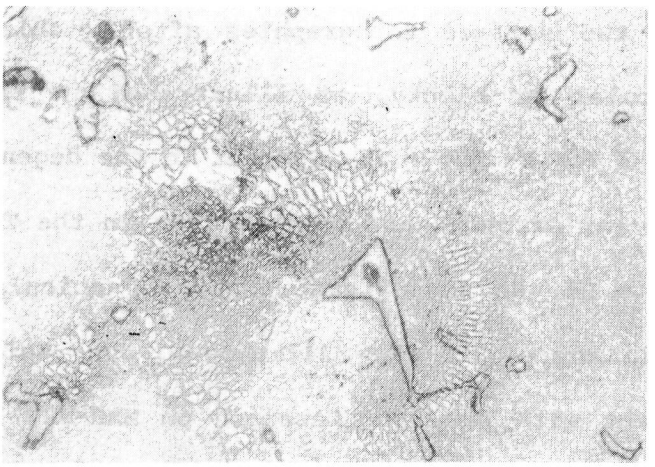

0.67 a/o Ta

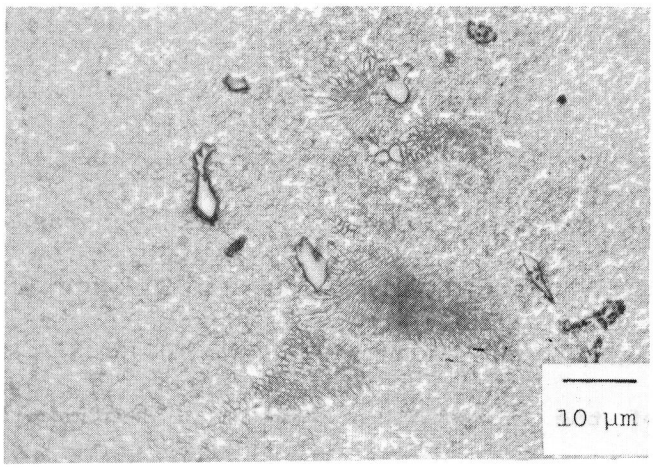

0.00 a/o Ta

Figure 3: Optical micrographs of the B-1900 + Hf-type alloys in the as-cast condition. Note the change in the eutectic morphology as a function of Ta content.

(when they are present in significant amounts in the alloy), Cr, and Co. These observations are consistent with the dendritic segregation observed in single crystal MAR-M247 [27, 41]. The degree of segregation in the as-cast structure is greater in the B-1900 + Hf-type alloys than in the MAR-M247-type alloys (possibly a result of different casting practice), with the degenerate eutectic regions being more heavily cored than the rosette structure in the same alloy.

The MC carbides in MAR-M247 (DS and equiaxed) and B-1900 + Hf have two morphologies and two surface topographies after etching. The MC carbides can be acicular or blocky, as illustrated in the optical micrographs of Figure 3 for B-1900 + Hf. Similar to the degenerate eutectic pools, the acicular carbides are only present in the Ta containing alloys of B-1900 + Hf. No significant number of acicular MC carbides were observed in any of the MAR-M247-type alloys. This observation is in disagreement with previous research on MAR-M247 (with Hf) [45], and is probably due to a difference in cooling rates employed during casting [14]. The surface topography of the MC carbides were either smooth or mottled as shown in Figure 4. Both alloy systems contained carbides with the two surface topographies. In-situ EDS analysis showed some correlation between surface topography and composition; smooth carbides tended to be Ta or Ti-rich and mottled carbides contained significant amounts of Hf. The EDS results also indicate that many of the MC carbides have a Hf-rich mottled shell around them.

The x-ray diffraction phase identification from the minor phase residues indicates that MC carbides are the major constituent of the residue and that the MC carbide type is a function of Ta level. Table 4

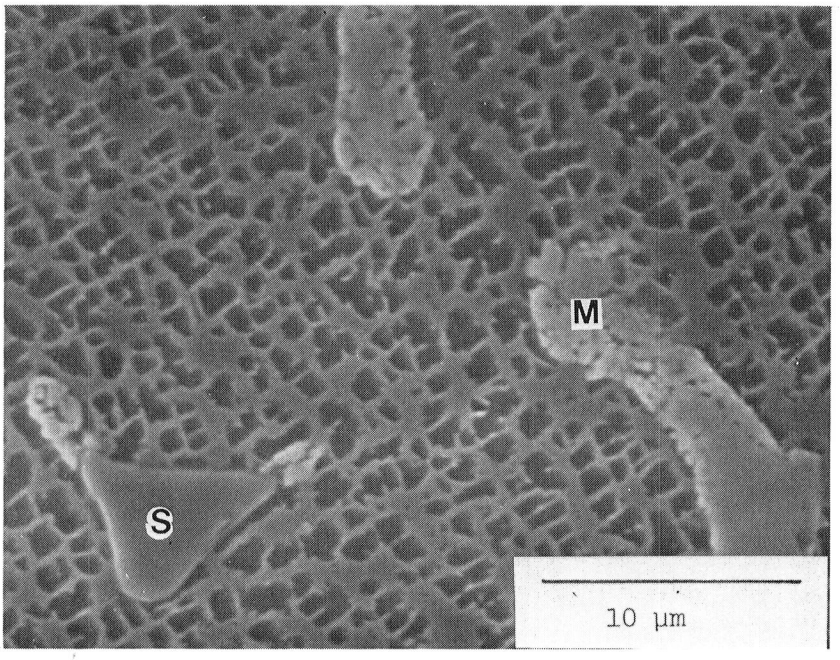

Figure 4: SEM micrograph of the normal Ta B-1900 + Hf alloy as-cast showing the two MC carbide surface topographies, mottled (M) and smooth (S).

Table 4: Lattice Parameters of MC Carbides in the As-Cast Alloys

Alloy		Bulk Ta Level (a/o)	Abundant MC		Less-Abundant MC	
			a (nm)	relative intensity	a (nm)	relative intensity
B-1900 + Hf	A	1.34	0.440	vs	0.450	vw
	B	0.67	0.439	vs	0.451	m
	C	0.00	0.458	vs	0.435	m
MAR-M247	A1	0.07	0.458	vs	0.437	w
(Con. Cast)	B1	0.88	0.439	vs	0.451	vw
MAR-M247	C	0.00	0.457	vs	0.437	m
(D.S.)	D	0.97	0.440	vs	0.451	vw

vs:very strong s:strong m:medium w:weak vw:very weak

lists the MC carbide lattice parameters and their respective relative intensities for the as-cast alloys. Because Ti, Ta, and Hf are the strong MC carbide forming elements contained in B-1900 + Hf and MAR-M247, an analysis to identify the MC carbides in Table 4 can be attempted using the lattice parameters of the pure MC carbides of these three strong MC carbide formers. The lattice parameters of HfC, TiC, and TaC are 0.464, 0.433, and 0.446 nm, respectively. The lattice parameter of the abundant* MC carbide in both as-cast alloy series shifts from 0.457-0.458 nm to 0.439-0.440 nm when Ta is added to the alloy. It is suggested, on the basis of the large lattice parameter, that the abundant MC carbide in the zero Ta alloys is Hf-rich. The lattice parameter of the abundant MC carbide in the Ta-containing alloys is intermediate to that of TaC and TiC, and therefore is thought to be a mixed Ta/Ti-rich MC carbide. The in-situ EDS confirms that the abundant MC carbide in the zero Ta alloys is approximately 80 atomic percent (of the metallic elements) Hf, and the abundant carbide in the Ta-containing alloys is approximately 40 atomic percent each of Ta and Ti, with the remainder being Hf, Mo, and W. The lattice parameter of the less-abundant* MC carbide goes from 0.435-0.437 nm to 0.450-0.451 nm as Ta is added. This suggests that the less-abundant carbide changes from Ti-rich to a mixed Ta/Hf-rich MC carbide as bulk Ta increases. Again, in-situ EDS confirms the analysis of the x-ray data; the less abundant carbide is about 75 atomic percent Ti with some W and/or Mo in

---

*The terms "abundant" and "less-abundant" MC carbide will be used to indicate the relative intensities of the peaks in the x-ray diffraction patterns. The "abundant" carbide has greater intensity and, therefore, would be expected to be present in the larger volume fraction and vice-versa for the "less abundant" carbide.

the zero Ta alloys and approximately 45 atomic percent each of Ta and Hf when Ta is added. No borides or other minor phases were positively identified by x-ray diffraction, although many low intensity peaks in the diffraction scans remained unidentified.

The compositions of the minor phase residue, which will henceforth be referred to as the carbide compositions, shown in Figure 5, indicate that as Ta is added to the as-cast B-1900 + Hf and MAR-M247-type alloys, part of the Hf is replaced by Ta. The concentrations of the other elements, Ti, W, and Mo remained nearly constant. These results are in agreement with the interpretation of the x-ray diffraction data and in-situ EDS analysis that the abundant MC carbide shifts from Hf-rich to Ta-rich with Ta additions.

The addition of Ta to as-cast MAR-M247 (conventionally cast and DS) and B-1900 + Hf causes an increase in the gamma prime lattice parameter, as shown in Figure 6. Although the data for the two alloy systems lay on slightly different lines, the lattice parameter data indicates that the gamma prime phase compositions of B-1900 + Hf and MAR-M247 are changing in a similar manner with Ta additions. Increases in the Ta and Hf (the latter from the MC carbides) levels with Ta additions to the bulk material are likely possibilities for the implied changes in precipitate composition.

2. Heat Treated Microstructure

The solutionizing and aging heat treatments completely dissolved the gamma/gamma prime eutectic and coarse gamma prime that was present in the as-cast material. A typical fully heat treated microstructure is shown in Figure 7. Incipient melting was not noted from the single temperature solution treatment, which is in disagreement with results

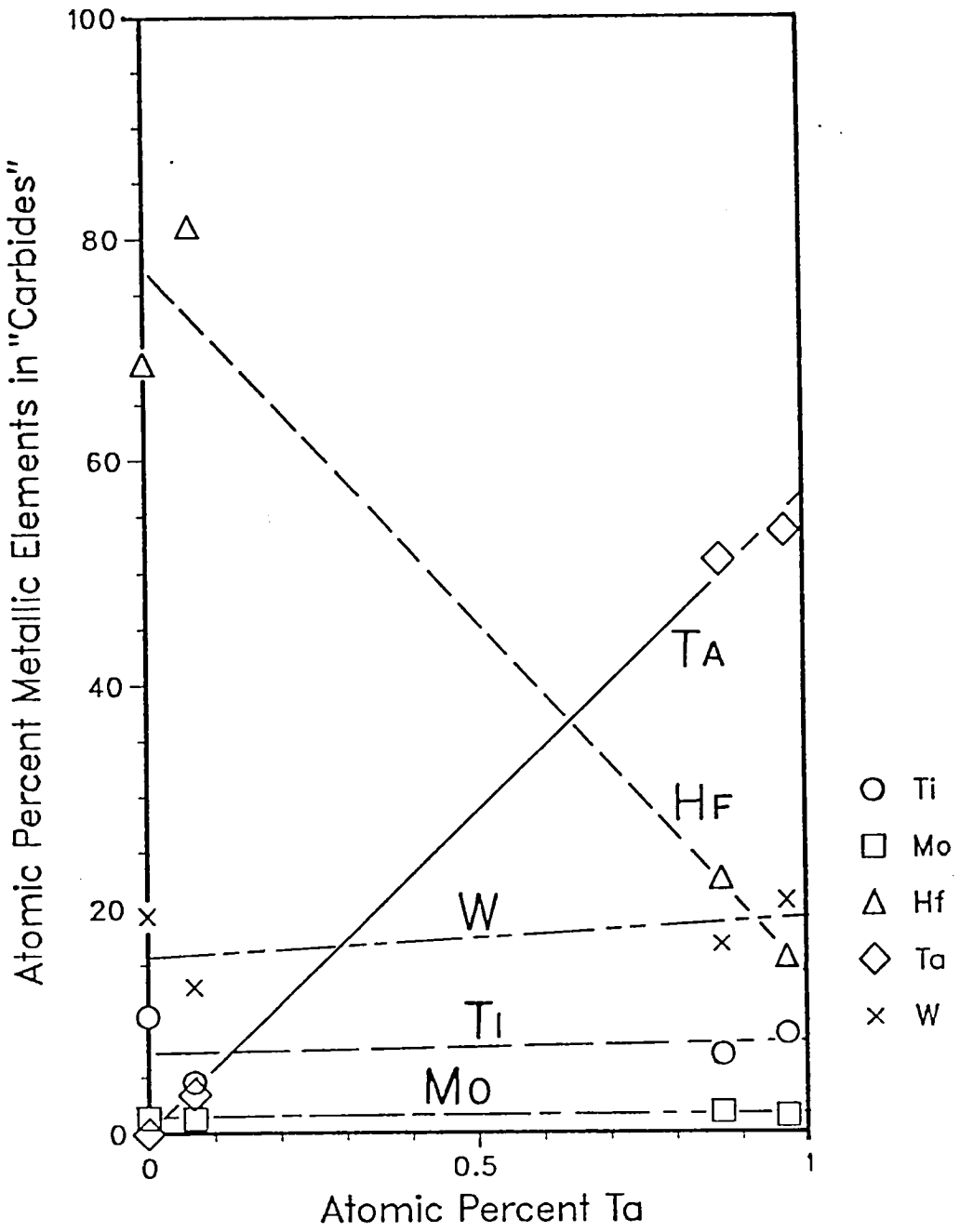

Figure 5a: Composition of the carbides in the as-cast MAR-M247-type alloys as a function of Ta level.

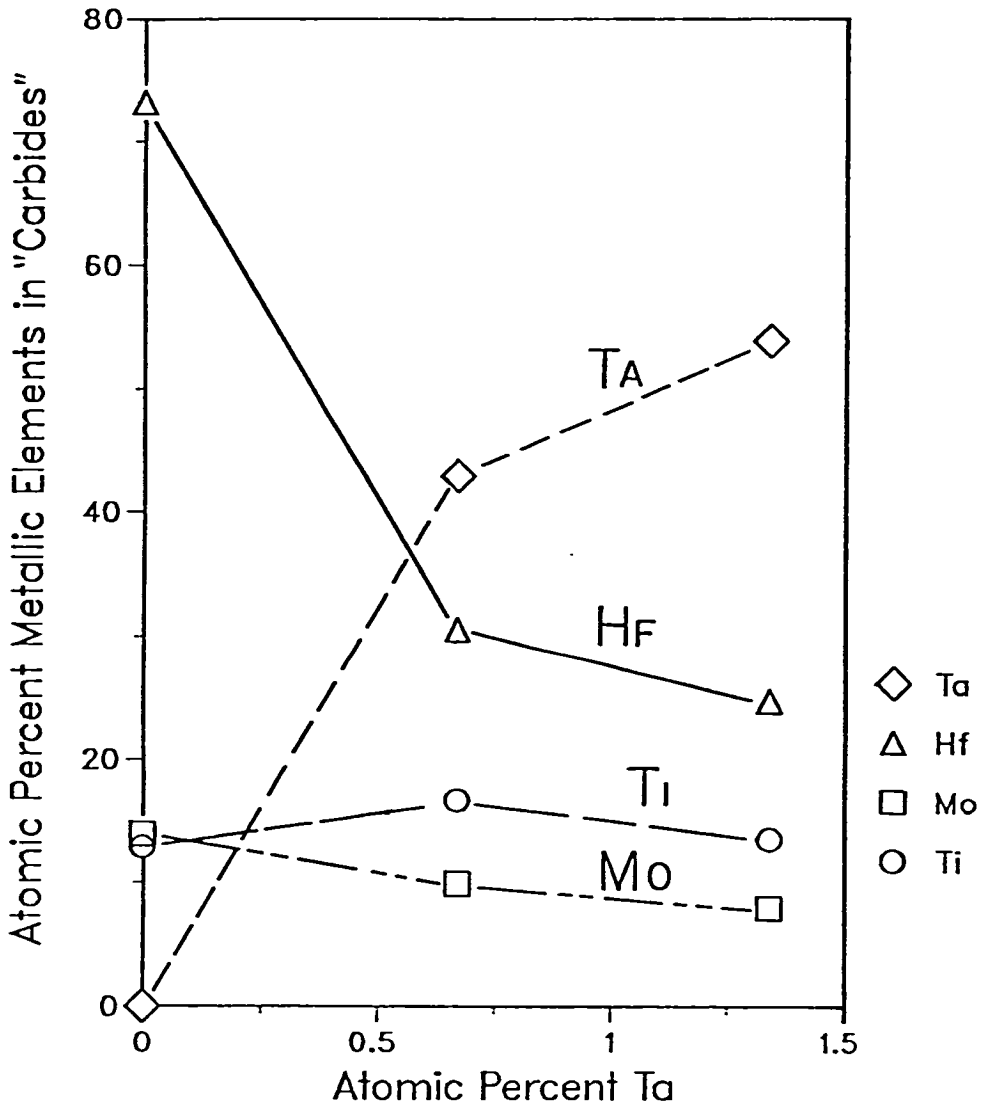

Figure 5b: Composition of the carbides in the as-cast B-1900 + Hf-type alloys as a function of Ta level.

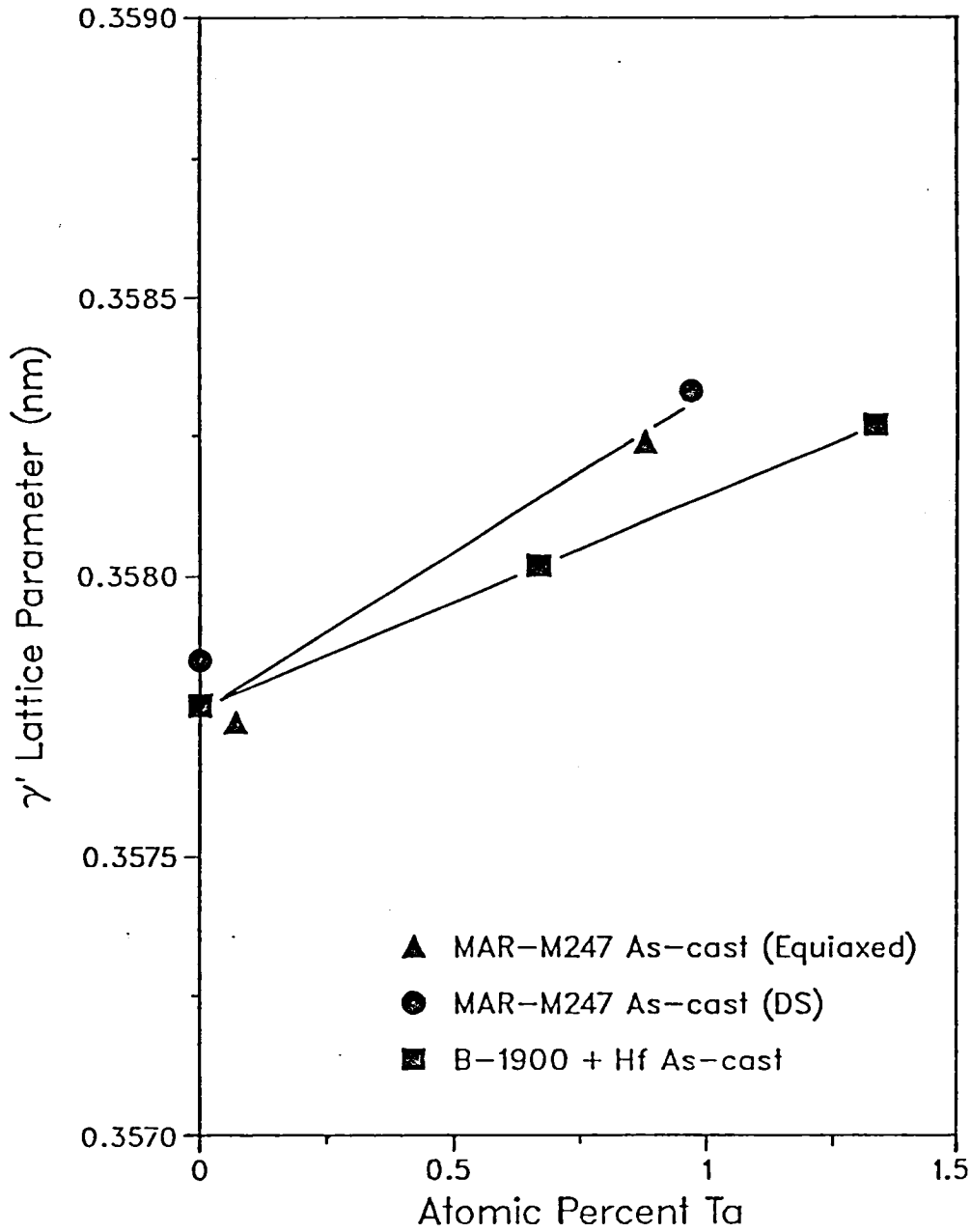

Figure 6: Gamma prime lattice parameters of the as-cast MAR-M247 and B-1900 + Hf-type alloys as a function of Ta level.

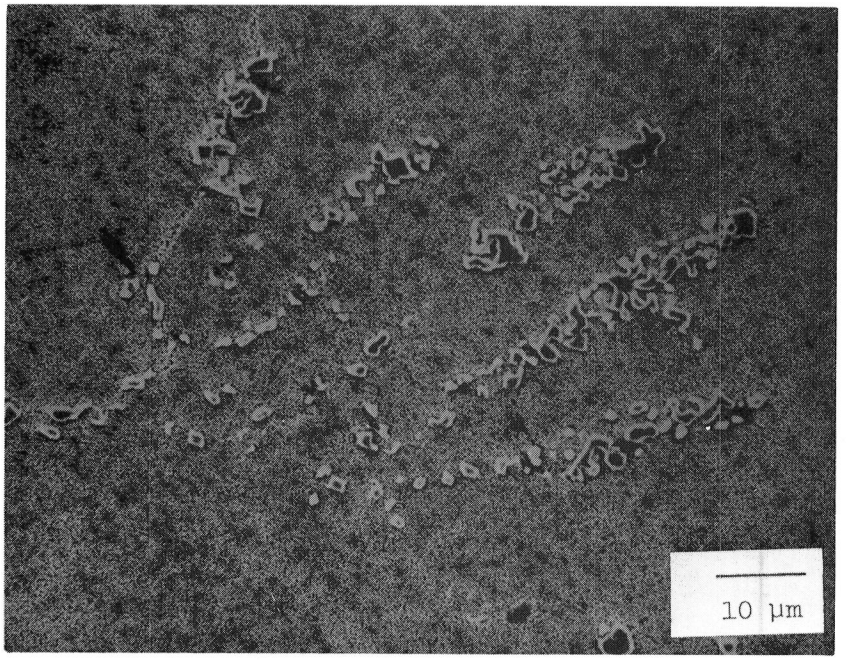

Figure 7: SEM micrograph of the normal Ta DS MAR-M247-type alloy in the heat-treated condition. Note the MC carbide breakdown and the fine gamma/gamma prime in the background (compare to Figure 2).

from a study on a MAR-M247 derivative alloy [45]. The capability to completely solutionize the as-cast structure without incipient melting in the present study is likely a result of the low heating rates employed (a necessary precaution when using alumina furnace tubes) and close temperature control.

Three additional changes were observed in the microstructures of MAR-M247 and B-1900 + Hf after heat treatment. In all of the alloys, the MC carbides, particularly the script type, degenerated into small particles as shown in Figure 7. This degeneration is typical of MC carbide breakdown after high temperature solution treatments [45, 46] or after long time aging at lower temperatures [12]. Secondly, strings of what appear to be very small (less than 1 micron) precipitates form in the zero Ta MAR-M247-type alloys. The additional precipitation, primarily in the area of MC carbides, is illustrated in the SEM micrograph of Figure 8. Lastly, a large number of low-angle grain boundaries, shown both by an optical and a TEM micrograph in Figure 9, formed in the zero Ta B-1900 + Hf alloy. Significant numbers of low angle grain boundaries were not observed in any other alloy.

The gamma prime lattice parameter in heat-treated B-1900 + Hf and MAR-M247-type alloys also increased with increasing Ta content as shown in Figure 10. Included in Figure 10 are the gamma prime lattice parameters for the as-cast materials. The gamma prime lattice parameter in the heat treated alloys increased linearly with Ta concentration, but the gamma prime lattice parameters for the two alloy series are very different, unlike the data for the two as-cast alloy series. Specifically, the gamma prime lattice parameter for B-1900 + Hf was increased by heat treatment compared to the as-cast B-1900 + Hf alloys. The

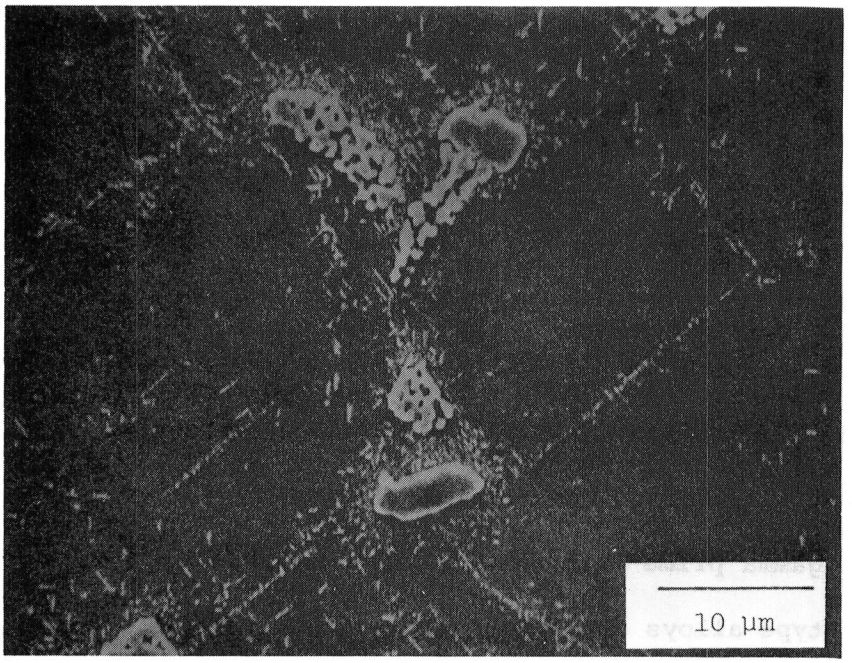

Figure 8: SEM micrograph of the zero Ta DS MAR-M247-type alloy in the heat-treated condition. Note the strings of precipitates and their greater density in the vicinity of the MC carbides.

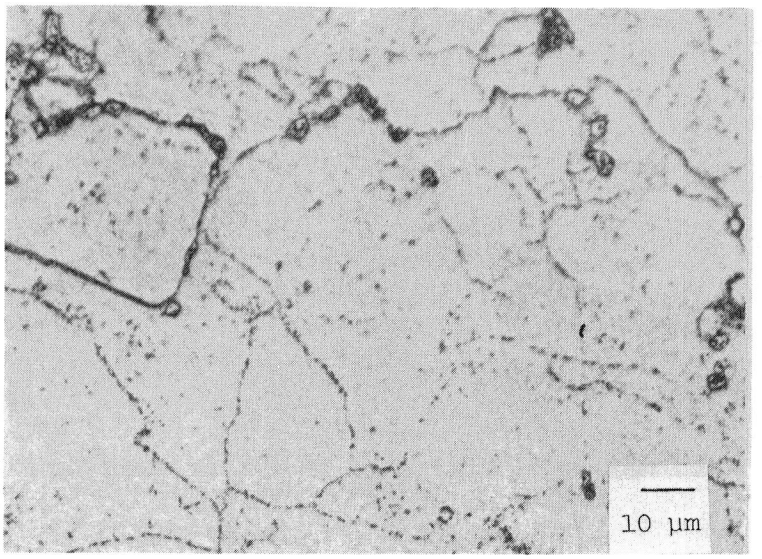

Figure 9a: Optical micrograph of the zero Ta B-1900 + Hf-type alloy in the heat treated condition. Note the presence of low-angle grain boundaries decorated with coarse gamma prime.

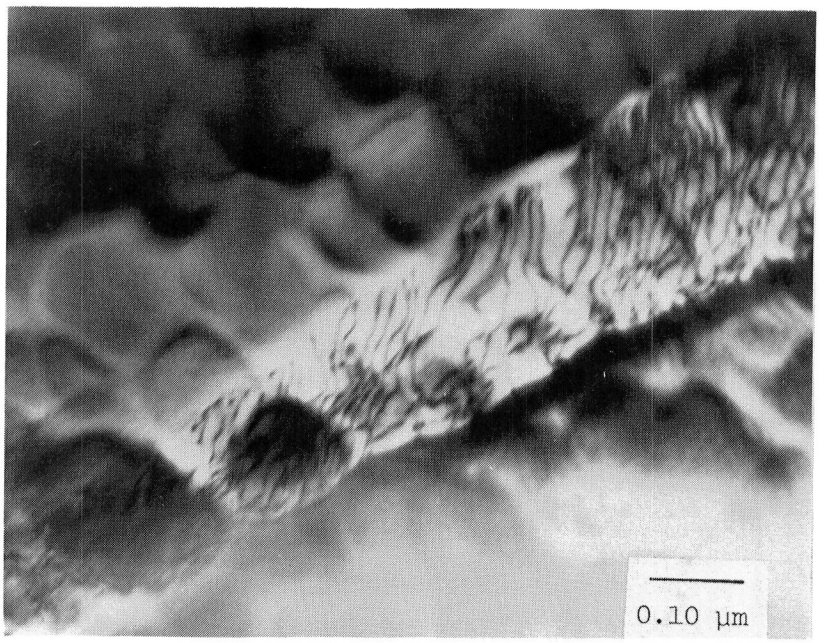

Figure 9b: TEM bright field micrograph of the zero Ta B-1900 + Hf-type alloy in the heat treated condition showing the structure of a low-angle grain boundary.

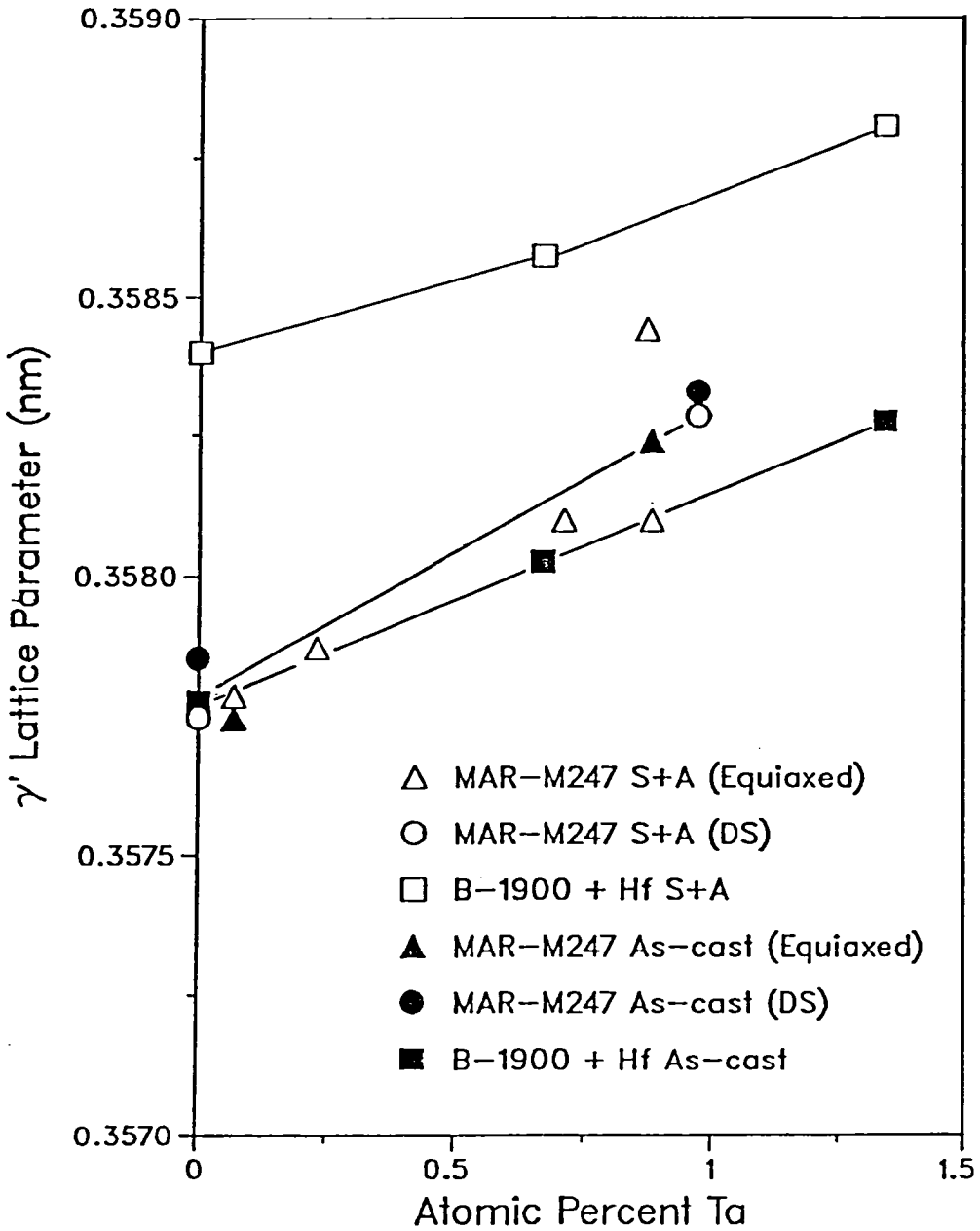

Figure 10: Gamma prime lattice parameters of the as-cast and heat treated B-1900 + Hf and MAR-M247-type alloys.

increase in the gamma prime lattice parameter may be caused by the solutionizing of non-equilibrium phases, such as Ni_5Hf, in the B-1900 + Hf eutectic pools.

The gamma prime morphology of the two heat-treated alloy series is very different, with the gamma prime morphology being cuboidal for all of the B-1900 + Hf-type alloys and spheroidal to flat-faced spheroidal with increasing Ta level for the MAR-M247-type alloys. The gamma prime morphologies are illustrated by the TEM micrographs of Figure 11. By coupling the room temperature lattice parameter data with the gamma prime morphology observations for MAR-M247, it is suggested that the gamma/gamma prime mismatch becomes more positive ($a_{\gamma'}$ larger than a_{γ}) with Ta additions at the heat treatment temperature. The mismatch may be positive or negative in the zero Ta alloys, but in either case is nearly zero. The cuboidal gamma prime morphology in all of the B-1900 + Hf-type alloys indicates that gamma/gamma prime mismatch of the B-1900 + Hf alloys is larger than that of the MAR-M247 alloys. The increasing gamma prime particle size with Ta additions, shown in Figure 12, may also have a small effect on the gamma prime morphology. These measurements, expressed as equivalent mean circular radius, were made by tracing TEM dark field images of gamma prime particles, such as those in Figure 11, and weighing the paper cuttings. This method gives only a mean particle size (area) and not the range and distribution in particle size within an alloy.

3. Carbide Phases After Heat Treatment

The x-ray diffraction data and in-situ EDS analyses of the heat treated MAR-M247 and B-1900 + Hf-type alloys indicate that, as Ta is added to both alloy systems, part of the Hf in the MC carbides is

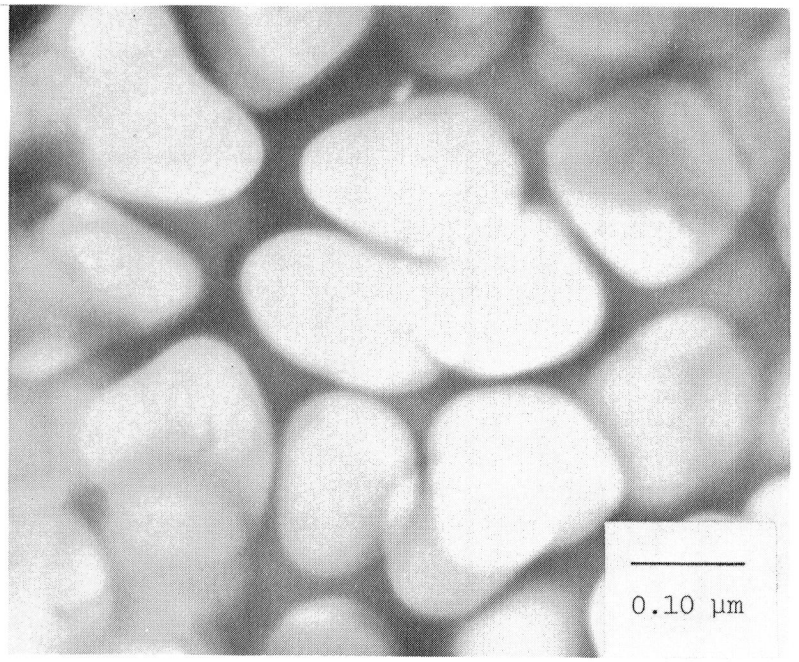

a

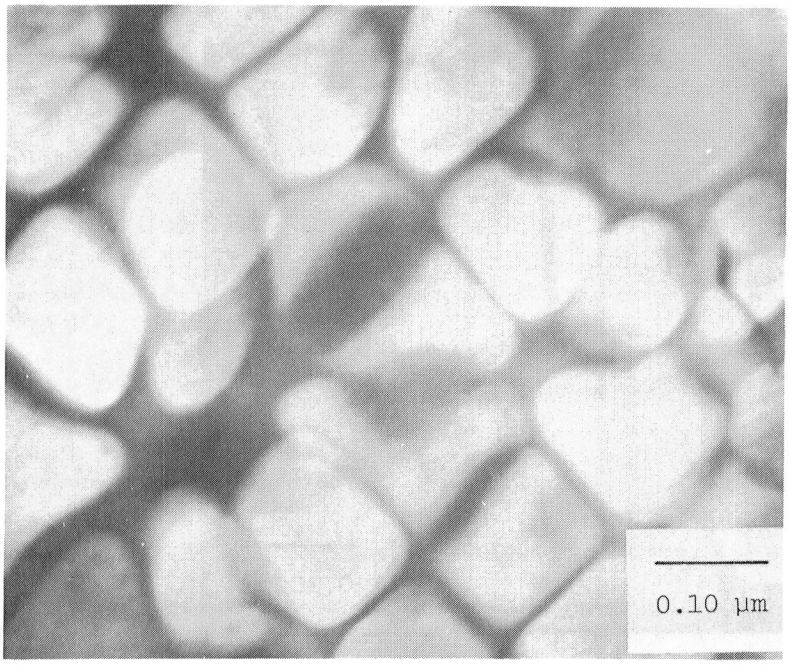

b

Figure 11: TEM dark field micrographs using a superlattice reflection showing the gamma prime morphology of (a) the zero Ta and (b) the normal Ta DS MAR-M247-type alloys.

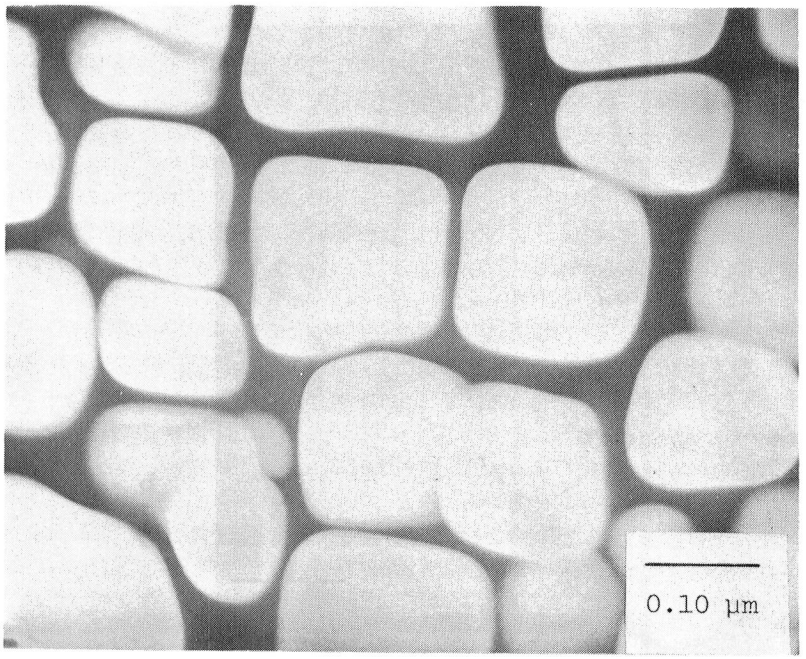

c

Figure 11c: (continued) TEM dark field micrograph using a superlattice reflection showing the gamma prime morphology of the normal Ta B-1900 + Hf alloy.

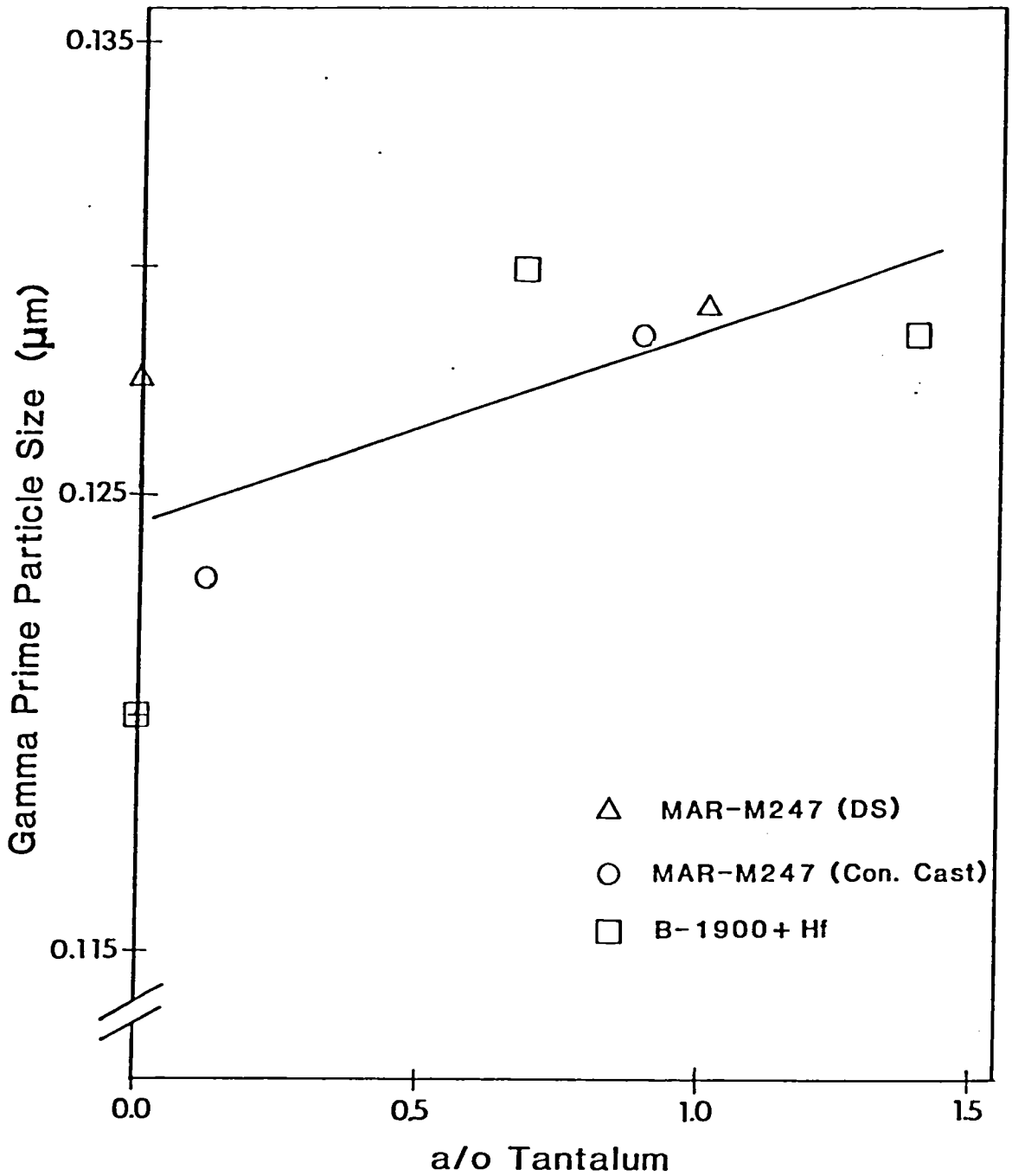

Figure 12: Equivalent mean gamma prime particle radius of the heat treated B-1900 + Hf and MAR-M247-type alloys as a function of Ta content.

replaced by Ta. The x-ray diffraction results, contained in Table 5, show that for the zero Ta alloys (alloys A1, A2, and C for MAR-M247 and alloy C for B-1900 + Hf), the abundant MC carbide has a lattice parameter of 0.461 to 0.462 nm and the less-abundant MC has a lattice parameter of 0.433 to 0.437 nm. Using the same analysis as for the carbides in the as-cast structure, it can be concluded from the lattice parameters that the abundant MC carbide is Hf-rich (a_{HfC}=0.464 nm) and the less-abundant MC carbide is Ti-rich (a_{TiC}=0.433 nm). In-situ EDS data confirms these conclusions; the abundant MC carbide is composed of 85 to 95 atomic percent (of the metallic elements) Hf and the less-abundant MC carbide contains approximately 60 atomic percent Ti, with the remainder being Mo and/or W with traces of Hf. When Ta is added to the alloys, both the abundant and less-abundant (when present) MC carbides are mixed Ta/Hf-rich, with a range in lattice parameters of 0.451 to 0.456 nm. Broad x-ray diffraction peaks and large in-situ EDS composition ranges are observed for the mixed Ta/Hf-rich carbides. The peak width, measured as the full width at half maximum (FWHM), for the mixed Ta/Hf MC carbides is typically 3 to 4 degrees (2θ). As a comparison, the nearly pure Hf-rich MC carbides from the zero Ta alloys have a FWHM of 1 to 2 degrees (2θ) at comparable 2θ angles and using the same reflection. The measured in-situ Hf levels in the mixed Ta/Hf carbides ranged from 20 to nearly 80 atomic percent. The apparent Hf inhomogeneities have been observed in the MC carbides of other Hf containing nickel-base alloys [8, 15, 16].

The composite carbide compositions, obtained from the extracted minor phase residue, in Figure 13, again illustrate that Ta replaces Hf in the MC carbides of both heat-treated alloy series. The Ti and Mo

Table 5: Lattice Parameters of MC Carbides in the Heat Treated Alloys

Alloy		Bulk Ta Level	Abundant MC		Less-Abundant MC	
		(a/o)	a_o (nm)	relative intensity	a_o (nm)	relative intensity
B-1900 + Hf	A	1.34	0.451	s	0.456	m
	B	0.67	0.454	vs	---	---
	C	0.00	0.462	vs	0.433	m
MAR-M247	A1	0.07	0.462	vs	0.435	w
(Con. Cast)	A2	0.23	0.462	vs	0.435	w
	B1	0.88	0.455	vs	---	---
	B2	0.71	0.456	vs	---	---
	B3	0.87	0.455	vs	---	---
MAR-M247	C	0.00	0.461	vs	0.437	m
(D.S.)	D	0.97	0.454	s	0.456	m

--- none detected

vs:very strong s:strong m:medium w:weak vw:very weak

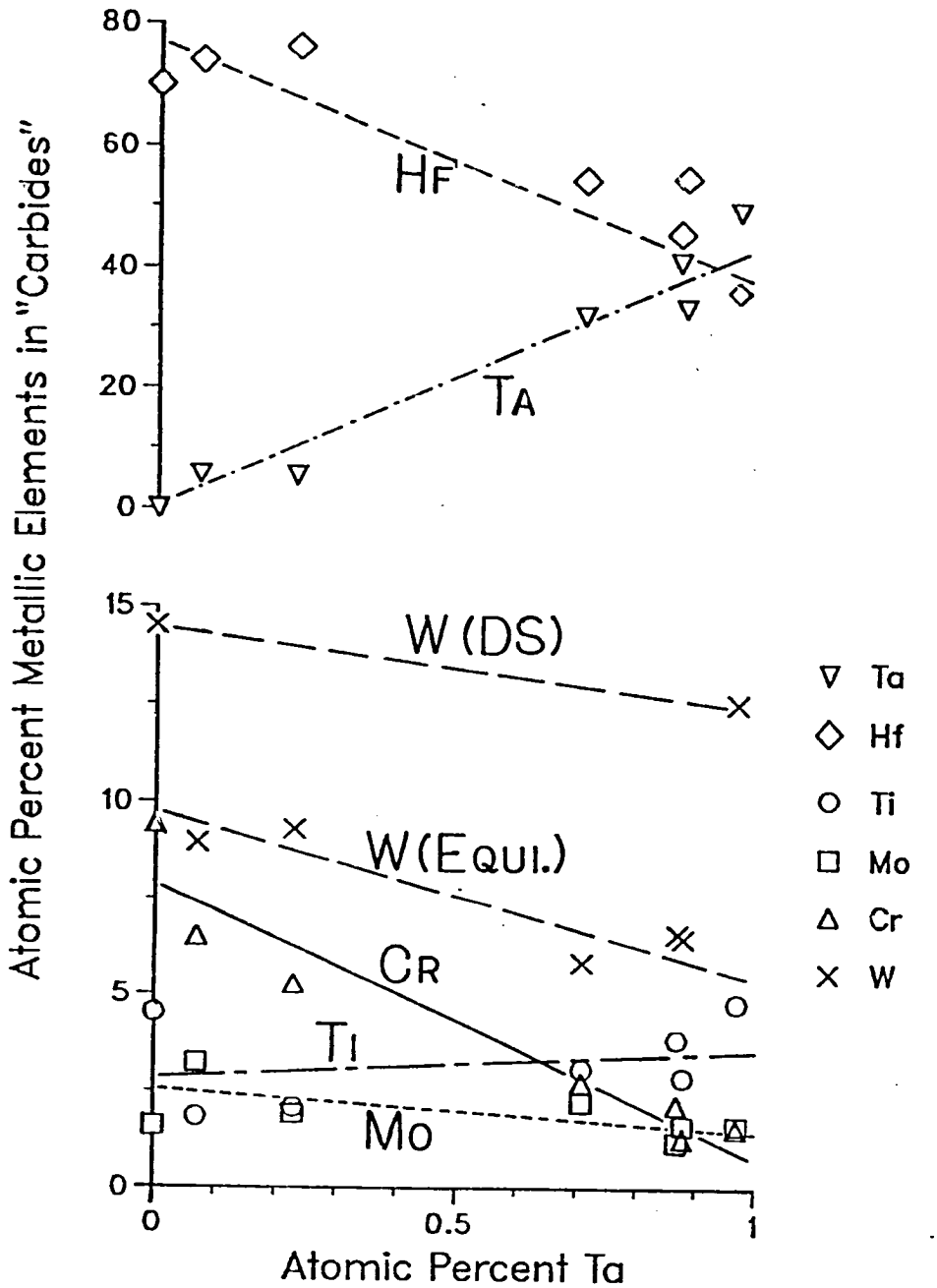

Figure 13a: Composition of the carbides in the heat treated MAR-M247-type alloys as a function of Ta content.

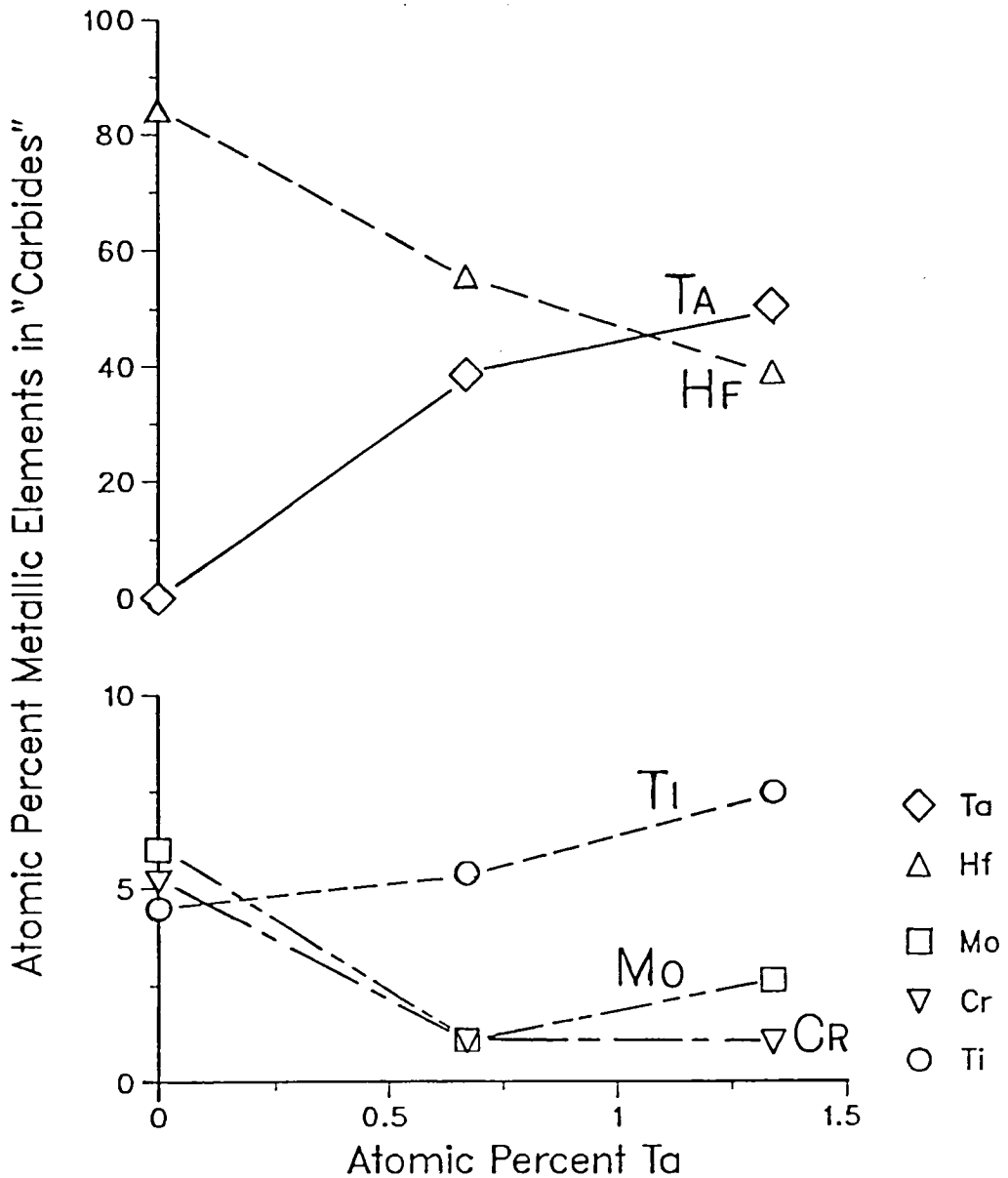

Figure 13b: Composition of the carbides in the heat treated B-1900 + Hf-type alloys as a function of Ta content.

levels in heat treated MAR-M247 remain basically constant and the W levels decrease slightly with Ta additions, although the W levels are slightly higher in the DS alloys than in the conventionally cast alloys. The Ti level also remained nearly constant in the B-1900 + Hf-type alloys, but the Mo level decreased with Ta additions. In addition, Cr is present in the carbide residue from both of the heat-treated alloys but was not observed in the carbide residue from the as-cast materials (see Figure 5) or in the in-situ MC carbide determinations.

Examination of the heat treated material with TEM showed the presence of an inhomogeneous distribution of secondary carbides in all B-1900 + Hf and MAR-M247-type alloys (see Figure 14); no similar secondary carbides were observed in the as-cast materials. The lattice parameter of these carbides was determined to be 1.071 nm, typical of $M_{23}C_6$ carbides, from electron diffraction studies. Limited STEM microanalysis showed that the Cr x-ray peak intensity increased substantially relative to the Co peak, an element not thought to be present in $M_{23}C_6$ carbides, in the vicinity of these carbides. Accurate quantitative analysis was not possible because the carbides are imbedded in the matrix phases. In addition, the presence of Cr only in the carbide residue from the heat treated alloys also indicates that the secondary carbides are Cr-rich $M_{23}C_6$ carbides. Three morphologies were observed: acicular, blocky, and in some cases, hexagonal. The bright field TEM micrograph and [100] zone axis electron diffraction pattern in Figure 14 show the acicular and blocky morphologies and the cube-on-cube ($\{100\}_{\gamma/\gamma'}$ // $\{100\}_{carbide}$) orientation relationship with the gamma/gamma prime matrix, respectively. The factor of three difference in

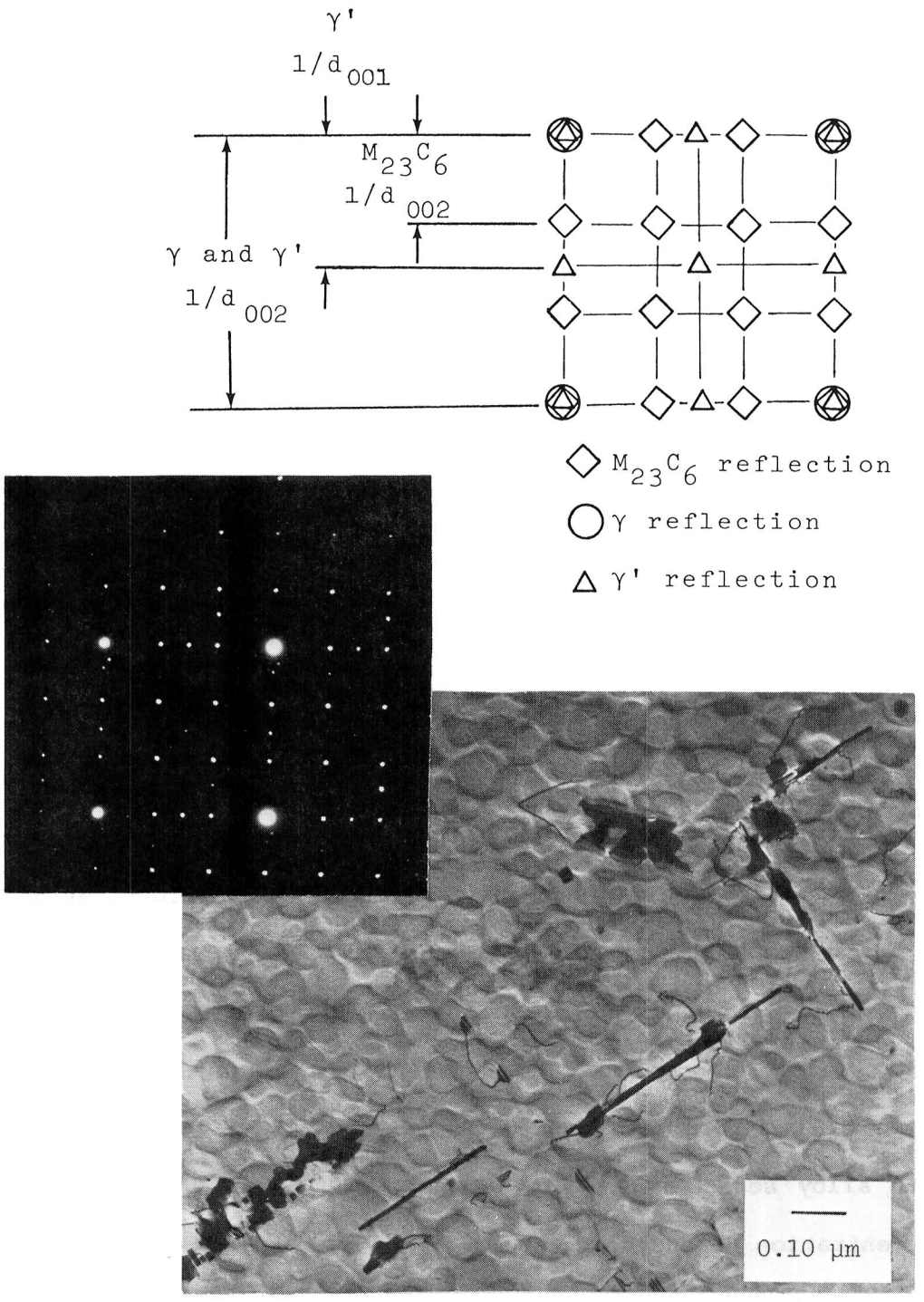

Figure 14: TEM bright field micrograph of acicular and blocky $M_{23}C_6$ carbides with [100] electron diffraction pattern and schematic insets showing the cube-on-cube orientation relationship with the gamma/gamma prime matrix.

lattice parameter between the carbides and matrix phases is also evident in the diffraction pattern. This orientation relationship has been confirmed in six other zone axes in addition to the [100] zone axis shown in Figure 14. The hexagonal carbide morphology is illustrated by the dark field TEM micrograph in Figure 15. The sides of the regular hexagons lie along a ⟨022⟩ and two ⟨111⟩ directions. The strings of small, discrete precipitates observed in the zero Ta MAR-M247 alloys with optical microscopy were found to be strings of $M_{23}C_6$ carbides with TEM (see Figure 16). It should be emphasized that there are no differences in lattice parameter and orientation relationship among the three morphologies and two types (isolated particles and strings) of $M_{23}C_6$ carbides. Differences in composition between the various morphologies and types are possible; however, a detailed STEM microanalysis study would be necessary to determine this.

4. Phase Fractions

Phase extraction was utilized to determine the weight fractions of gamma prime and the minor phases, primarily MC carbides, as a function of Ta content. It is evident from Figures 17 and 18 that Ta additions to B-1900 + Hf and MAR-M247 increase the weight fractions of gamma prime and minor phases. In addition, the weight fractions of gamma prime or carbides are approximately linear with Ta concentration and both alloy series can be described using the same line. The best fit concentration dependencies are:

gamma prime weight fraction = 56.6 + 6.51 X (a/o Ta)

regression coefficient = 0.91

minor phase weight fraction = 1.3 + 0.55 X (a/o Ta)

regression coefficient = 0.73

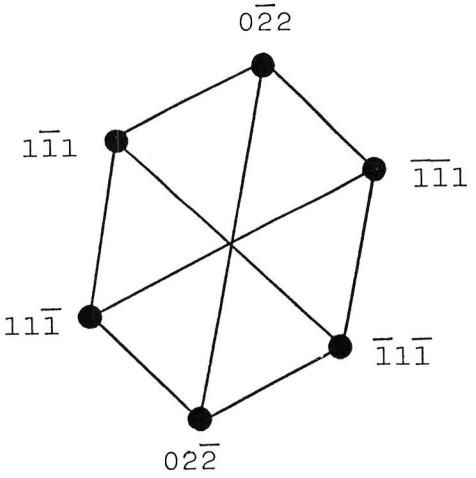

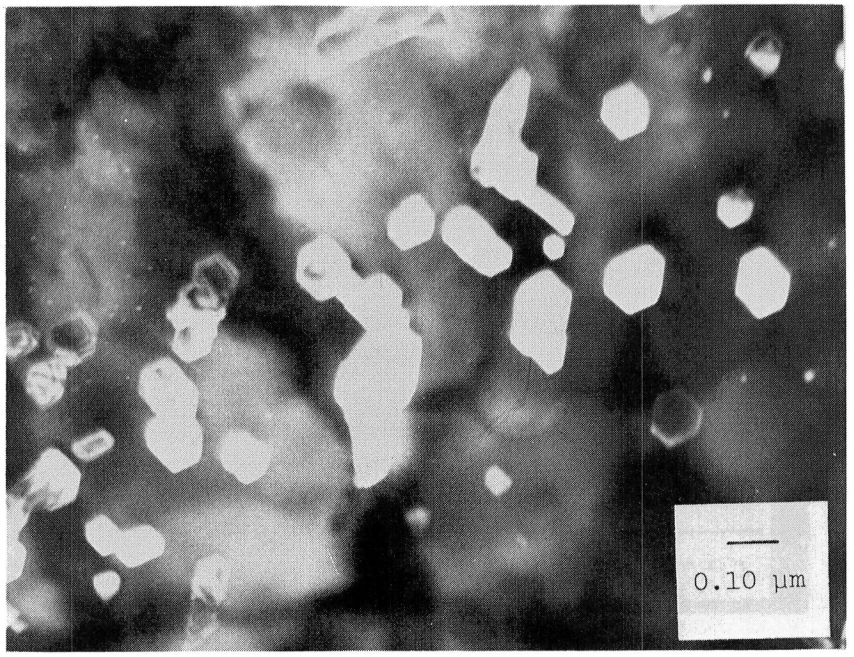

Figure 15: TEM dark field micrograph using a carbide reflection showing the hexagonal $M_{23}C_6$ carbides. The schematic diffraction pattern shows the apparent orientation relationship of the sides of the hexagons with the matrix.

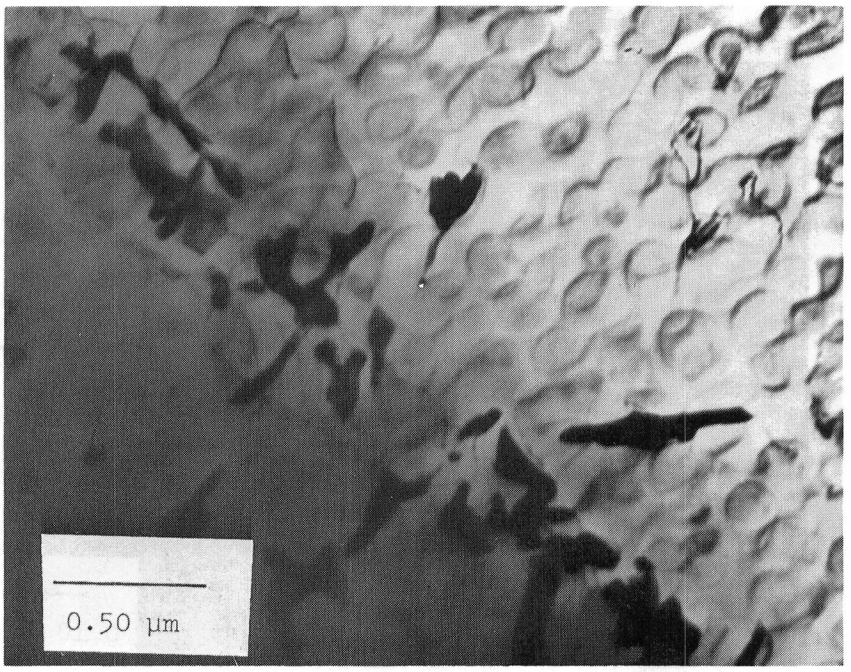

Figure 16: TEM bright field micrograph of the $M_{23}C_6$ carbides arranged as strings of discrete particles in the zero Ta MAR-M247-type alloys.

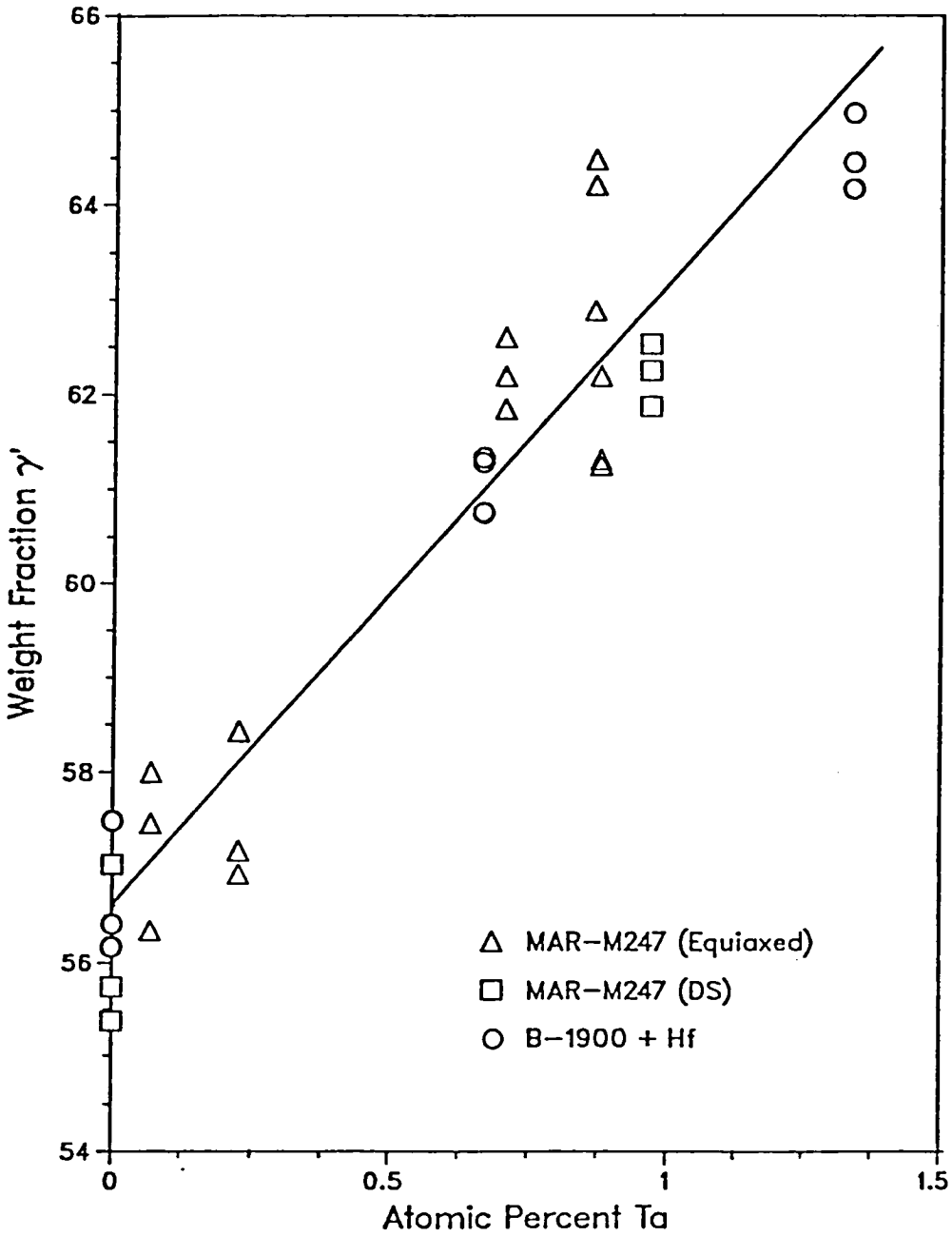

Figure 17: Gamma prime weight fraction in the heat treated MAR-M247 and B-1900 + Hf -type alloys as a function of Ta content.

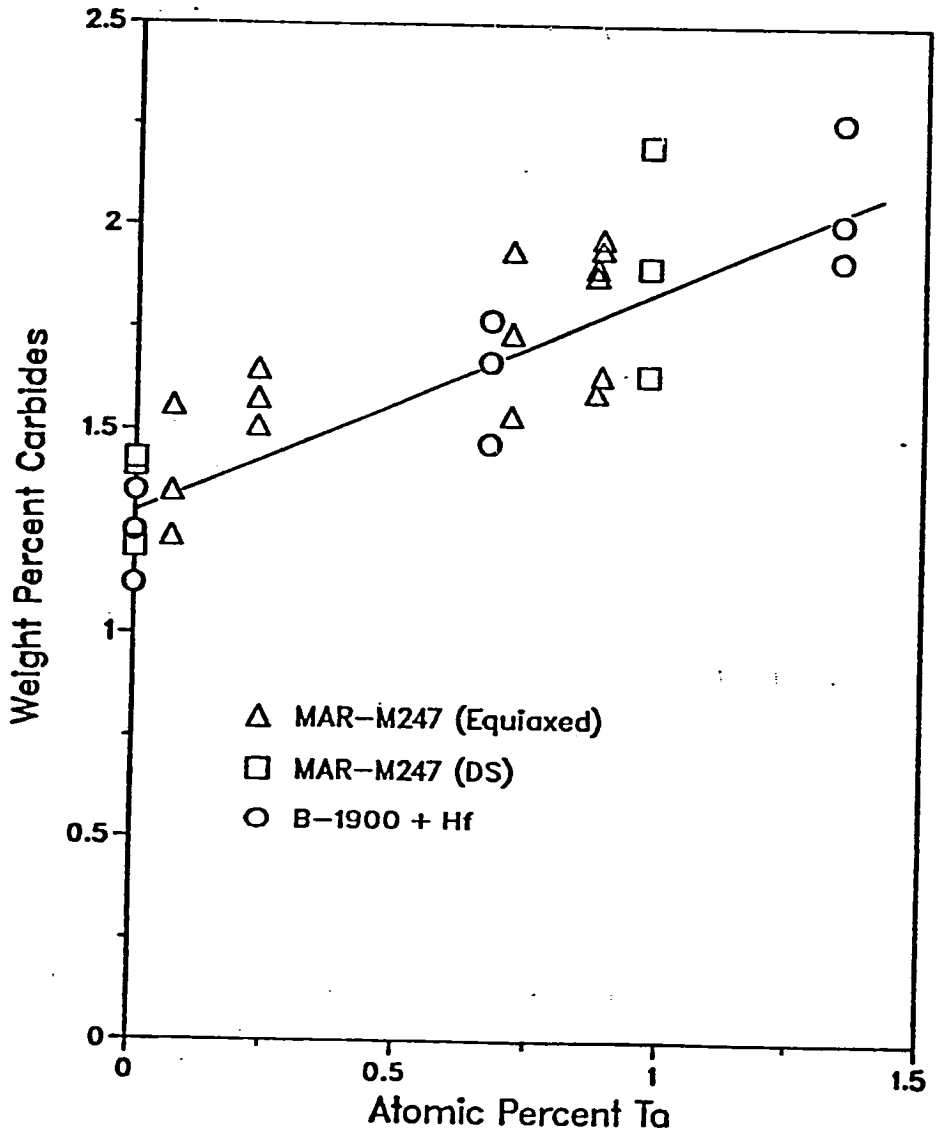

Figure 18: Minor phase weight fraction in the heat treated MAR-M247 and B-1900 + Hf-type alloys as a function of Ta content.

5. Gamma and Gamma Prime Phase Compositions

The composition of the extracted gamma prime residue from the heat treated alloys was determined by the inductively coupled plasma, atomic-emission-spectroscopy technique at NASA's Lewis Research Center and was corrected for the presence of the carbides. The gamma phase composition was calculated with the gamma prime weight fraction and composition in addition to the alloy composition. The absolute levels of the various elements, particularly those present in low concentrations, should be viewed with some caution. However, the techniques utilized are sufficient to indicate compositional trends as a function of Ta level, which are of greater interest to the present study than absolute concentrations.

The gamma prime phase compositions for the MAR-M247-type alloys are contained in Figure 19a. As the Ta level in the alloy is increased, the Ta level in the gamma prime increased. The concentrations of most other elements, namely Co, Ni, Al, W, Ti, Mo, and Hf, are nearly constant as the bulk Ta level is increased, although the W levels differ for the DS and conventionally cast alloy series. The Cr level does decrease slightly with Ta additions. The gamma phase compositions for the MAR-M247-type alloys are shown in Figure 19b. The concentrations of Cr, Co, Al, and Ta all increase sharply as Ta is added to the alloy; the levels of Mo and W are nearly constant. However, the W results again differ for the DS and conventionally cast alloys. The nickel level decreases sharply with increasing Ta additions. Ti was not present in the gamma phase; Hf values are not reported for the gamma phase because the calculations indicated negative Hf concentrations. Further work is being planned to correct this obvious error by perform-

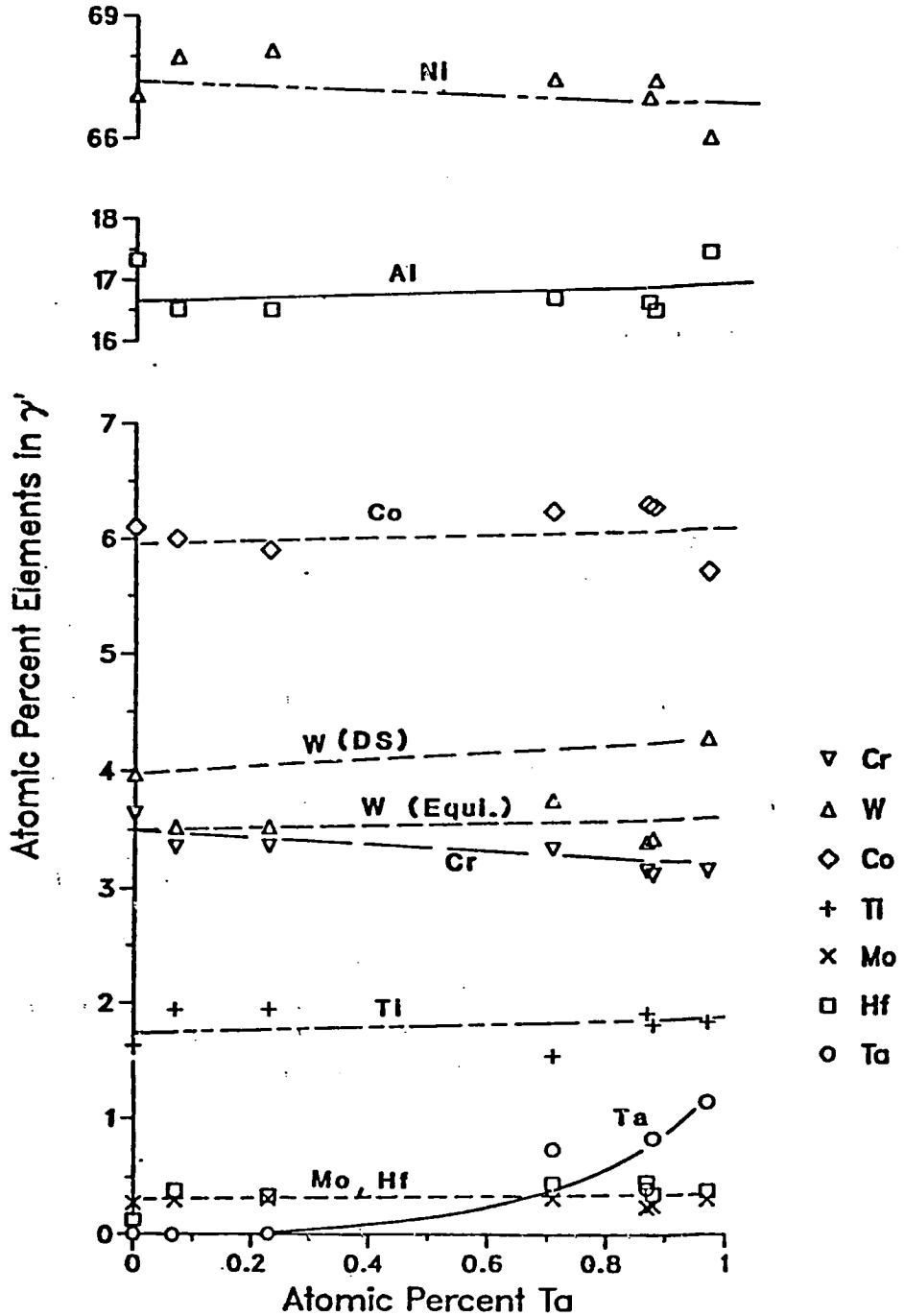

Figure 19a: Gamma prime phase composition of the heat treated MAR-M247-type alloys as a function of Ta content.

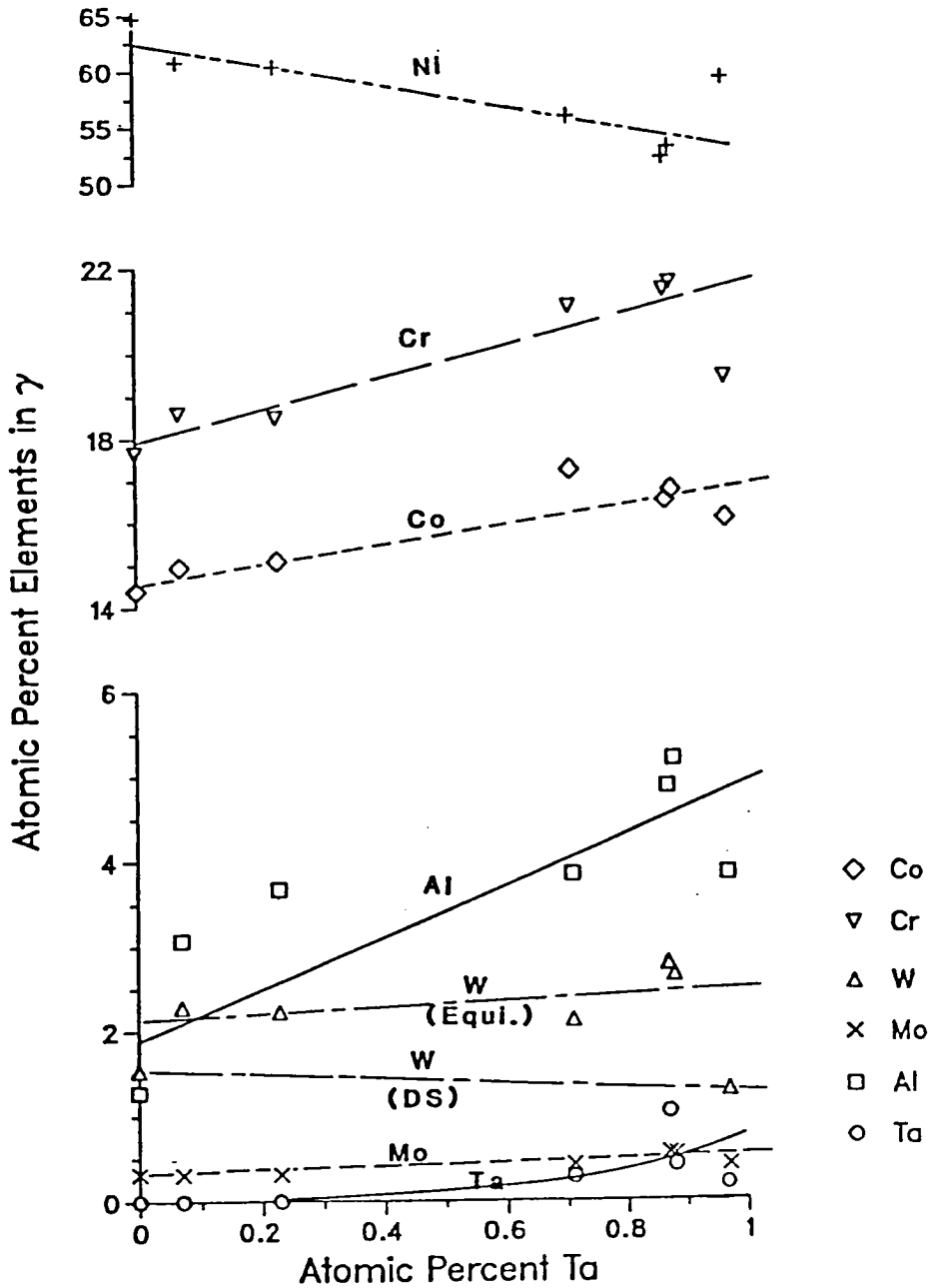

Figure 19b: Gamma phase composition of the heat treated MAR-M247-type alloys as a function of Ta content.

ing STEM microanalysis on the individual gamma and gamma prime phases.

An alternate method of examining gamma and gamma prime compositions as a function of Ta content is with partitioning ratios, defined as the percentage of an element in the gamma prime phase divided by the percentage of the same element in the gamma phase. A partitioning ratio of less than unity indicates that an element is contained primarily in the gamma phase, and a partitioning ratio greater than one indicates that element is primarily in the gamma prime phase. The partitioning ratios for the MAR-M247-type alloys in Figure 19c show that the partitioning ratios of Ni, Co, and Cr are independent of Ta level. The partitioning ratios of Al and Mo decrease somewhat with Ta additions. Although the partitioning ratio for Ti is not shown, it is greater than 20 for all the MAR-M247-type alloys. The partitioning ratio of W reflects the difference in the gamma and gamma prime phase W levels for the conventionally cast and DS alloys. Partitioning data is not reported for Hf and Ta because of the scatter in the data.

The gamma prime compositions for the B-1900 + Hf-type alloys, contained in Figure 20a, show slightly different results than the MAR-M247-type alloys. Specifically, the Co and Ti levels remain constant with Ta variations, and the Mo and Cr concentrations decrease with increasing bulk Ta content. The Ta level increases sharply, as well as the Hf and Al levels to a lesser degree, as Ta is added to the alloy. The gamma phase results, shown in Figure 20b, indicate that as Ta is added to B-1900 + Hf, the Cr, Co, Mo, and Ta levels all increase. The Hf and Al levels are constant with Ta variations, and both Ni and Ti levels decrease slightly with increasing bulk Ta levels. The partitioning ratios for the B-1900 + Hf-type alloys in Figure 20c are

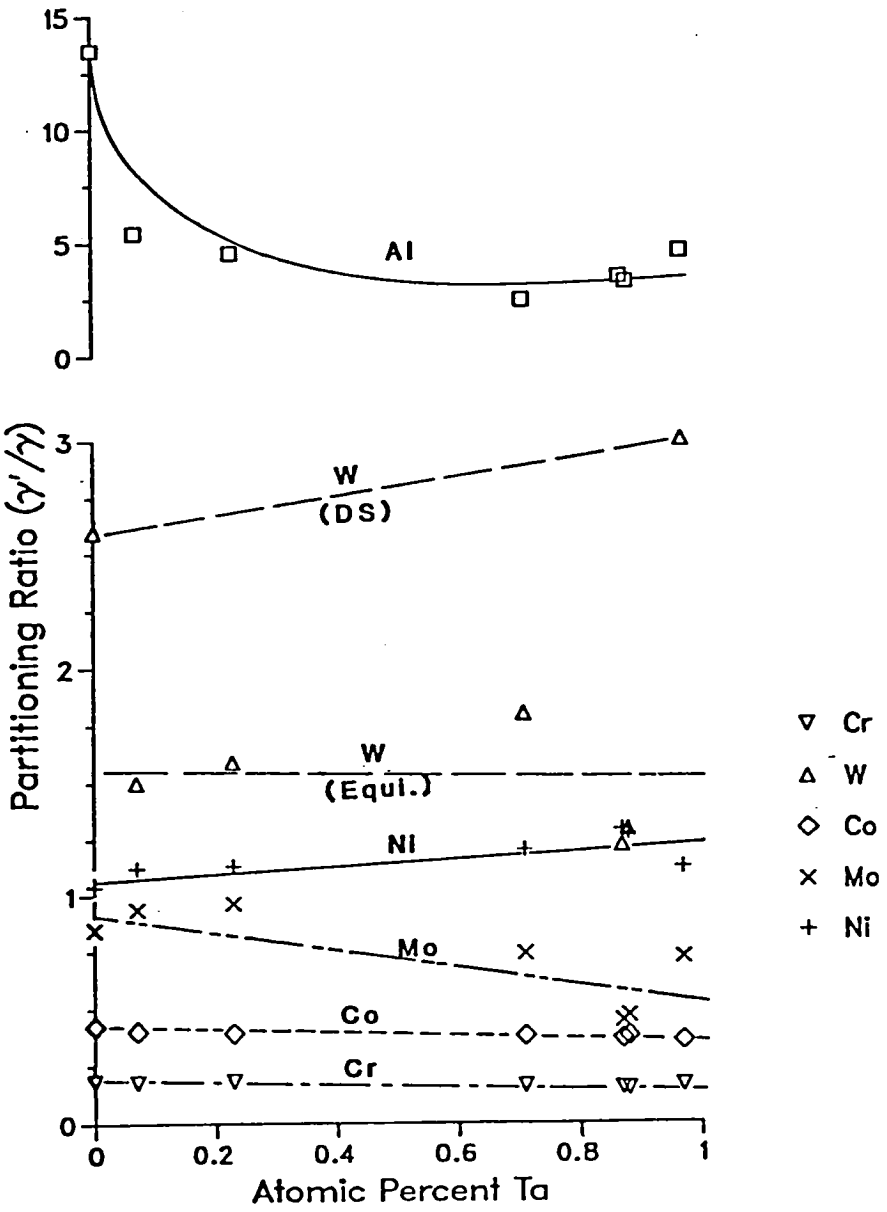

Figure 19c: Gamma prime/gamma phase elemental partitioning ratios for the heat treated MAR-M247-type alloys.

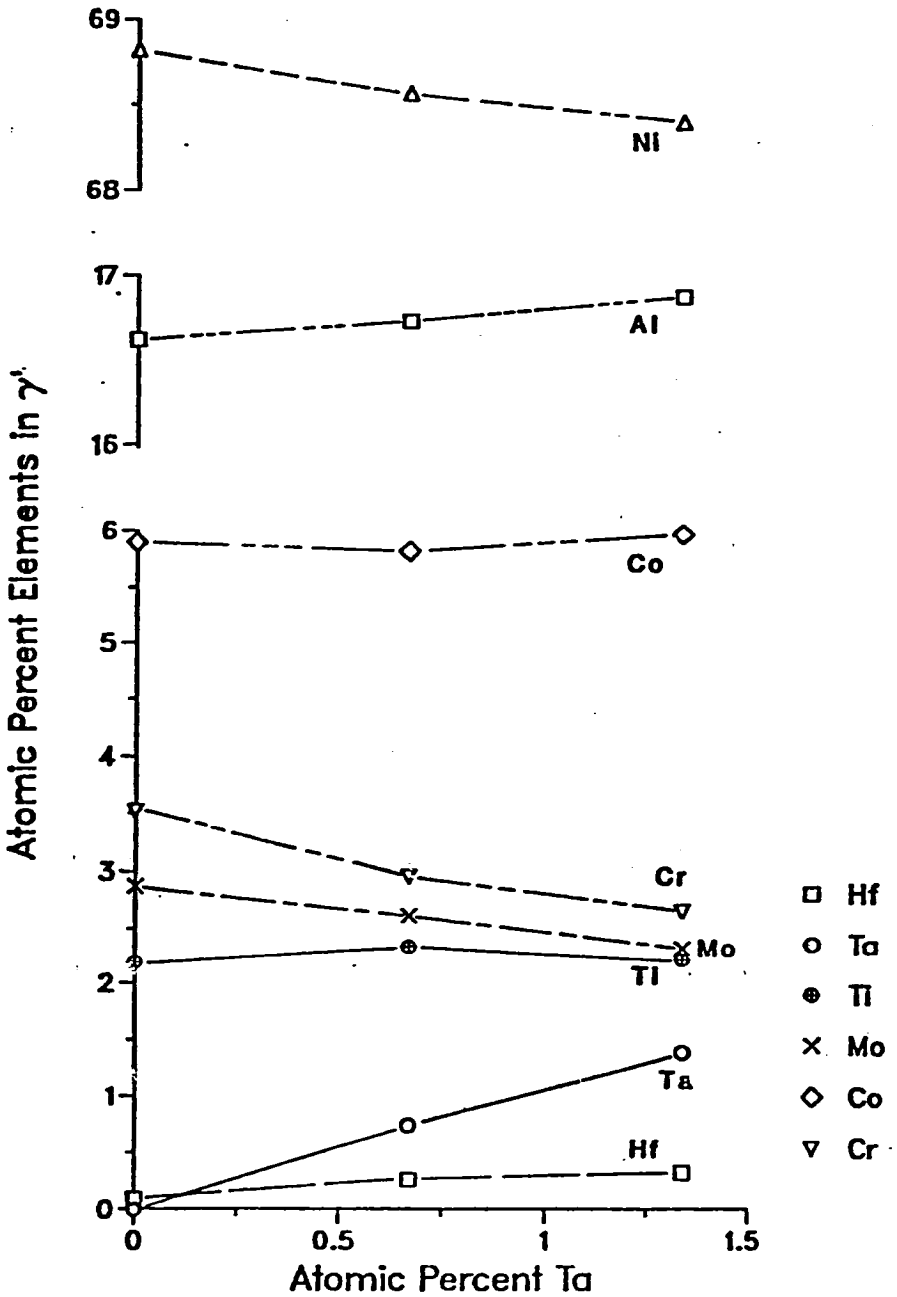

Figure 20a: Gamma prime phase composition for the heat treated B-1900 + Hf-type alloys as a function of Ta content.

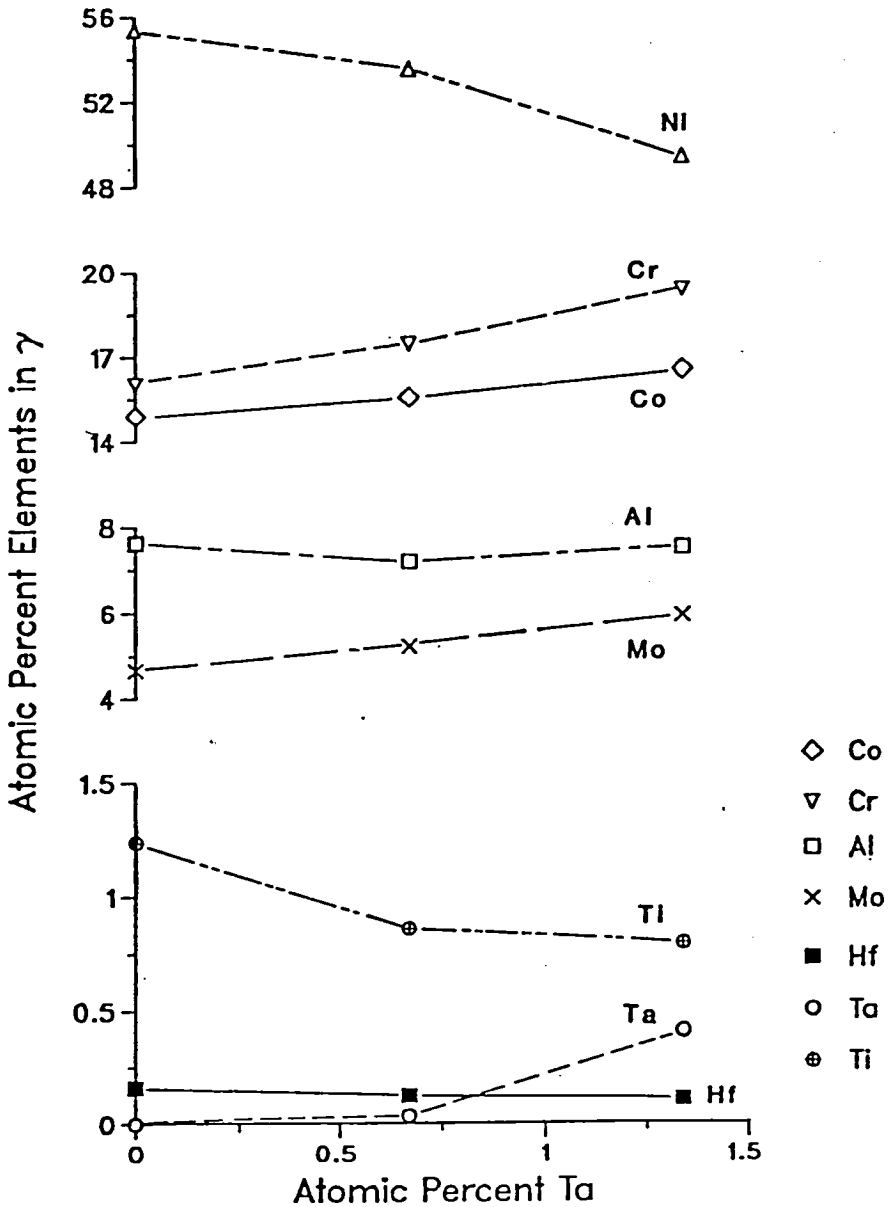

Figure 20b: Gamma phase composition of the heat treated B-1900 + Hf-type alloys as a function of Ta content.

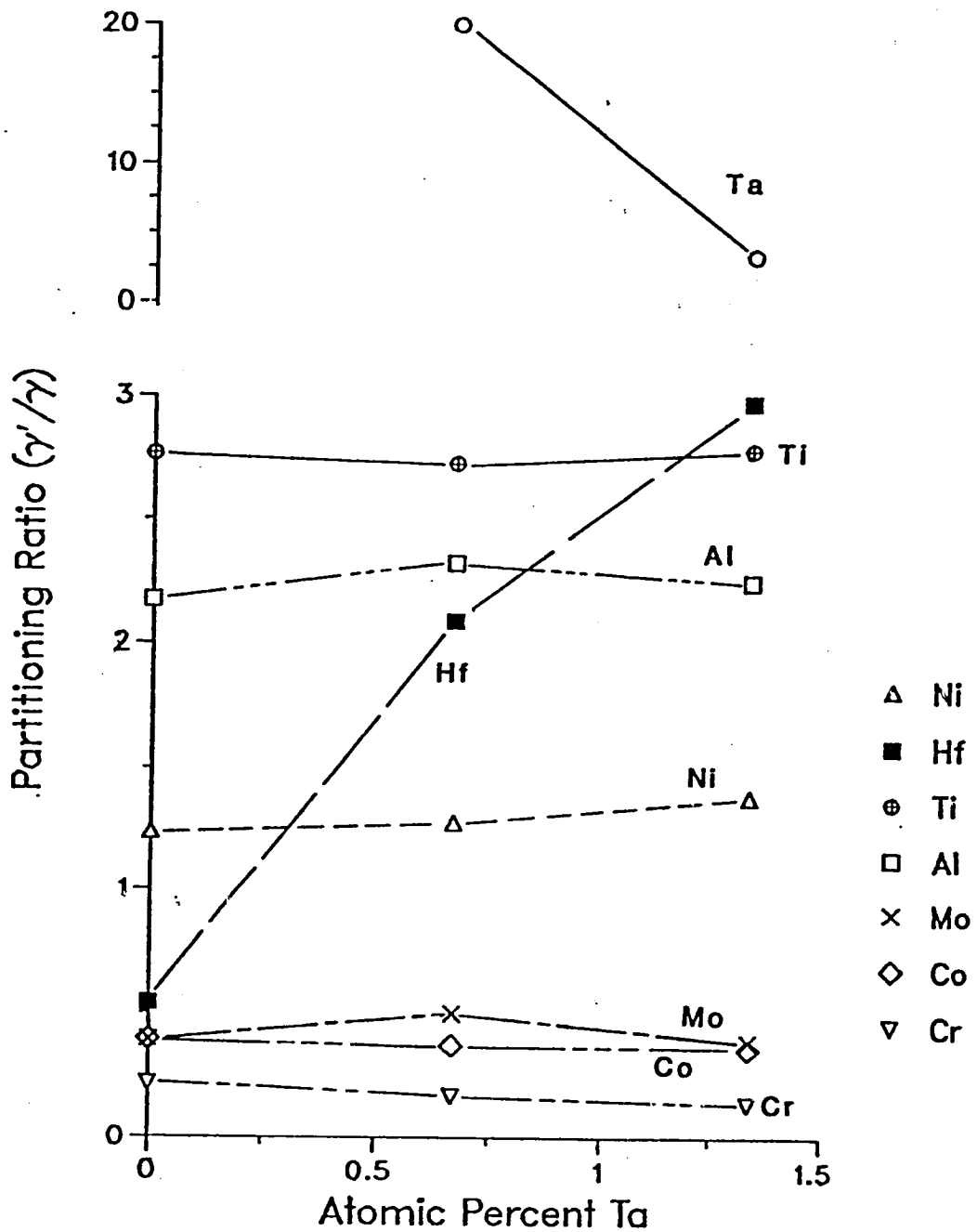

Figure 20c: Gamma prime/gamma phase elemental partitioning ratios for the B-1900 + Hf-type alloys as a function of Ta content.

similar to those for the MAR-M247-type alloys. The partitioning ratios of Co, Cr, and Ni are constant with Ta variations, consistent with the MAR-M247 results. In addition, the partitioning ratios for Al, Mo, and Ti are also independent of Ta content. However, the Hf and Ta partitioning ratios are very sensitive to increasing bulk Ta additions; the partitioning ratios of Hf and Ta increase and decrease, respectively, with Ta additions. The change in the Hf distribution is likely a consequence of more Hf becoming available to the matrix phases as a result of Ta replacing part of the Hf contained in the MC carbides.

B. Mechanical Properties

1. Tensile Properties

Tensile tests were performed at 540°C (1000°F), 760°C (1400°F), and 982°C (1800°F) on the conventionally cast and DS MAR-M247-type alloys. The results are presented in Table 6. The yield strength at 540°C is increased by the addition of Ta, with the DS and conventionally cast alloys showing comparable properties at equivalent Ta levels. The UTS is apparently unaffected by Ta variations. At 760°C and 982°C, both yield strength and UTS are increased by Ta additions to the DS alloys. Successful tensile tests were not performed on the conventionally cast alloys at the higher temperatures. The tensile ductility is greater for the DS alloys than the conventionally cast alloys at 540°C and is decreased slightly by Ta additions. Figure 21 illustrates the temperature dependency and the Ta effects on the average tensile properties of DS MAR-M247. An increase of about 150 MPa occurs in both yield strength and UTS between 540°C and 760°C; both properties decrease by about 500 MPa when the temperature is increased to 982°C. The

Table 6: Tensile Properties of MAR-M247 Type Alloys

Alloy	Temperature (°C)	0.2% Yield Strength (MPa)	UTS (MPa)	Ductility % Elong.	Ductility % RA
A1	540	909	1018	6.5	8.2
	982	--*	434	---	---
B1	540	949	998	3.0	4.3
	982	--**	246	---	---
C	540	874	1062	10.3	11.6
	540	911	1087	8.1	10.8
	760	981	1131	3.4	3.8
	982	418	492	23.1	29.7
	982	334	454	27.2	38.3
	982	432	504	29.1	31.1
D	540	992	1090	6.1	10.3
	540	923	1062	9.0	10.9
	760	1075	1265	3.6	4.4
	982	429	597	23.6	29.3
	982	418	563	20.7	33.3
	982	450	564	4.9	6.7

* Failed before yielding
** Failed in fillet

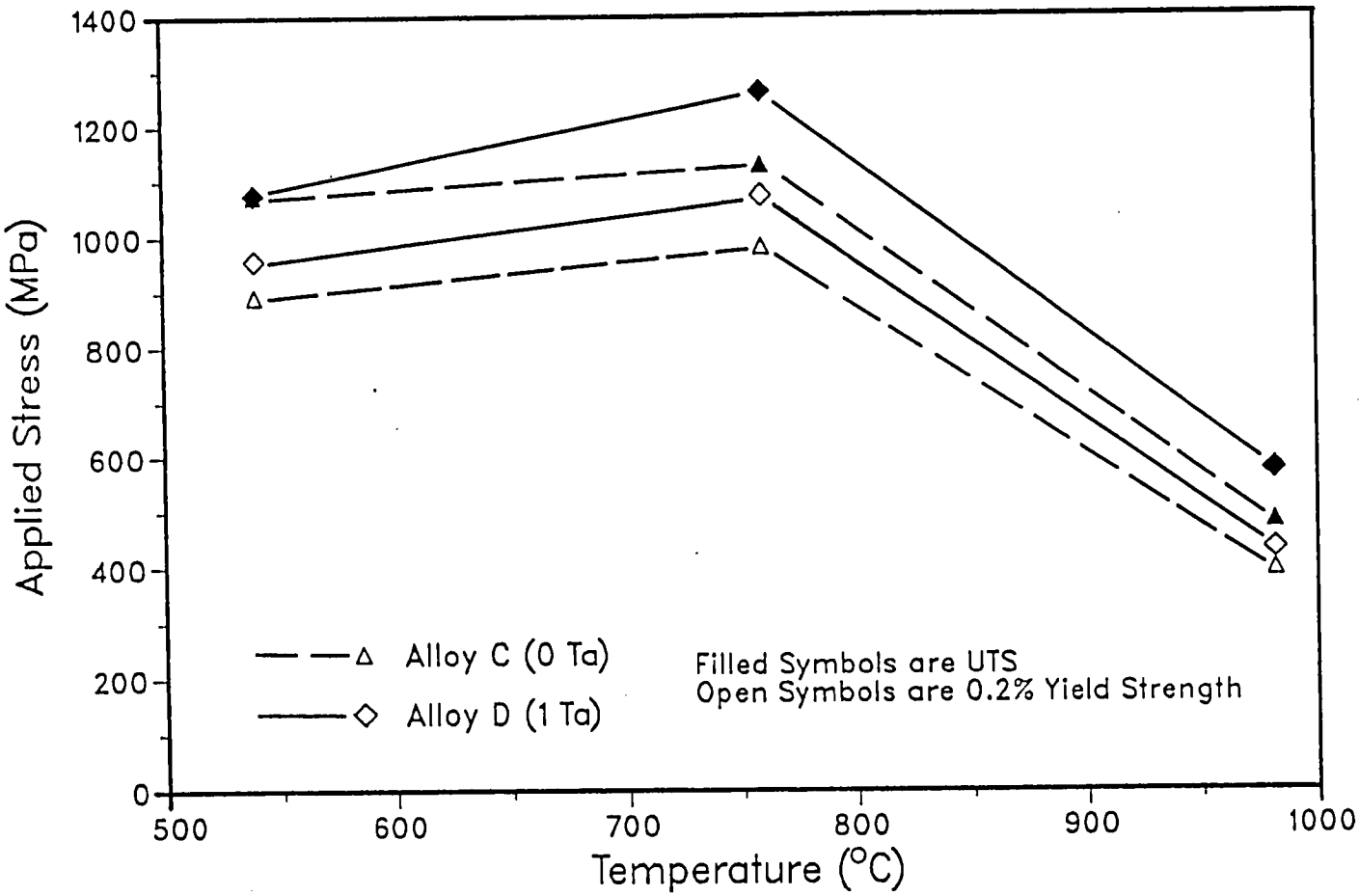

Figure 21: Yield stress and ultimate tensile strength for the DS MAR-M247-type alloys as a function of test temperature.

temperature effects were equivalent for both alloys, although the strengths of the Ta containing alloy were higher. The temperature dependencies observed in this study are typical of nickel-base superalloys with a high gamma prime fraction.

2. Creep Rupture Properties

Creep rupture tests were performed at 760°C (1400°F), 871°C (1600°F), and 982°C (1800°F) on the conventionally cast and DS MAR-M247-type alloys. Stress levels were selected to maximize the range of secondary creep rates and rupture times at each temperature. The results of the creep rupture testing are presented in Table 7. Ta additions improve the creep rupture resistance by increasing the rupture life and decreasing the secondary creep rate of the DS alloys at all temperatures tested. This can be seen by comparing the creep curves of the two alloys at the same stress level in Figure 22, with one example for each test temperature. An insufficient number of tests were carried out to examine rupture ductility as a function of Ta level.

The creep rupture property of greatest importance to the component designer is secondary (or minimum) creep rate. This parameter is typically plotted on a logarithmic scale as a function of applied stress; the slope of this plot is the stress exponent n in the power law expression for creep rate (equation 1 of the introduction). The secondary creep rates for the DS MAR-M247-type alloys are plotted in such a manner in Figure 23. The Ta-containing alloy always requires a higher stress at a given minimum creep rate and temperature than the zero Ta alloy, indicating again that Ta additions improve the creep resistance of DS MAR-M247. With the limited data, the stress exponents

Table 7: Creep Rupture Properties of MAR-M247 Type Alloys

Alloy	Temperature (°C)	Stress (MPa)	Rupture Time (Hours)	$\dot{\varepsilon}_s$ (10^{-8}) (sec^{-1})	Ductility % Elong.	Ductility % RA
A1	760	414	4.1*	---***	---	---
	982	138	200.0**	1.15	---	---
B1	760	690	0.1	---***	2.2	2.0
	982	172	1.8	---***	1.5	1.2
C	760	483	200.0**	---***	---	---
	760	690	37.5	20.6	7.4	12.7
	760	862	3.5	366	7.0	7.0
	871	345	198.5	8.61	49.7	41.1
	871	414	15.0	39.7	3.3	4.9
	982	138	200.0**	3.13	---	---
	982	172	91.4	17.2	36.8	60.5
	982	241	9.4	145	37.2	50.2
	982	276	3.1	---***	33.7	44.9
D	760	690	100.0**	3.09	---	---
	760	862	16.2	90.0	14.5	14.7
	760	1103	2.2	---***	9.4	12.2
	871	414	100.0**	5.19	---	---
	871	483	54.1	28.3	29.8	37.2
	982	172	200.0**	3.42	---	---
	982	207	89.8	10.7	30.9	55.6
	982	241	38.6	32.5	33.7	53.7
	982	276	16.3	106	27.9	34.1

* Failed in fillet
** Test terminated in time indicated, did not fail
*** Secondary creep rate not determined

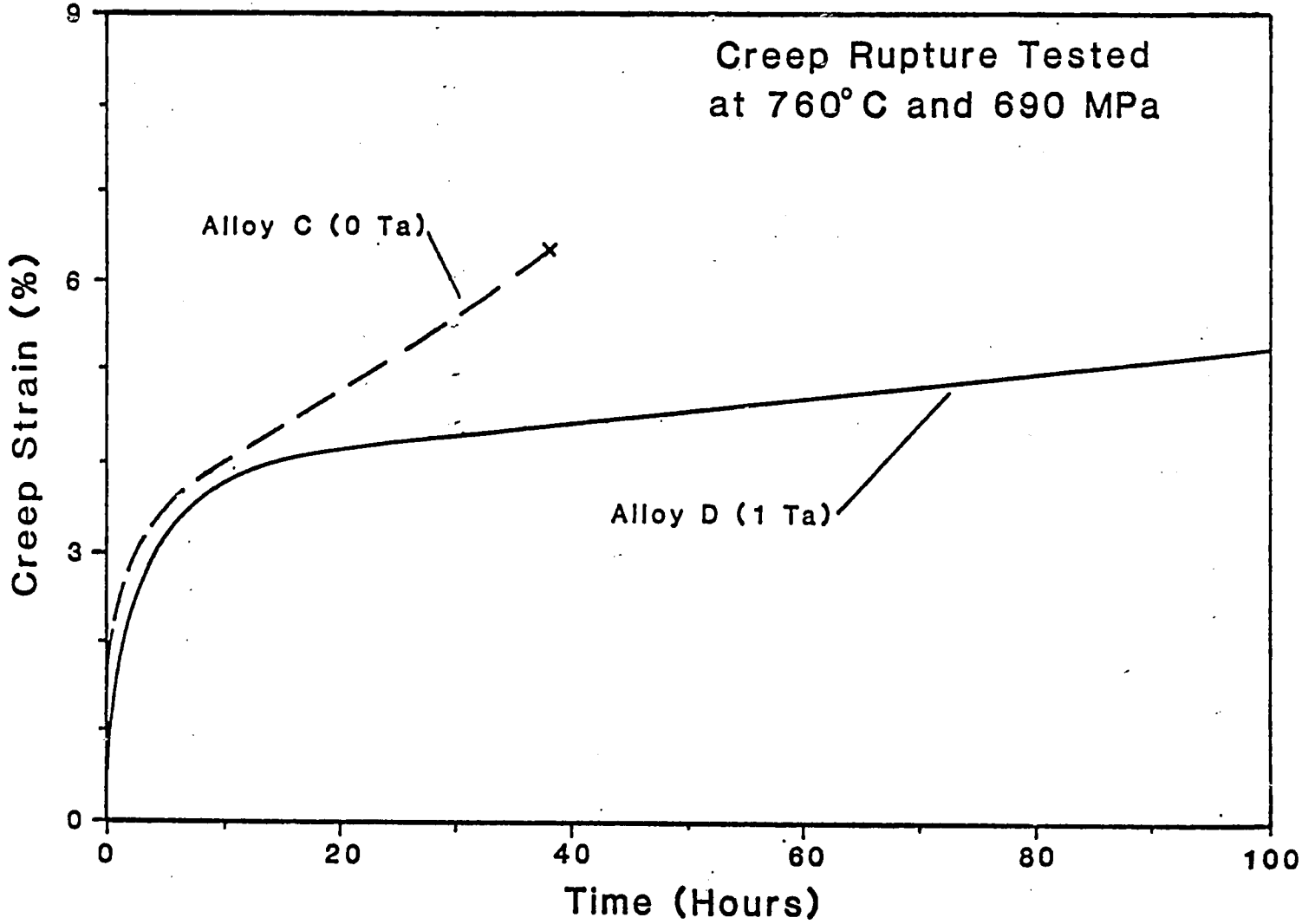

Figure 22a: Creep curves for DS MAR-M247-type alloys tested at 760°C and 690 MPa.

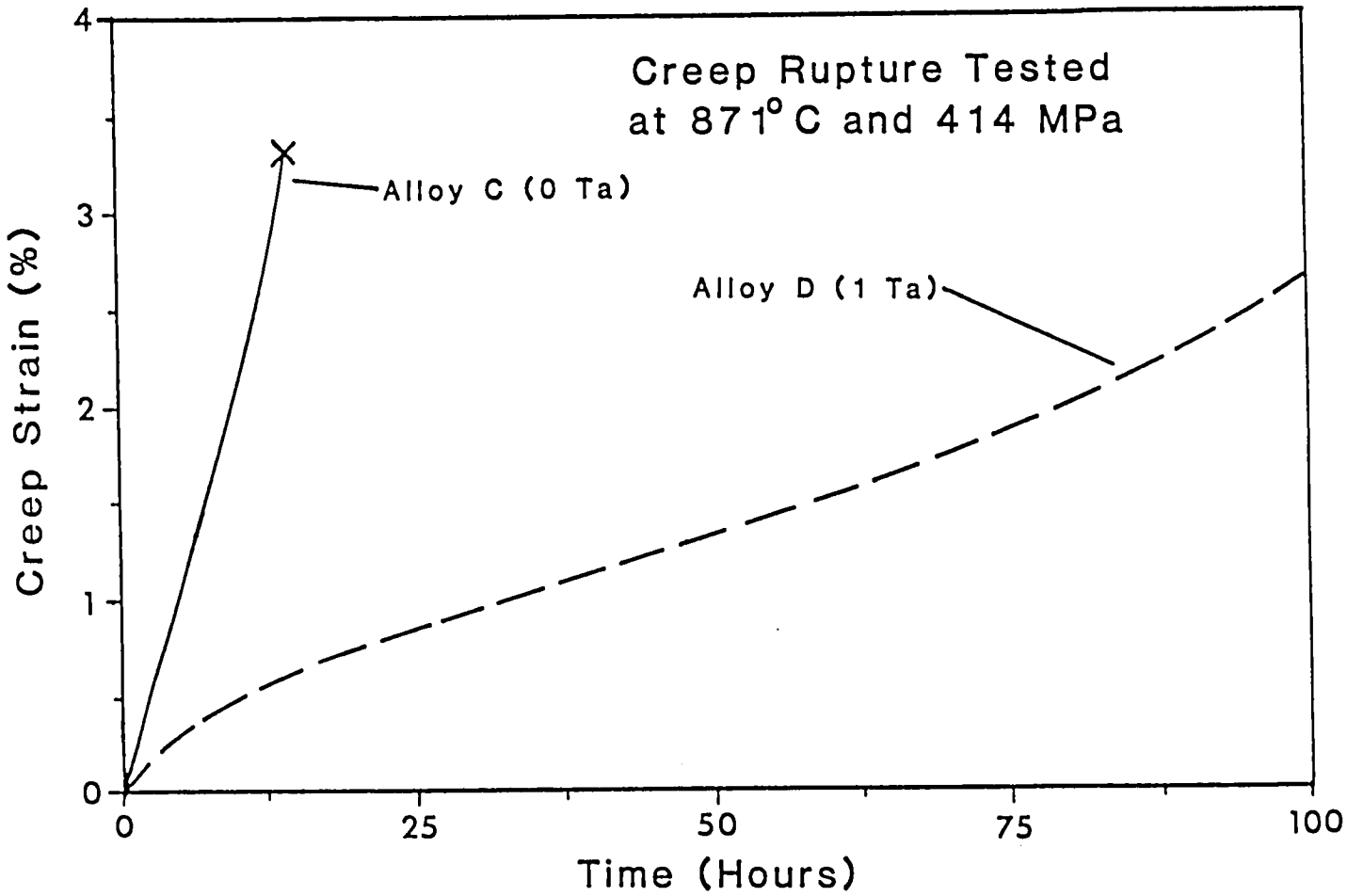

Figure 22b: Creep curves for DS MAR-M247-type alloys tested at 871°C and 414 MPa.

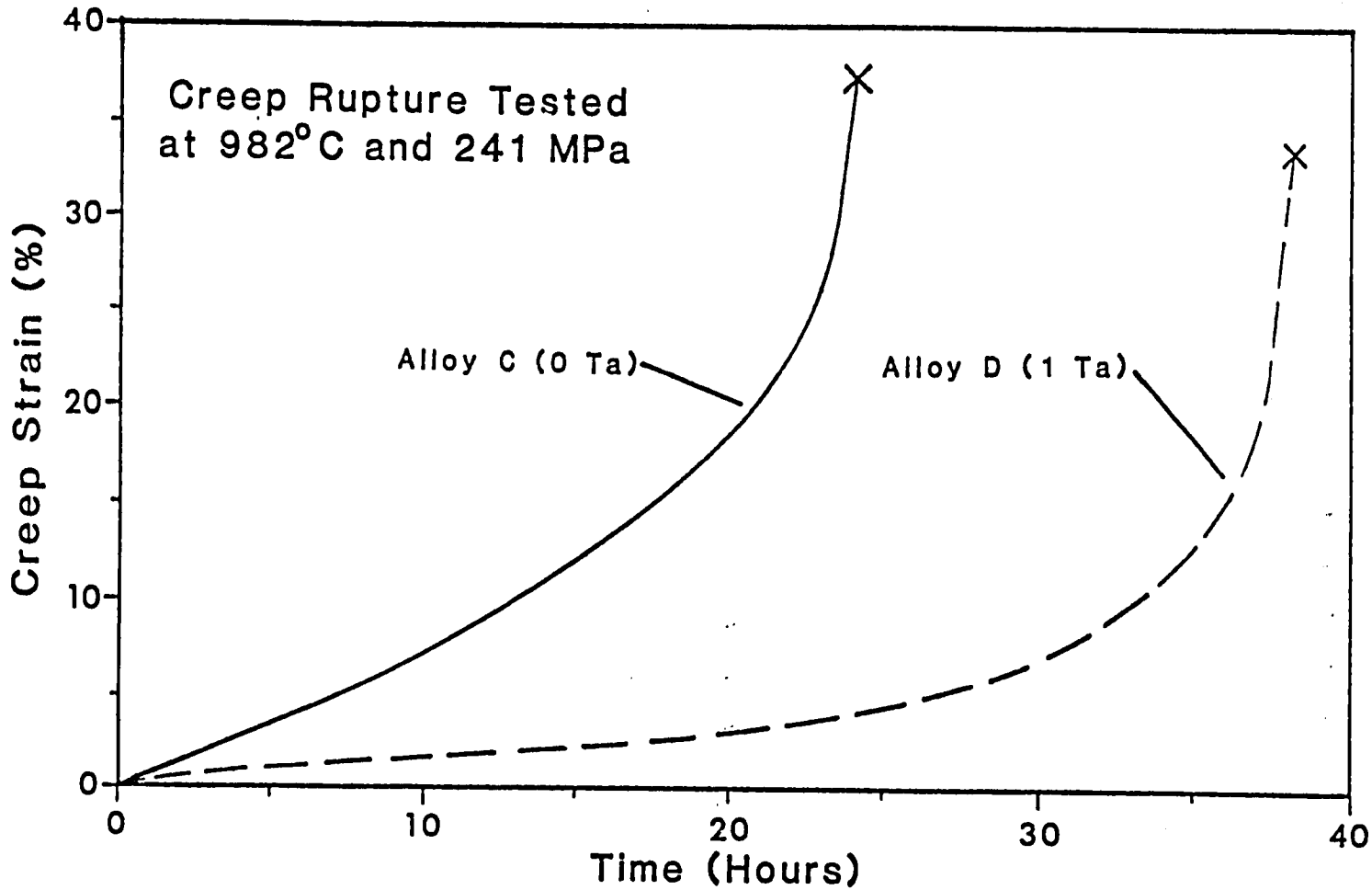

Figure 22c: Creep curves for DS MAR-M247-type alloys tested at 982°C and 241 MPa.

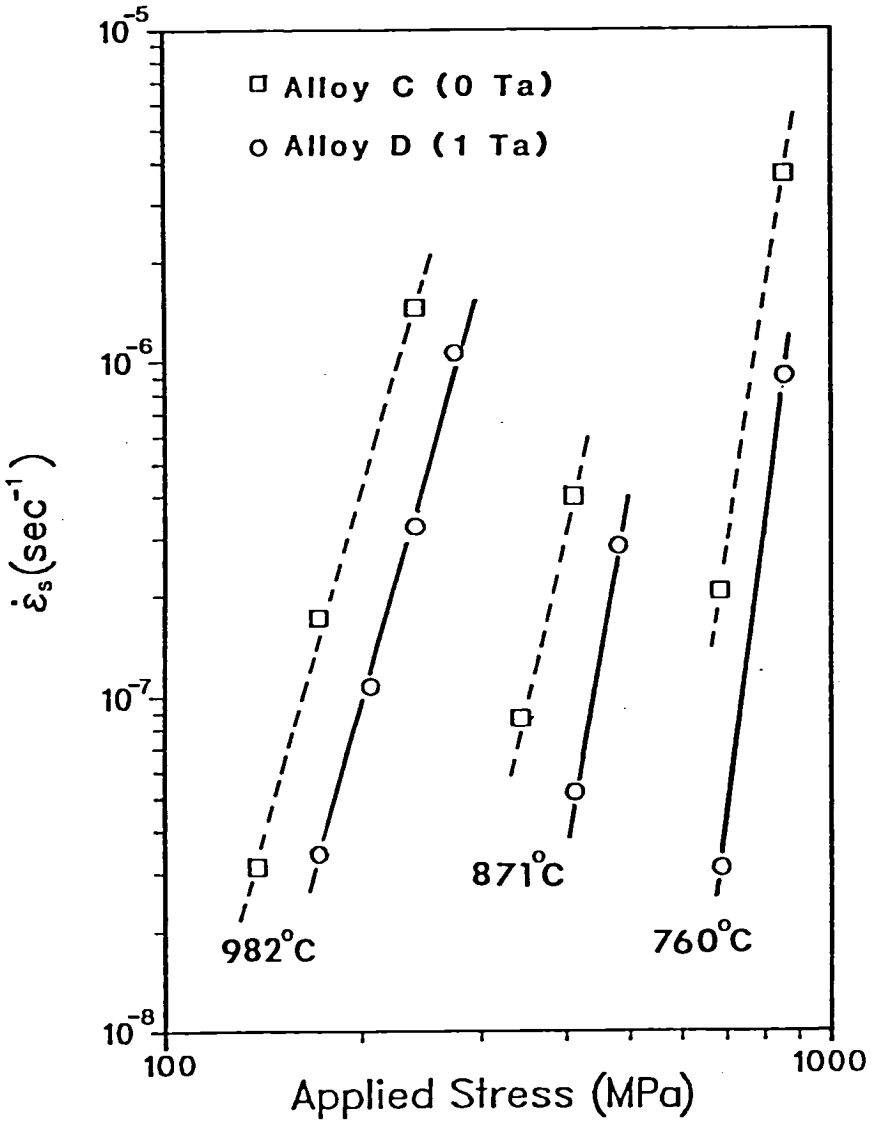

Figure 23: Logarithmic plot of secondary creep rate as a function of applied stress in the DS MAR-M247-type alloys at 760, 871, and 982°C.

were calculated to be 12.9, 8.4, and 6.9 for the zero Ta alloy and 15.1, 11.0, and 7.5 for the normal Ta alloy at 760, 871, and 982°C, respectively.

Creep rupture data can also be expressed with a Larson-Miller plot, which permits extrapolations to temperatures and stress levels that were not used in the actual experiments. The Larson-Miller parameter can either be considered in terms of secondary creep rate or rupture life, since they are inversely related. The formulae for the Larson-Miller parameters are:

$$LMP = (T + 460) \times (20 + \log(t_{rup})) \text{ for rupture life}$$

and

$$LMP = (T + 460) \times (20 - \log(\dot{\varepsilon}_s)) \text{ for secondary creep rate}$$

with units of °F and hours

Using these expressions, the creep rupture data in Table 7 were placed on Larson-Miller plots; Figure 24 is in terms of rupture time, and Figure 25 is in terms of secondary creep rate. By selecting a Larson-Miller parameter, a combination of temperature and rupture life (or secondary creep rate) is therefore determined. The position of the Larson-Miller plot for an alloy then determines the stress for that given Larson-Miller parameter. The Larson-Miller plots for Alloy D (1 Ta) always lay at a higher stress level than those for Alloy C (0 Ta), again indicating the greater creep resistance of the Ta containing alloy.

Only one of four creep-rupture tests on the conventionally cast alloys showed much ductility and creep life. The other three specimens either failed in the fillet or at very low rupture times with negligible ductility. All fractures occurred at transverse grain boundaries,

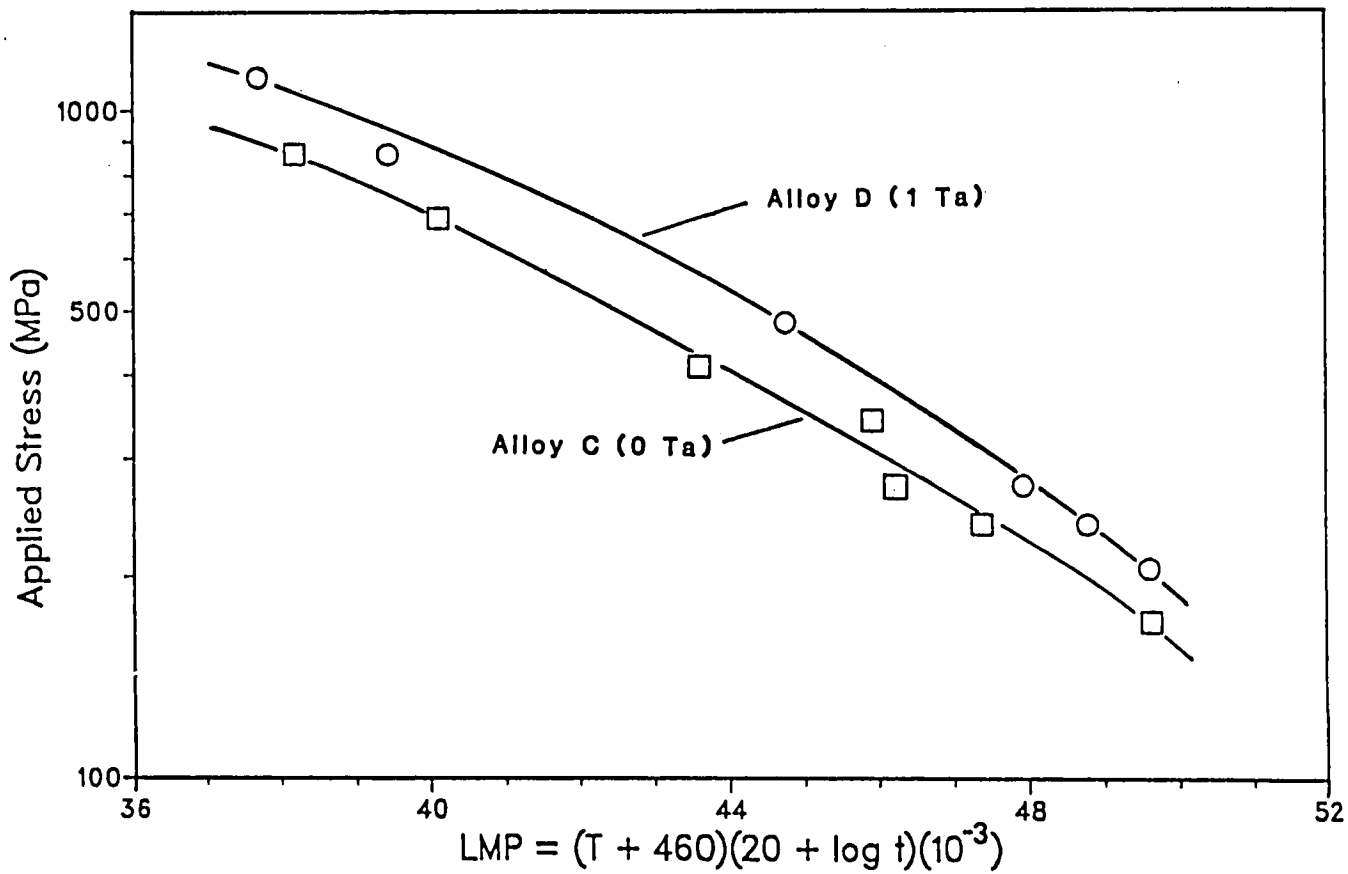

Figure 24: Larson-Miller plots in terms of rupture life for DS MAR-M247-type alloys.

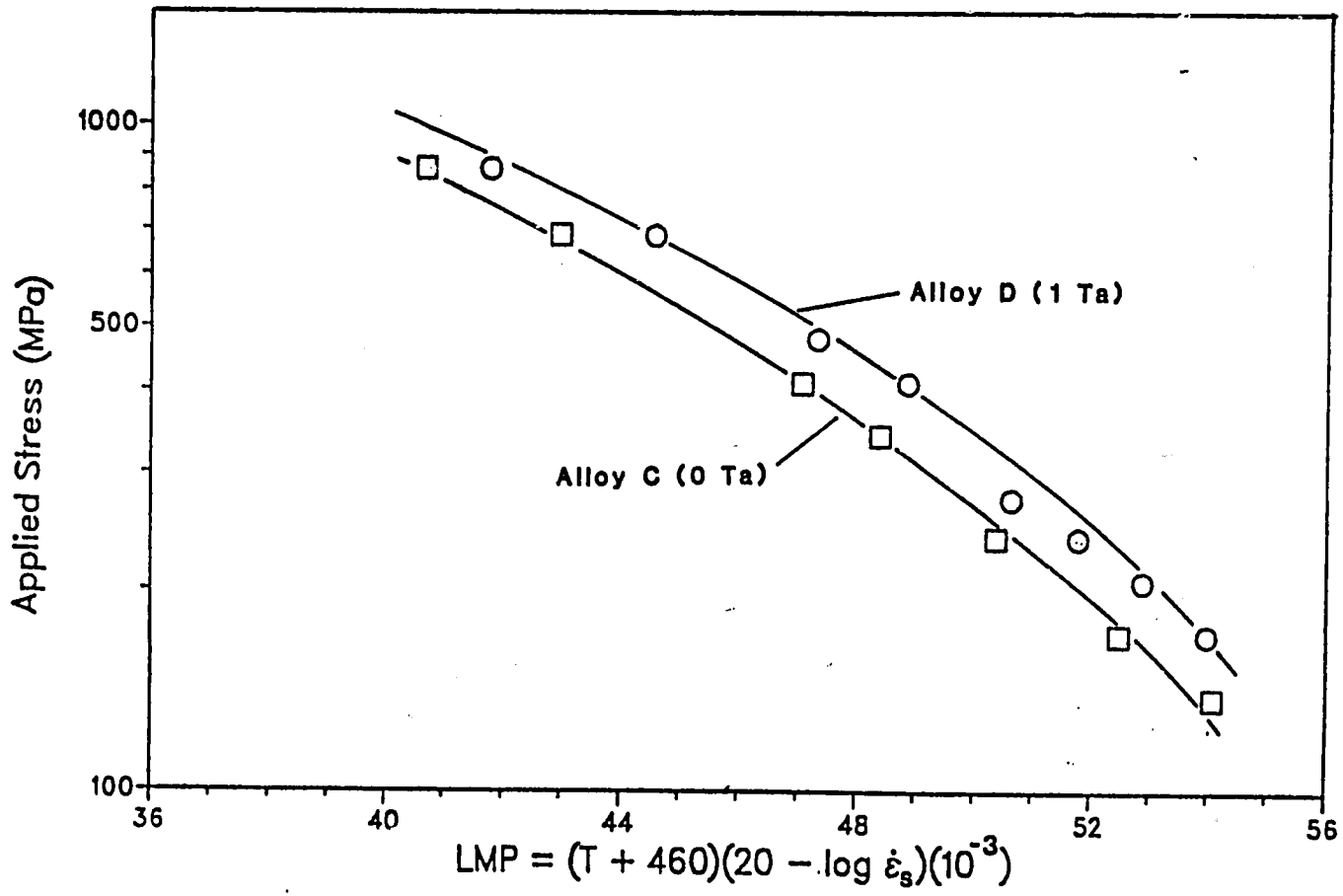

Figure 25: Larson-Miller plots in terms of secondary creep rate for DS MAR-M247-type alloys.

and, in the SEM fractograph in Figure 26, the grain structure is very evident. This fracture mode was also observed in the tensile specimens. The early failures and low ductilities are likely related to the removal of the reportedly ductile [11] gamma/gamma prime eutectic along the grain boundaries by the solution treatment. The one successful creep test of a conventionally cast alloy gave comparable behavior to its DS counterpart, as can be seen in the creep curves in Figure 27.

3. Post-Creep Tested Microstructure

The microstructure was examined after creep testing by SEM on longitudinal sections. Coarsened, cuboidal gamma prime was found in the gauge sections of the DS specimens tested at 760°C and 871°C, and the grip sections of the DS specimens tested at all temperatures. An example is shown in Figure 28a. However, a rafted gamma prime structure developed in the gauge sections of the DS alloys tested at 982°C, as is shown in Figure 28b. The gamma prime platelets are oriented perpendicular to the stress axis. This stress-coarsened gamma prime structure has also been observed after high temperature creep testing of single crystal MAR-M247 [27,41]. The gamma prime morphology of the one successful creep test on the conventionally cast material (at 760°C) was coarsened and cuboidal as were the DS specimens at the same temperature. The tensile tests brought about no change in morphology or size of the gamma prime precipitates from the solutionized and aged condition.

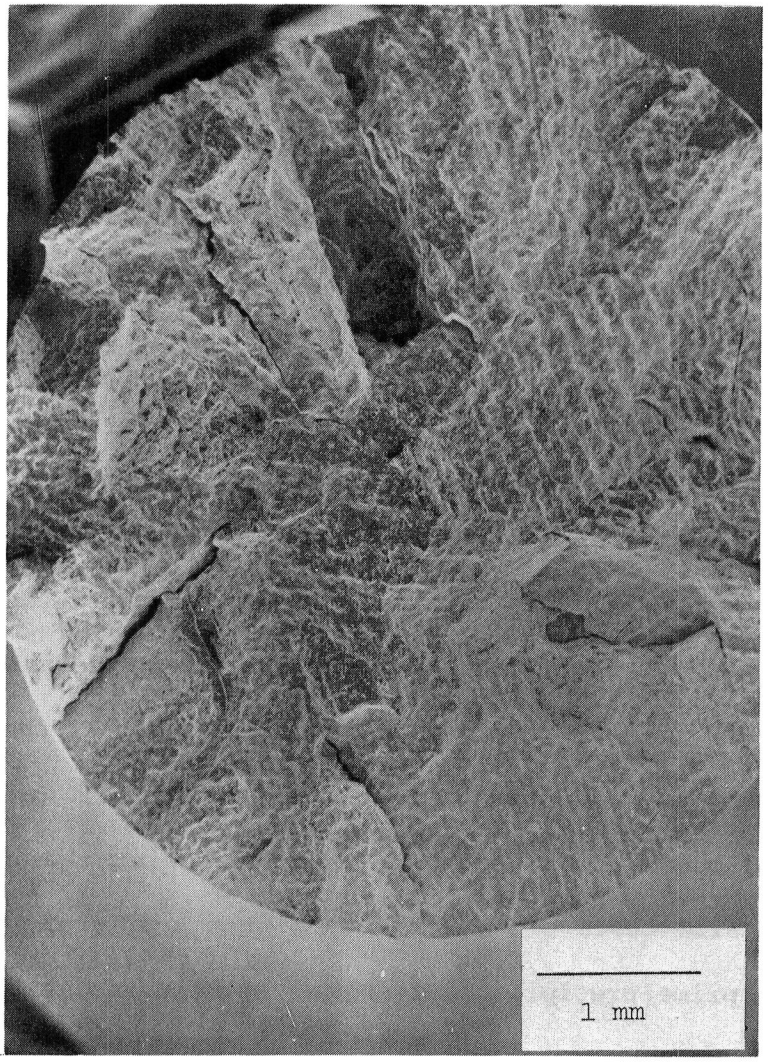

Figure 26: SEM micrograph showing the intergranular fracture surface from a 1000°C tensile test of a conventionally cast MAR-M247-type alloy.

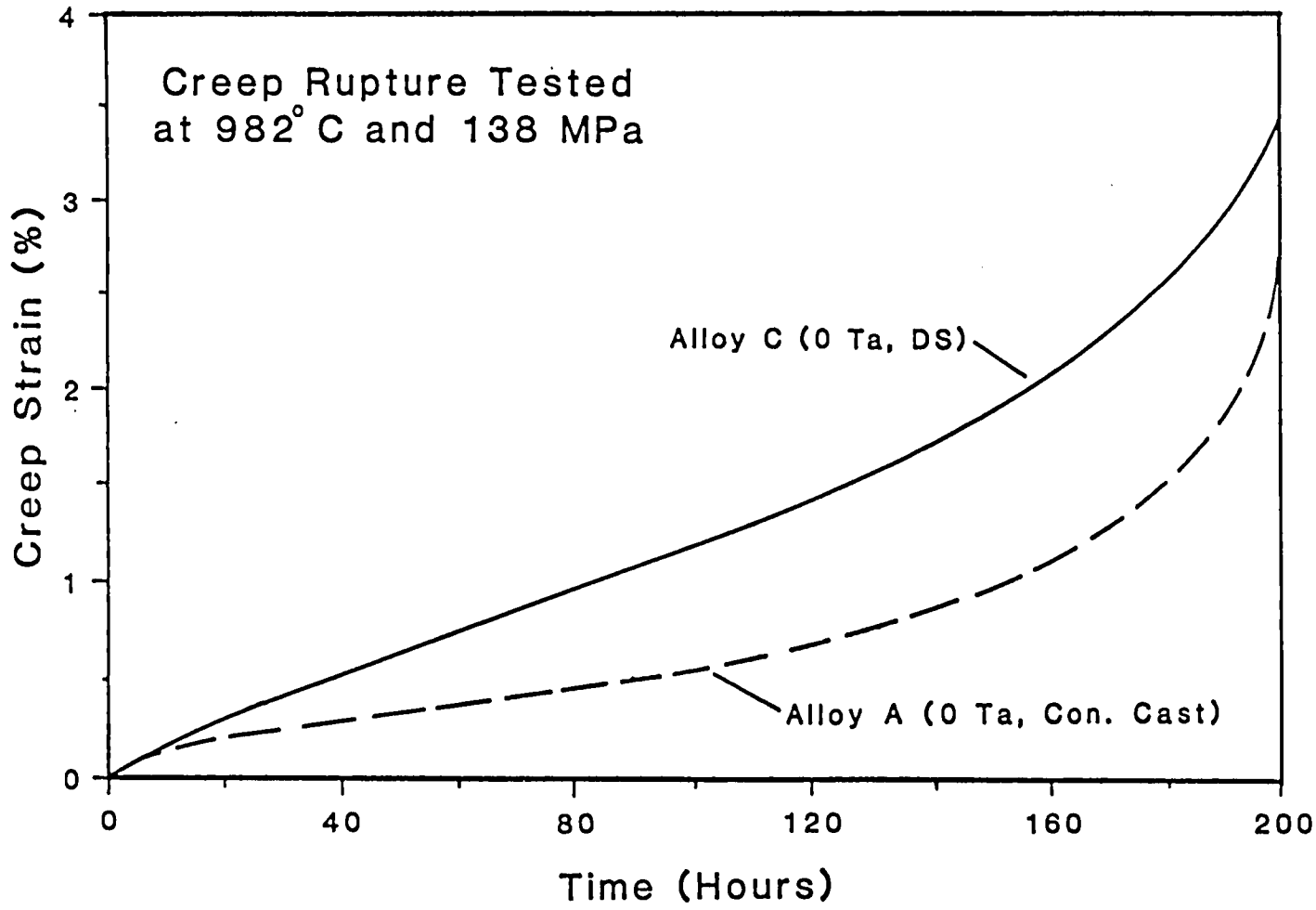

Figure 27: Creep curves for zero Ta conventionally cast and DS MAR-M247-type alloys tested at 982°C and 138 MPa.

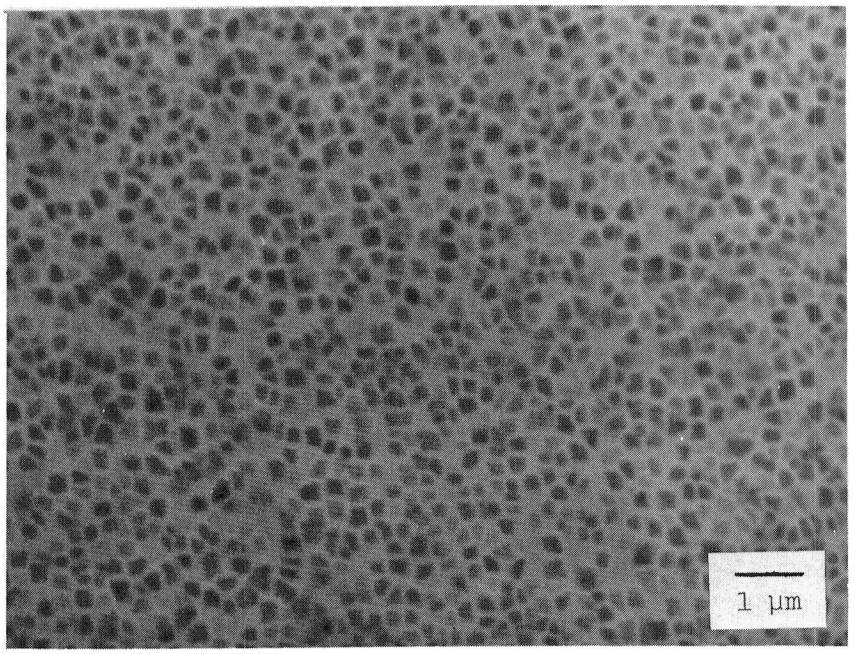

a

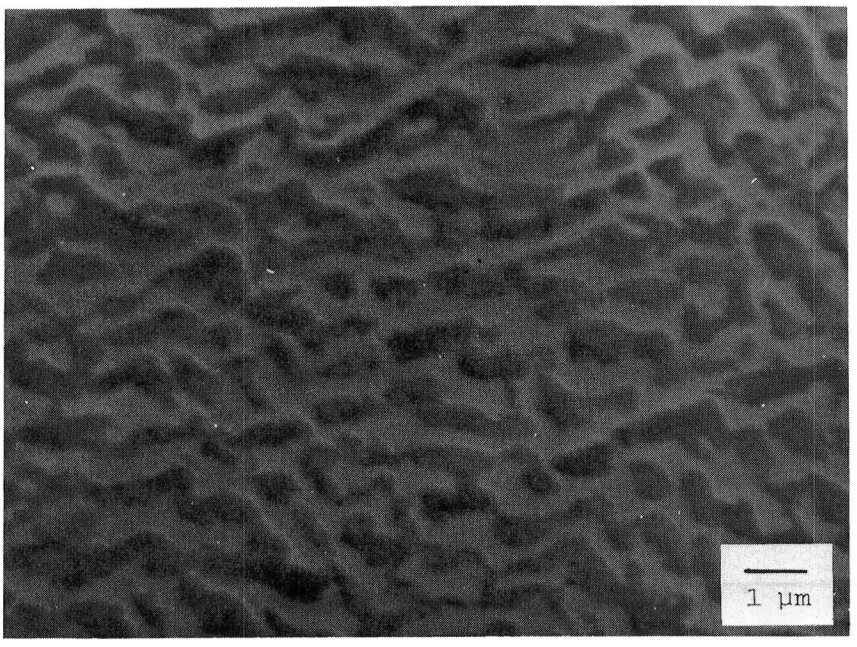

b

Figure 28: SEM micrographs showing the post-creep tested gamma prime morphology of the DS MAR-M247-type alloys at (a) 760°C and (b) 982°C. The stress axis is vertical in the micrographs.

Discussion

A. Microstructure and Phase Compositions

The addition of tantalum has been shown to affect the carbide composition, gamma and gamma prime compositions, and to increase the gamma prime and minor phase fractions of B-1900 + Hf and MAR-M247. Each of these effects will be addressed in turn within this section before comparing the effects of Ta on the two alloy series, B-1900 + Hf and MAR-M247 (DS and conventionally cast).

The obvious effect of Ta on the carbide composition (see Figures 5 and 13) is that Hf is replaced by Ta, with the Hf then being redistributed to the matrix phases. However, the degree of replacement is a function of heat treatment condition. The extent of substitution can be measured by plotting the ratio of Ta to Hf in the carbides against the ratio of Ta to Hf in the alloy. A slope of greater than unity for an alloy system indicates that Ta is a stronger carbide former than Hf. From the data in Figures 5 and 13, this "relative carbide forming strength" has been calculated and is plotted in Figure 29. Three separate curves are evident: as-cast MAR-M247-type alloys, as-cast B-1900 + Hf-type alloys, and both alloy systems after heat treatment, in order of decreasing slope. The significant decrease in slope (less Hf replacement by Ta in the carbides) for both alloy systems after heat treatment may be a result of the more thermodynamically stable Hf-rich MC carbides replacing the less stable Ta-rich MC carbides which form during solidification. The observed breakdown of MC carbides, changes in the carbide composition, and the elimination of Ti and Ta-rich MC carbides by heat treatment are consistent with this interpretation. An increase in the amount of Hf-rich MC carbides during heat treatment has also been observed in other studies

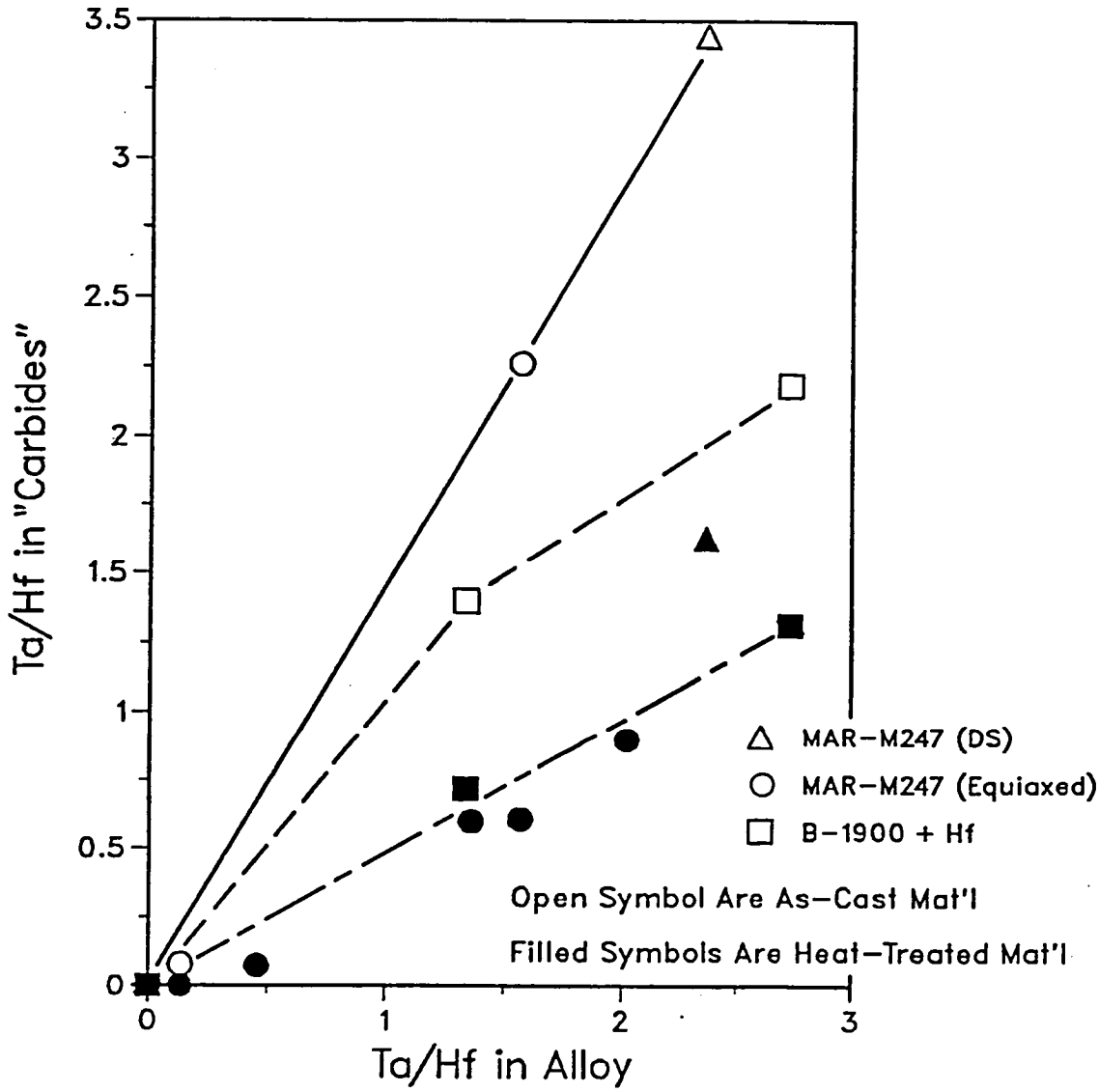

Figure 29: Ratio of Ta to Hf in the carbides plotted against the ratio of Ta to Hf in the as-cast and heat treated B-1900 + Hf and MAR-M247-type alloys.

of MAR-M247 and similar alloys [8, 14, 43, 45]. The differences in slope for as-cast MAR-M247 and as-cast B-1900 + Hf are possibly a result of differences in casting practice; i.e. more rapid cooling rates lead to more inhomogeneous carbides.

The gamma prime compositions of B-1900 + Hf and MAR-M247 were relatively insensitive to bulk Ta variations; the only significant changes were increases in the Ta level (both alloy series) and the Hf and Al levels (only B-1900 + Hf). This is in good agreement with the results on Ta variations in single crystal MAR-M247 (without Hf) [27, 41]. Although the increases in the Ta and Hf levels were not large, small additions of refractory metals such as Hf and Ta, which are thought to be potent solid solution strengtheners in addition to their possible effects on the APB energy, may have a significant impact on mechanical properties.

The gamma phase compositions were much more sensitive to variations in bulk Ta content than were the gamma prime phase compositions. In addition to the increase in the Ta concentration (an effective gamma strengthener), the addition of Ta brought about increases in the Co and Cr levels in both alloy series and the Al level in the MAR-M247-type alloys. The increases in the Co and Cr concentrations are believed to be due to two causes: 1) inadvertent increases in bulk Cr and Co levels with Ta additions (only MAR-M247) and 2) decreases in the gamma phase fraction coupled with constant partitioning ratios for Co and Cr with increasing bulk Ta. The latter cause is likely more significant in light of the increases in Cr and Co levels in the gamma phase of the B-1900 + Hf-type alloys where no bulk compositional variations exist. An increase in the Al concentration of the gamma phase with Ta additions was only observed

in the MAR-M247-type alloys. The nearly constant Al partitioning ratio for all alloys except the zero Ta DS alloy suggests that the increases in the Al level of the gamma phase are largely a result of the inadvertent increases in bulk Al content. While Al partitioning ratios of greater than 20 were also found for the two zero Ta alloys in one of the single crystal MAR-M247 studies [27], it is not apparent how low levels of Ta can influence the Al partitioning behavior. Further work is planned to examine this result by determining directly the Al levels of the gamma and gamma prime phases by STEM microanalytical techniques.

Although the redistribution of Hf from the carbides to the matrix phases has been mentioned previously, this aspect of the "Ta effect" merits further discussion. The preferred order for metallic elements to form MC carbides is Ta, Nb, Ti, and V [12]; as has been shown in this study, Hf lies either above or immediately below Ta, depending on heat treatment. The addition of a strong carbide forming element to an alloy will result in the partial, if not nearly complete, replacement of the weaker carbide forming elements in the carbides. The redistribution of these elements to the gamma and gamma prime phases will alter the compositions and/or volume fractions of gamma and gamma prime and, ultimately, may also affect the mechanical properties. In this study, the addition of Ta to B-1900 + Hf brought about an increase in the Hf concentration of the gamma prime phase while its level in the gamma phase was constant. A more striking illustration of this redistribution is the increase in the Hf partitioning ratio from 0.5 to 3.0 with the addition of 1.34 atomic percent Ta (see Figure 20c). Experimental difficulties prevented the Hf behavior in the MAR-M247-type alloys from being studied, but a similar effect is thought to occur. The redistribution of elements such as Ti,

Ta, and Nb from the carbides to the matrix phases may also be one of the mechanisms for the improved mechanical properties of superalloys with Hf additions.

The addition of Ta to B-1900 + Hf and MAR-M247 increases the weight fraction of the minor phases (primarily MC carbides) and possibly decreases the amount of $M_{23}C_6$ carbides present. Although the scatter in the minor phase data is relatively large (regression coefficient of 0.73), the trend of increasing weight fraction with Ta additions is clear from Figure 18. Three possible explanations for this behavior are variations in bulk carbon concentration, an increase in the mean atomic weight of the metallic elements that compose the MC carbides (while maintaining stoichiometry), and a reduction in the amount of carbon dissolved in the matrix phases. While there is scatter in the carbon contents of the two alloy series, it is random in nature and could not explain the observed increases. The atomic weights of Hf and Ta (178.5 and 181.9, respectively) are very close, which eliminates the possibility of atomic weight effects. The only plausible explanation, that Ta additions decrease the amount of carbon dissolved in the matrix phases thereby increasing the weight fraction of the carbides, is not unreasonable as this mechanism has also been suggested for Hf additions [15]. Furthermore, the addition of Ta may also decrease the amount of the chromium-rich $M_{23}C_6$ carbides that precipitate during heat treatment. This hypothesis is supported by the decrease in the Cr level of the carbide residue from both alloy series (see Figure 13) as the bulk Ta level increases and the absence of strings of $M_{23}C_6$ carbide particles in the Ta containing MAR-M247-type alloys. The reduction in $M_{23}C_6$ precipitation could either be caused by a decrease in carbon solubility of the matrix phases or increased MC

carbide stability, resulting in less carbon being available for secondary carbide formation.

The addition of tantalum to B-1900 + Hf and MAR-M247 increased the weight fraction of gamma prime, as would be expected from the large partitioning ratio of Ta. This result is consistent with observations in two previous studies of single crystal MAR-M247 [27, 41]. However, the increase is greater than would be expected from the most extreme circumstance in which Ta partitioned completely to gamma prime. For example, the addition of 4.3 weight percent Ta to B-1900 + Hf should lead only to a 4.3 weight percent increase in gamma prime fraction, but the actual increase was 8 percent. The additional increase in the gamma prime weight fraction is likely a result of the additional redistribution of the remaining alloying elements.

The gamma prime morphologies observed in the two alloy series are a puzzling aspect of this study. The gamma prime in the as-cast B-1900 + Hf and MAR-M247-type alloys is cuboidal, with the cube edges about 1 micron in length. After the solution and age heat treatment, the gamma prime morphology is cuboidal in B-1900 + Hf and spheroidal to flat-faced spheroidal in MAR-M247 with increasing Ta level. However, in both alloys, the maximum dimension of the gamma prime particles is 0.10 to 0.15 microns. The gamma prime in MAR-M247 reverts to the original cuboidal morphology upon coarsening after long term aging without stress [47] or during creep rupture testing at 760 and 871°C. The differences in the gamma prime morphologies of the B-1900 + Hf and MAR-M247 alloy series after heat treatment could be attributed to greater gamma/gamma prime mismatch in the B-1900 + Hf-type alloys, although no interfacial dislocations or delta-fringes, normal indications of coherency strains, were

observed using TEM under any heat treatment conditions. The transition from cuboids to spheroids and back again to cuboids is more difficult to rationalize for the MAR-M247-type alloys. In order to fully examine this phenomena, the gamma/gamma prime misfit measurements should be performed at the aging temperature. Nevertheless, the lack of interfacial dislocations indicates that the misfit must be small; therefore, the observations in this and other studies may not support the traditional viewpoint that gamma prime morphology is strictly a function of gamma/gamma prime misfit. For example, it has been observed for Ni-Co-Al alloys that the gamma prime morphology changed from spheroidal to cuboidal as the particle size increased during the initial stages of coarsening without any increase in lattice misfit. It has been suggested that this is a result of the {100} planes having a low energy which causes a reduction in total surface energy [48]. High temperature in-situ x-ray diffraction and aging studies are necessary to fully understand this aspect of microstructural development.

The effects of Ta on the microstructure of B-1900 + Hf and MAR-M247 are very similar, although several differences between the two alloy series are also present. First, to examine the similarities, both alloy systems exhibit increasing gamma prime and minor phase weight fractions as well as Hf replacement in the MC carbides with Ta additions. It will be demonstrated later in this discussion that two of these changes, increases in the gamma prime weight fraction and solid solution hardening by Hf and Ta, are the most significant Ta effects on the mechanical properties of DS MAR-M247; they would be expected to have similar importance in B-1900 + Hf. The increase in gamma prime lattice parameter and apparent decrease in the amount of $M_{23}C_6$ carbide precipitation with

increasing Ta content are also common to both alloy series. The dissimilarities between the two alloy systems can either be related or unrelated to Ta variations. The absence of significant amounts of script MC carbides and the lack of a Ta dependency on eutectic pool morphology in MAR-M247, both observed in B-1900 + Hf, are likely related to differences in casting practices. The only notable differences in the phase composition behavior of the two alloy series were the presence of Ti in the gamma phase of B-1900 + Hf (independent of Ta level) and the Al partitioning behavior in MAR-M247. The sole difference in the microstructure of conventionally cast and DS MAR-M247 is the tendency for W to partition more to the carbides and the gamma prime phase in the DS material compared to the conventionally cast alloys, regardless of Ta level. Overall, the similarities are more important than the dissimilarities since they have a profound influence on alloy performance, and, therefore, it is concluded that the effects of Ta on the microstructure of B-1900 + Hf and MAR-M247 (DS and conventionally cast) are not specific to either alloy.

B. Mechanical Properties

In the present study, tantalum additions have been shown to improve the creep rupture resistance, yield stress, and ultimate tensile strength of directionally solidified MAR-M247. However, the extremely low ductilities of the fully heat treated conventionally cast alloys (with and without Ta) limited the quantity of mechanical property data obtained and therefore prevents any detailed analysis from being performed on the effects of Ta on the mechanical properties of the conventionally cast alloys.

The primary mechanisms responsible for the improvements in the strength of the DS alloys as Ta is added are thought to be solid solution hardening of the gamma and gamma prime phases and increases in the gamma prime volume fraction. The solid solution strengthening mechanisms are, however, more extensive than normally considered in classical solid solution hardening theory. With regard to nickel-base superalloys, the possible solid solution effects as solute is added can include increasing the APB energy of the gamma prime phase, decreasing the stacking fault energy of the gamma phase, and decreasing the diffusion rate, in addition to changes in the elastic moduli and lattice parameter. Additions of refractory metals are particularly effective in reducing the diffusion rate because they diffuse slowly and also concomitantly reduce the diffusion coefficients of the other alloying elements.

The benefits of increasing the volume fraction of fine gamma prime on strength (both creep and tensile) has been well documented experimentally [10, 49, 50, 51] and theoretically [35, 52]. Intuitively, this is reasonable from the standpoint of increased frequency of precipitate/dislocation interactions. In the most applicable previous study, on a sister alloy of MAR-M247, MAR-M200, a three-fold increase in creep rupture life was realized with an increase in the volume fraction of fine gamma prime from 30 to 45 percent [10]*. The addition of 1 atomic percent Ta to DS MAR-M247 resulted in about a five-fold increase in creep rupture life at all tempertures and stresses tested, but only a corresponding increase in gamma prime weight fraction (all of which is fine gamma

---

* The densities of gamma and gamma prime for both MAR-M200 and MAR-M247 were determined to differ by less than 3% using the published phase compositions [6, 27, 41]. Therefore, weight fraction and volume fraction are essentially equal and interchangable for each alloy.

prime) from 56.5 to 62.0 percent. The increase in creep resistance is greater for MAR-M247 than would be anticipated from strictly a gamma prime volume fraction effect (based on the MAR-M200 data) and indicates the presence of another strengthening mechanism, which is suggested to be solid solution strengthening of gamma and gamma prime.

While a detailed analysis of the strengthening effects due to solid solution hardening (and its combination with precipitation hardening) is beyond the scope of the present work, it can be demonstrated that solid solution effects are an important strengthening mechanism by comparing the creep rupture resistance of the DS MAR-M247-type alloys (with Hf, Zr, and B) from this study to the single crystal (SC) MAR-M247-type alloys (without Hf, Zr, and B) from a previous study [27]. Using the Larson-Miller plots, the stress necessary to obtain a secondary creep rate of 10^{-6} sec^{-1} at 760°C was calculated for the two DS alloys and two SC alloys, one with zero Ta and the other with the normal 1 atomic percent Ta. The results, plotted in Figure 30, show that the Hf-Zr-B containing DS alloys require a higher stress to achieve the same secondary creep rate than the single crystal alloy with the same Ta level. This is somewhat surprising in light of the well documented advantages of single crystal components, including improved creep resistance, for commercial alloys such as MAR-M200 [53]. The mechanism that is thought to be responsible for the additional increment of creep strength is solid solution hardening of the gamma and/or gamma prime phases by Hf. Zr and B are also added to the DS alloys, but their primary location is along grain boundaries, where they have been shown to improve alloy ductility and increase the gamma prime phase stability, particularly along transverse grain boundaries [12, 26]. Although their presence would affect rupture lifetime since they enhance

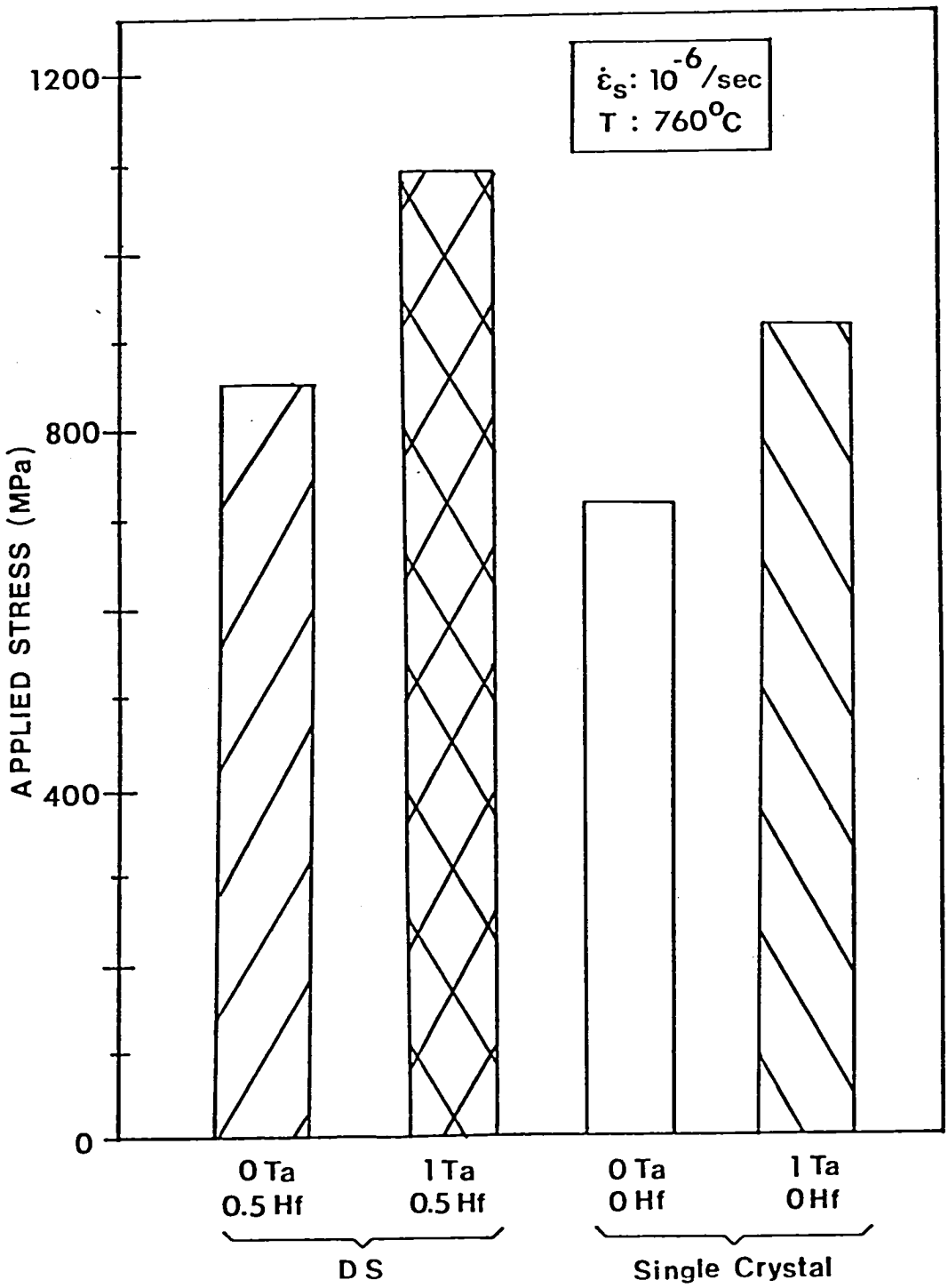

Figure 30: Comparison of the stresses necessary to obtain a secondary creep rate of 10^{-6}/sec at 760°C for the DS MAR-M247-type alloys (with Hf) and single crystal MAR-M247-type alloys (without Hf) with the same Ta variations.

ductility and delay the onset of tertiary creep, they should have a minimal affect on the secondary creep rate. The gamma prime weight fractions are equivalent at a given Ta level for the DS and SC alloy series so that the comparison is independent of any precipitation hardening effect. These arguments allow one to conclude that the solid solution effects of Hf do indeed strengthen the DS MAR-M247-type alloys. Although it can not be presently demonstrated for the case of Ta, a similar effect on superalloy strength with Ta additions would also be expected since Ta and Hf are chemically very similar. In addition, Ta additions have been shown to increase the strength of the gamma prime phase [54].

The extremely low ductilities and premature failures exhibited by the conventionally cast alloys (with and without Ta) precluded any useful mechanical property data from being collected, but the results do provide some useful insight into the fracture behavior of polycrystalline superalloys. Elongations to failure for conventionally cast MAR-M247 with only an aging treatment (without a solution treatment) are about 5 percent for creep rupture tests at 760°C to 982°C and 4 to 8 percent for tensile tests at 650°C to 982°C [55]. These values certainly were not attained in this study, as is evident for alloys A1 and B1 in Tables 6 and 7. The low ductilities are caused by the early failure of the transverse grain boundaries, which is likely a result of the solutionizing of the gamma/gamma prime eutectic along the grain boundaries. It has been suggested that primary gamma prime increases alloy ductility because it is inherently ductile [11] and therefore aides strain accommodation at the grain boundaries. The solutionizing of the as-cast gamma prime and subsequent reprecipitation strengthens the matrix, but also apparently weakens the grain boundaries. An alternate way to state this is that the stress

necessary to fracture the boundary is less than the strength of the bulk material. This hypothesis can be proven by determining the effects of primary gamma prime on alloy ductility by solutionizing for different times to control the fraction of primary gamma prime along the grain boundaries.

Although it was previously stated that carbides play no direct role in the strengthening of superalloys, the precipitation of a homogeneous distribution of secondary carbides by heat treatment could give an additional increment of strengthening. Extended solution treatments enhance the breakdown of MC carbides, but also increase the volume fraction of porosity. The carbon released from the MC carbide degeneration would be expected to form secondary carbides, likely of the $M_{23}C_6$-type observed in these two alloy systems. The precipitation of these carbides throughout the structure during heat treatment, and on dislocations and stacking faults during creep testing [12], would increase the resistance of the material to deformation. Since the $M_{23}C_6$ carbides are thermodynamically stable and possibly coherent [13], they would not be expected to coarsen rapidly nor dissolve. Thus, because of these two features, precipitation of $M_{23}C_6$ carbides is an attractive alternative high temperature strengthening mechanism. An additional benefit of replacing the MC carbides with $M_{23}C_6$ carbides is the redistribution of the metallic elements, mainly Ta and Hf, from the MC carbides to the gamma and gamma prime phases. Long term solution treatments to dissolve the MC carbides, followed by hot isostatic pressing to eliminate the subsequent porosity, are planned to confirm the feasibility of this potential strengthening mechanism.

CONCLUSIONS

1. The gamma prime solvus temperature of the polycrystalline MAR-M247 and B-1900 + Hf-type alloys was increased by Ta additions. The as-cast gamma/gamma prime eutectic and coarse gamma prime were completely dissolved during the four hour solutionizing treatment without the occurrence of incipient melting.

2. The addition of tantalum to both the as-cast and heat treated MAR-M247 and B-1900 + Hf-type alloys resulted in the partial replacement of Hf by Ta in the MC carbides, although the degree of this substitution was decreased by heat treatment. In the case of B-1900 + Hf, the Hf from the MC carbides was redistributed almost exclusively to the gamma prime phase.

3. Very small (less than 1 micron) chromium-rich $M_{23}C_6$ carbides precipitated during heat treatment and are distributed inhomogeneously throughout all of the alloys. Three morphologies, acicular, blocky, and, occasionally, hexagonal, were observed with TEM in the B-1900 + Hf and MAR-M247-type alloys. In addition, strings of discrete $M_{23}C_6$ carbide particles formed in the zero Ta MAR-M247-type alloys. The apparent cube-on-cube orientation relationship and lattice parameter relationship ($a_{carbide}=3a_{matrix}$) was maintained regardless of the morphology or distribution of the $M_{23}C_6$ carbides. The decrease in the Cr level of the composite carbide residue with increasing bulk Ta level indicated that Ta additions decrease the amount of $M_{23}C_6$ present in the microstructure.

4. The gamma prime and minor phase (mainly MC carbides) fractions of the heat treated MAR-M247 and B-1900 + Hf-type alloys both increased linearly with Ta concentration. For example, the addition of 0.97 atomic percent Ta to the DS MAR-M247-type alloys resulted in an increase in the gamma prime fraction from 56.5 to 62.0 weight percent and an increase in the minor phase fraction from 1.25 to 1.75 weight percent, respectively.

5. The gamma prime phase compositions of the heat treated B-1900 + Hf and MAR-M247-type alloys were relatively insensitive to bulk Ta variations. Only the Ta levels in both alloy series and the Hf and Al levels in the B-1900 + Hf alloy series showed significant increases with Ta additions.

6. The Cr and Co levels in the gamma phase of the B-1900 + Hf and MAR-M247-type alloys increased significantly with Ta additions; the increases are a reflection of the decrease in the gamma phase fraction and constant Cr and Co partitioning ratios. The increase in the Al concentration of the gamma phase in MAR-M247-type alloys with Ta additions, which was not observed in the B-1900 + Hf-type alloys, appears to be a result of an inadvertent increase in bulk Al concentration. The Ta level also increased, particularly at higher bulk Ta levels, in the gamma phase.

7. The yield stress and ultimate tensile strength of the DS MAR-M247-type alloys at 540, 760, and 982°C are increased by the addition of Ta, without a significant decrease in ductility. The mechanisms responsible for these improvements are increased gamma prime weight

fraction and increased solid solution effects in the gamma and gamma prime phases. The sources of the solute elements are the direct addition of Ta to the alloy, the indirect effect of Ta replacement of Hf in the MC carbides with subsequent redistribution of Hf to gamma and gamma prime, and slight redistributions of other alloying elements. In contrast to classical solid solution hardening, increases in the APB energy of the gamma prime phase, decreases in the stacking fault energy of the gamma phase, and reduced diffusion rates are incorporated into the solid solution effects.

8. The addition of Ta to the DS MAR-M247-type alloys increased the creep resistance by increasing the time to rupture and decreasing the secondary creep rate at 760, 871, and 982°C. The mechanisms responsible for these enhanced properties are the same as those for improved tensile strength, namely increased solid solution strengthening and gamma prime weight fraction with Ta additions. Stress coarsening of the gamma prime precipitates may also play a role in the creep resistance at 982°C, although this potential strengthening mechanism did not appear to be a function of Ta level in the DS MAR-M247-type alloys.

9. The premature failures of the conventionally cast MAR-M247-type alloys during tensile and creep testing precluded the attainment of much mechanical property data. The two successful tensile tests and one successful creep test indicate that the properties of the DS and conventionally cast alloys are comparable, although the ductility of the DS alloys was greater. It was suggested that the solutionizing of the reportedly ductile gamma/gamma prime eutectic caused a reduction in the

strain accommodation along the grain boundaries and, therefore, the low ductilities observed in the heat treated conventionally cast MAR-M247-type alloys.

10. By comparing the creep resistance of the DS MAR-M247-type alloys (with Hf) and the creep rupture resistance of the single crystal MAR-M247-type (without Hf) alloys from a previous study, it was demonstrated that Hf is a potent solid solution strengthener of MAR-M247.

REFERENCES

1). J.R. Stephens: NASA TM-82852, NASA-Lewis Research Center, Cleveland, OH, May 1982.

2). O.H. Kriege and J.M. Baris: Trans. ASM, 1969, vol. 62, pp. 195-200.

3). R.F. Decker: Strengthening Mechanisms in Nickel-Base Superalloys, Steel Strengthening Symposium, Zurich, Switzerland, 1969.

4). W.C.Hagel and H.T. Beattie: Iron and Steel Inst., Spec. Rep. 64, pp. 98-107.

5). R.A. Gregg and B.J. Piearcey: Trans. TMS-AIME, 1964, vol. 230, pp. 599-600.

6). B.J. Piearcey, B.H. Kear, and R.W. Smashey: Trans. ASM, 1967, vol. 60, pp. 634-45.

7). B.H. Kear and D.E. Fornwalt: in Superalloys - Metallurgy and Manufacture, Proc. 3rd Int. Sym., Ed. by B.H. Kear, D.R. Muzyka, J.K. Tien, and S.T. Wlodek, High Temperature Alloys Committee, AIME, New York, NY, 1976, pp. 255-64.

8). C. Lund and J.F. Radavich: in Superalloys 1980, Proc. 4th Int. Sym. on Superalloys, Ed. by J.K. Tien, S.T. Wlodek, H. Morrow, M. Gell, and G.E. Maurer, ASM, Metals Park, OH, 1980, pp. 85-98.

9). B.J. Piearcey and B.E. Terkelsen: Trans. TMS-AIME, 1967, vol 238, pp. 1143-50.

10). J.J. Jackson, M.J. Donachie, R.J. Hendricks, and M. Gell: Metall. Trans. A, 1977, vol. 8A, pp. 1615-20.

11). D.H. Maxwell, J.F. Baldwin, and J.F. Radavich: Metall. Met. Form., 1975, vol. 42, No. 10, pp. 332-399.

12). R.F. Decker and C.T. Sims: in The Superalloys, John Wiley and Sons, Inc., New York, NY, 1972, pp. 33-78.

13). B.J. Piearcey and R.W. Smashey: Trans. TMS-AIME, 1967, vol. 239, pp. 451-57.

14). A. Saam and J.F. Radavich: in Microstructural Science, Volume 10, Ed. by White, Richardson, and McCall, Elsevier Science Publishing Co., Inc., New York, NY, 1982, pp. 393-99.

15). J.M. Dahl, W.F. Danesi, and R.G. Dunn: Metall. Trans., 1973, vol. 4, pp. 1087-96.

16). S.W. Wawro: NASA CR-167892, NASA-Lewis Research Center, Cleveland, OH, June 1982.

17). P.S. Kotval, J.D. Venables, and R.W. Calder: Metall. Trans. A, 1972, vol. 3A, pp. 1615-20.

18). D.N. Duhl and C.P. Sullivan: J. Metals, 1971, vol. 23, No. 7, pp. 38-40.

19). F.R. Beckitt and B.R. Clark: Acta Met., 1967, vol. 15, pp. 113-29.

20). H.E. Collins: Trans. TMS-AIME, 1969, vol. 62, pp. 82-104.

21). B.J. Piearcey and R.W. Smashey: Trans. TMS-AIME, 1967, vol. 239, pp. 451-57.

22). C.T. Sims: in The Superalloys, John Wiley and Sons, Inc., New York, NY, 1972, pp. 259-84.

23). J.R. Mihalisin, C.G. Bieber, and R.T. Grant: Trans. TMS-AIME, 1968, vol. 242, pp. 2399-2414.

24). E.S. Machlin and J. Shao: Metall. Trans. A, 1978, vol. 9A, pp. 561-68.

25). R.G. Menzies, R.H. Bricknell, and A.J. Craven: Phil. Mag. A, 1980, vol. 41, No. 4, pp. 493-508.

26). R.F. Decker and J.W. Freeman: Trans. TMS-AIME, 1960, vol. 218, pp. 277-85.

27). H.C. Nguyen: The Effect of Tantalum and Carbon on the Structure/ Properties of a Single Crystal Nickel-Base Superalloy, M.S. Thesis, Michigan Technological University, 1984.

28). R.V. Miner: Metall. Trans. A, 1977, vol. 8A, pp. 259-63.

29). G.R. Leverant and M. Gell: Trans. TMS-AIME, 1969, vol. 245, pp. 1167-73.

30). R. Nordheim and N.J. Grant: J. Inst. Met., 1954, vol. 82, pp. 440-44.

31). N.S. Stoloff: in The Superalloys, John Wiley and Sons, Inc., New York, NY, 1972, pp. 79-111.

32). R.M.N. Pelloux and N.J. Grant: Trans. of TMS-AIME, 1960, vol. 218, pp. 232-37.

33). T.H. Hazlett and E.R. Parker: Trans. of ASM, 1954, vol. 46, pp. 701-15.

34). R.W. Guard and J.W. Westbrook: Trans. of TMS-AIME, 1959, vol. 215, pp. 807-14.

35). S.M. Copley and B.H. Kear: Trans. of TMS-AIME, 1967, vol. 239, pp. 984-92.

36). M.L. Sessions, C.J. McMahon, Jr., and J.L. Walker: Mater. Sci. Eng., 1977, vol. 27, pp. 17-24.

37). K.R. Williams and B. Wilshire: Met. Sci. J., 1973, vol. 7, pp. 176-78.

38). P.W. Davies, G. Nelmes, K.R. Williams, and B. Wilshire: Met. Sci. J., 1973, vol. 7, pp. 87-92.

39). J.D. Parker and B. Wilshire: Met. Sci. J., 1975, vol. 9, pp. 248-52.

40). S. Purushothaman and J.K. Tien: Acta Met., 1978, vol. 26, pp. 519-28.

41). M.V. Nathal: NASA TM-83479, NASA-Lewis Research Center, Cleveland, OH, January 1984.

42). M.J. Donachie and O.H. Kriege: J. Mater., 1972, vol. 7, pp. 269-78.

43). M.V. Nathal, R.D. Maier, and L.J. Ebert: Metall. Trans. A, 1982, vol. 13A, pp. 1775-82.

44). W.B. Pearson: Handbook of Lattice Spacings and Structures of Metals and Alloys, Volume 2, Pergamon Press Ltd., London, 1967.

45). G.L. Erickson, K. Harris, and R.E. Schwer: presented at "High Temperature Alloys: Theory and Design", co-sponsored by TMS-AIME and ORNL, Bethesda, MD, April 9-11, 1984 (proceedings to be published).

46). H.C. Nguyen, B.J. Pletka, and R.W. Heckel: presented at "High Temperature Alloys: Theory and Design", co-sponsored by TMS-AIME and ORNL, Bethesda, MD, April 9-11, 1984 (proceedings to be published).

47). K.L. Fink: Stability of Carbides and The Gamma Prime Phase in Nickel-Base Superalloys, Senior Project Report, Michigan Technological University, 1984.

48). C.K.L. Davies, P. Nash, and R.N. Stevens: J. Mat. Sci., 1980, vol. 15, pp. 1521-32.

49). P. Beardmore, R.G. Davies, and T.L. Johnson: Trans. TMS-AIME, 1967, vol. 245, pp. 1537-45.

50). L.R. Cornwell, J.D. Embury, and G.R. Purdy: in Proc. 3rd Bolton Landing Conf. on Ordered Alloys, Ed. by N.S Stoloff and J.H. Westbrook, Claitors Publishing Compoany, Baton Rouge, 1972, pp. 387-404.

51). B. Reppich, P. Schepp, and G. Wehner: Acta Met., 1982, vol. 30, pp. 95-104.

52). B. Reppich: Acta Met., 1982, vol. 30, pp. 87-94.

53). B.H. Kear and B.J. Piearcey: Trans. of TMS-AIME, 1967, vol. 239, pp. 1209-15.

54). S. Chakravorty and D.R.F. West: Metals Technology, 1980, vol. 7. pp. 414-18.

55). M.V. Nathal, R.D. Maier, and L.J. Ebert: Metall. Trans. A, 1982, vol. 13A, pp. 1767-74.

1. Report No.	2. Government Accession No.	3. Recipient's Catalog No.
NASA CR-174847		

4. Title and Subtitle	5. Report Date
The Effect of Tantalum on the Structure/Properties of Two Polycrystalline Nickel-Base Superalloys: B-1900 + Hf and MAR-M247	February 1985
	6. Performing Organization Code
7. Author(s)	8. Performing Organization Report No.
Gregg M. Janowski	None
	10. Work Unit No.
9. Performing Organization Name and Address	11. Contract or Grant No.
Michigan Technological University Houghton, Michigan	NAG 3-216
	13. Type of Report and Period Covered
12. Sponsoring Agency Name and Address	Contractor Report
National Aeronautics and Space Administration Washington, D.C. 20546	14. Sponsoring Agency Code
	505-33-62

15. Supplementary Notes

Final report. Project Manager, Robert L. Dreshfield, Materials Division, NASA Lewis Research Center, Cleveland, Ohio 44135. This report was a thesis submitted in partial fulfillment of the requirements for the degree of Master of Science in Metallurgical Engineering to Michigan Technological University, Houghton, Michigan in 1984.

16. Abstract

The microstructure, phase compositions, and phase fractions were studied in conventionally cast B-1900 + Hf and both conventionally cast and directionally solidified MAR-M247 as a function of tantalum concentration. The hot tensile and creep rupture properties of the solutionized and aged MAR-M247-type alloys were also determined as a function of tantalum level. The effects of tantalum on the microstructure and phase compositions of B-1900 + Hf and MAR-M247 (conventionally cast and directionally solidified) were found to be very similar. The addition of tantalum to the as-cast and heat treated alloys was shown to cause the partial replacement of the Hf in the MC carbides by Ta, although the degree of replacement was decreased by the solutionizing and aging heat treatment. The gamma prime and minor phase fractions (primarily MC-type carbides) both increased approximately linearly with tantalum concentration. The gamma prime phase compositions were relatively insensitive to tantalum variations with the exception of the tantalum and/or hafnium levels. Bulk tantalum additions increased the tantalum, chromium, and cobalt levels of the gamma phase in both alloy series. The increase in the concentrations of the latter two elements in the gamma phase was a result of the decrease in the gamma phase fraction with increasing bulk tantalum concentration and constant gamma/gamma prime partitioning ratio. Tantalum additions increased the yield strss and ultimate tensile strength of the directionally solidified MAR-M247-type alloys and had no significant effect on ductility. The secondary creep rate was decreased and the creep rupture life was increased in the directionally solidified MAR-M247-type alloys with the addition of tantalum. The mechanisms believed responsible for these improvements are the increase in gamma prime weight fraction and increased solid solution strengthening of the gamma and gamma prime phases with increasing tantalum content. Stress coarsening of the gamma prime precipitates was also observed in the creep samples tested at 982°C. The conventionally cast MAR-M247-type alloys exhibited extremely low ductilities and premature failures which were related to the large fraction of intergranular fracture surface observed in the failed specimens.

17. Key Words (Suggested by Author(s))	18. Distribution Statement
Ni alloy; Tantalum; Superalloy; Microstructure; Mechanical properties	Unclassified - unlimited STAR Category 26

19. Security Classif. (of this report)	20. Security Classif. (of this page)	21. No. of pages	22. Price*
Unclassified	Unclassified	108	A06

*For sale by the National Technical Information Service, Springfield, Virginia 22161

NASA Langley Rsch Center
Attn Library
Langley Field, VA 23365